The Dissertation Committee for Subramanian Sankaranarayanan Certifies that this is the approved version of the following Dissertation:

EVALUATION OF MECHANISMS GOVERNING THE STABILIZATION OF UNBOUND AGGREGATE BASES BY GEOGRIDS IN FLEXIBLE PAVEMENTS

Committee:

Jorge G. Zornberg, Supervisor

Robert B. Gilbert

Amit Bhasin

Andre Smit

EVALUATION OF MECHANISMS GOVERNING THE STABILIZATION OF UNBOUND AGGREGATE BASES BY GEOGRIDS IN FLEXIBLE PAVEMENTS

by

Subramanian Sankaranarayanan

Dissertation

Presented to the Faculty of the Graduate School of

The University of Texas at Austin

in Partial Fulfillment

of the Requirements

for the Degree of

Doctor of Philosophy

The University of Texas at Austin

May 2023

Dedication

To my mom, for always supporting my aspirations.

To my grandmother, for being the source of my inspiration.

To my family, for their undying support.

To my loving wife, for always being there through all of my endeavors.

Acknowledgements

I would like to express my sincere gratitude to my advisor, Professor Jorge G Zornberg, for believing in me and giving me the opportunity to be a part of his research team. Under his guidance, I was able to be a part of several experimental and field projects related to pavement design, analysis, instrumentation, and monitoring that were not a part of this dissertation, but allowed me to gain technical expertise and knowledge that were highly useful in completing the work outlined in this dissertation. It is under his tutelage that I evolved into being an independent researcher, a mentor for others, a collaborator, and a professional engineer, for which I owe him my eternal gratitude.

My heartfelt thanks to the members of the dissertation committee whose valuable insights and constructive feedback greatly benefited the work in this dissertation. Having come from a geotechnical background and starting my research in pavements, I was fortunate to have collaborated early-on with Dr. Smit, whose technical knowledge in the field of pavement engineering and expertise in accelerated pavement testing were invaluable to the successful start of my research career. The three graduate courses and innumerous interactions I had with Dr. Bhasin, be it in the class or in his office or over the email, greatly benefitted not only my technical understanding of flexible pavements, and visco-elastic materials, but also of the scientific method, and the potential for cross-pollination of ideas across disciplines. My interactions with Dr. Gilbert on the subject of foundation engineering were highly insightful, and useful as they helped challenge my approach and evaluation of the outcomes from my research.

Much of my engineering knowledge in geomaterial behavior and pavement analysis I owe to the brilliant ensemble of faculty members in the Department of Civil, Architectural and Environmental Engineering (CAEE) at the University of Texas at Austin. The graduate courses I took with Dr. Zornberg, Dr. Bhasin, Dr. Gilbert, and Dr. El Mohtar informed my understanding of geotechnical and pavement engineering significantly.

Without the fruitful debates, the exchange of ideas, the sharing of knowledge and expertise, and the brainstorming sessions I have had with my colleagues in the geotechnical and pavement engineering groups at UT Austin, my research would have been far less enjoyable. My sincere appreciation to Hossein Roodi, Amr Morsy, Behdad Mofarraj, Dawie Marx, and Wilfrido Martinez-Alonso for their valuable insights and feedback.

This research was primarily funded by the Texas Department of Transportation (TxDOT) through the Center for Transportation Research (CTR) at UT Austin. Additional support was received from the Geosynthetic Institute (GSI) in the form of GSI fellowships.

Subramanian Sankaranarayanan

29 March 2023

Abstract

EVALUATION OF MECHANISMS GOVERNING THE STABILIZATION OF UNBOUND AGGREGATE BASES BY GEOGRIDS IN FLEXIBLE PAVEMENTS

Subramanian Sankaranarayanan, Ph.D.

The University of Texas at Austin, 2023

Supervisor: Jorge G. Zornberg

The benefits of using geosynthetics to stabilize the unbound aggregate layers in flexible pavements, in terms of improvement to pavement life or potential decrease in layer thickness, have been well documented. Early research focused on developing ratios such as the traffic benefit ratio (TBR) or the layer coefficient ratio (LCR) to quantify (empirically) the benefits of including geogrids, and for their use in the design of flexible pavements with those geogrids. However, the lack of a mechanistic understanding of geogrid-stabilization and the empirical nature of this data limited their use to the geogrids and pavement materials that were used to develop them. With the proliferation of different geogrid products and pavement materials, the scope of the early research has become limited and attempts to correlate the properties of the geogrids and pavement materials to the improvement in performance of the pavement have not been successful. This study aims to further the understanding of the mechanisms involved in geogrid-

stabilization and to identify the mechanistically relevant properties that contribute to this stabilization.

Accelerated pavement tests are conducted, using the model mobile load simulator (MLS11), on reduced-scale pavement test sections with and without geogrids for stabilization under controlled, laboratory conditions. The performance of the pavement sections is evaluated by monitoring the deformation of the surface, the internal particle displacements (within the base), and the dynamic increase in stress (within the pavement structure) for increasing traffic volume. The deformation of the surface is obtained by profiling the surface of the pavement at regular traffic intervals using a laser profilometer, designed and built in-house for this study. A unique cost-effective displacement measuring technique is developed and implemented to obtain the horizontal displacement data of particles in the base. The data from the dense array of the particle tracking sensors is used to generate the horizontal displacement field, horizontal normal strain field and shear transfer efficiency plots in the base. The vertical stress distribution is obtained from the earth pressure cells installed within the pavement structure that are monitored for dynamic stress responses with applied traffic. The inclusion of the stabilizing geogrid resulted in reduced rut development, reduced particle displacements within the base and a wider distribution of the applied load for similar traffic volumes in the control and stabilized sections. The improvement in pavement life due to the stabilization of the base by the geogrid is quantified as the traffic benefit ratio (TBR). The TBRs are determined for seven different geogrids from the accelerated pavement tests, and correlated with the most commonly used in-isolation properties of the geogrid (geometric and tensile properties), and interaction properties of the geogrid-base aggregate composite. The TBRs are found to be best correlated to the coefficients of soil-geosynthetic composite stiffness (K_{SGC}) obtained from the soil-geosynthetic interaction tests.

Table of Contents

List of Tables

List of Figures

Chapter 1: Introduction

1.1 BACKGROUND

Mechanical stabilization of unbound aggregate base (UAB) layers in flexible pavements using tension-resistant materials (steel mesh, polymeric grids, and fabrics) has been studied for nearly five decades. Stabilization of the base is the application of the stiffening function that a geogrid provides when mechanically coupled (through friction and interlocking) with the unbound aggregates whereby the tensile stiffness of the geogrid stiffens the aggregate matrix against lateral spreading when subject to vertical stresses. Early full-scale laboratory and field studies (Bender and Barenberg, 1978; Brown et al., 1982; Halliday and Potter, 1984; Kinney and Barenberg, 1982; Ruddock et al., 1982; Webster and Watkins, 1977) indicated that the use of geosynthetics to stabilize the unbound layers could result in improved performance of flexible pavements in terms of rutting and fatigue cracking.

Several studies have since been conducted to quantify the benefits of geosynthetic-inclusion for stabilization of the unbound layers in flexible pavements (Al-Qadi et al., 1997; Chan et al., 1989; Haas et al., 1988; Smith et al., 1995) and to develop methods to design pavement sections with geosynthetic-stabilized aggregate layers (Giroud and Han, 2004a, 2004b; Holtz et al., 1998; Tingle and Webster, 2003). Early research focused on quantifying the improvement to pavement performance due to stabilizing geosynthetics as traffic benefit ratio (TBR), base course reduction (BCR) ratio or layer coefficient ratio (LCR)(Tingle and Jersey, 2009). These ratios were determined for a particular combination of geosynthetic, base material and pavement configuration.

The ratios were then used to develop empirical design procedures such as AASHTO R50 (2009).

However, the empirical nature of these methods limits their use to the geosynthetics, pavement materials and pavement configurations that were used to generate the data. With the rapid evolution of geosynthetic products and proliferation of their use with different pavement materials, the scope of the early research and empirical design methods have become limited. For instance, AASHTO R50 (2009) recommends determining the potential benefits of geosynthetic reinforcements (TBR or BCR) from design procedures mentioned in Berg et al. (2000), and Holtz et al. (1998). While the potential benefits from these empirical design methods are relevant to the particular dataset used to develop them, AASHTO R50 (2009) makes it clear that the accuracy of these methods are unverified for any specific pavement configuration. It is recommended to perform construction and performance monitoring of the constructed pavement to ensure the assumed benefits are, in fact, observed. Thus, whenever a new geosynthetic product is to be used, the design procedures require running full-scale laboratory tests with the specific geosynthetic product to determine their potential benefits (TBR or BCR) before being able to design with them. It is left to the manufacturer or the agencies (DOTs) to conduct those performance tests, a strategy that could be cost-prohibitive.

In order to design pavement sections with new geosynthetics and pavement materials, but using these empirical design methods, several DOTs have developed correlations between the potential benefits (TBR or BCR) and some characteristic properties of the geosynthetic used for stabilization. The potential benefit from a new geosynthetic is then predicted using the characteristic properties and correlations to the potential benefit. Characteristic properties that have been used commonly are the unconfined properties of the geosynthetic in isolation (tensile strength, junction strength,

stiffness, geometry) or the large-displacement interaction properties (interface strength ,pull-out resistance) between the geosynthetic and the aggregates (Berg et al., 2000). However, the geogrids within the pavement structure are neither unconfined nor undergo large displacements (owing to required serviceability criteria) (Roodi and Zornberg, 2017). Thus, any design method that involves the use of those properties cannot provide a holistic picture of the performance of the pavement. With the advent of Mechanistic Pavement Design methods, it is no longer possible use the empirical database of potential benefits to design geosynthetic-stabilized pavements. In order to develop a mechanistic design method for geosynthetic-stabilized pavements, there is a need for understanding the mechanisms involved in geogrid-stabilization (a confined, small-displacement phenomenon) and identifying the properties relevant to the associated mechanisms that contribute to this stabilization.

1.2 ORGANIZATION OF THE DISSERTATION

The dissertation is organized into five chapters, starting with this introductory chapter that provides a background on geosynthetic stabilization of roadways, accelerated pavement testing, and instrumentation of pavement structures. This is followed by three chapters (2, 3, and 4) that are self-contained studies prepared as stand-alone journal manuscripts, each with their own abstract, introduction, testing methodology, results, discussion, conclusions, and references. The final chapter is a summary of some of the key findings from each of the three studies, followed by future research potential of the work covered in the dissertation. A brief overview of the material covered in each of the three independent studies is provided below.

Chapter 2 goes over the development of an Accelerated Pavement Testing (APT) facility to test reduced-scale pavement sections under controlled-laboratory conditions.

An overview of the pavement section layout, the materials used for the construction of the pavement section, the accelerated loading device, and the comprehensive instrumentation layout used to assess the pavement section performance are discussed. A 2D laser profilometer is designed, developed, and built in-house in order to measure the vertical profile of the surface of the pavement sections. These profiles are subsequently processed in order to obtain the surface rut. A unique particle tracking sensor is developed, by combining the concepts of flexible mechanical extensometers, and linear position transducers, to measure the horizontal particle displacements in the base layer. The displacements measured at discrete points at the same depth within the base aggregate matrix is fitted with a function that captures the physical characteristics of the displacement data. The fitting parameters of the function are interpolated with depth to obtain the horizontal displacement field, horizontal normal strain field, and shear transfer efficiency plot. Explanations on the compatibility of the observed surface deformations with the internal particle displacements, along with the variation of the average volumetric dilation (with respect to depth) across the width of the pavement section are provided. Finally, the measurement of the dynamic increase in vertical stress at various points within the pavement structure from the installed earth pressure cells, and the fitting of the earth pressure cell data with a parameterized Boussinesq's equation is discussed.

In chapter 3, the techniques developed in chapter 2 for the evaluation of the performance of reduced-scale pavement section under accelerated pavement loading is utilized to assess the performance of two identical control sections without geogrid and one stabilized section with geogrid, but identical to the control in all other respects. Two identical control sections are evaluated to assess the repeatability of the construction techniques, the as-constructed properties of the pavement materials, the measurement techniques used for measuring surface deformation, and internal particle displacements.

The comparison between the control and stabilized sections are aimed at identifying the mechanisms associated with the stabilization of the aggregate base with the geogrids. The inclusion of the geogrid within the base aggregate matrix resulting in a narrower surface rut path with increased surface heave due to distribution of relative particle movements with depth in the base. The path of aggregate flow in the base under surface deformations is redirected to flow more laterally above the geogrid which is further restrained by the interlocking of the flowing aggregates with the geogrid. The manifestation of the restrained lateral flow as improved base layer moduli is observed in the redistribution of the internal vertical stresses induced by the applied surface load.

Chapter 4 discussed the most mechanistically relevant properties that contribute to the stabilization of the aggregate base by geogrids. Accelerated pavement tests are conducted on eight reduced-scale pavement sections consisting of seven sections stabilized with different geogrids and one section without a geogrid serving as the control against which the stabilized sections are compared. The performance of the pavement sections are evaluated from the surface rut profiles obtained from the 1D laser profilometer developed for this study. The pavement surface rut profiles are fit with shape functions that uniquely characterized the shape of the deformed surface for each of the pavement sections. From the shape sections, the position of the heave relative to the wheel path, and the magnitude of the heave relative to the vertical deformation under the wheel path are obtained. The benefits of stabilization with the geogrid are obtained as traffic benefit ratio (TBR) by comparing the rut in the stabilized section with that in the control. The shape of the rut profiles were found to be uniquely correlated to the traffic benefit ratio implying that the extent of stabilization provided by the geogrids affects the development of deformation on the surface. Further, the TBRs obtained from the accelerated pavement tests are correlated with several geometric and tensile properties of

the geogrids used. Several wide-width (multi-rib) tensile tests are conducted in order to obtain the tensile properties such as tensile stiffness and ultimate tensile strength. The geometric and tensile properties of the geogrid in-isolation are not found to be good indicators of performance of the geogrids in stabilization. Several soil-geosynthetic interaction tests are conducted with the aggregate base and the seven geogrids used in the APT program, in order to obtain the two interaction properties, namely pull-out resistance and the soil-geosynthetic composite stiffness. TBR showed poor correlation with the pull-out resistance in a reduced-scale pull-out test. However, the TBRs are found to be highly linearly correlated to the coefficient of the soil-geosynthetic composite stiffnesses. Thus, the K_{SGC} of the soil-geogrid composite is identified as the mechanistically relevant property capable of predicting the performance of geogrid-stabilized aggregate layers in flexible pavement.

Chapter 6 includes a summary of the key findings from the three independent, self-contained studies, followed by the potential for further research.

REFERENCES

AASHTO R50, 2009. Standard Practice for Geosynthetic Reinforcement of the Aggregate Base Course of Flexible Pavement Structures.

Al-Qadi, I.L., Brandon, T.L., Bhutta, S.A., 1997. Geosynthetic Stabilized Flexible Pavements, in: Proceedings of the Conference Geosynthetics ’97. Presented at the Geosynthetics ’97, Long Beach, CA, USA.

Bender, D.A., Barenberg, E.J., 1978. Design and behavior of soil-fabric-aggregate systems. Transportation Research Record.

Berg, R.R., Christopher, B.R., Perkins, S., 2000. Geosynthetic Reinforcement of the Aggregate Base/Sub-base course of pavement structures. GMA White Paper - II.

Brown, S., Jones, C., Brodrick, B., 1982. USE OF NON-WOVEN FABRICS IN PERMANENT ROAD PAVEMENTS. Proceedings of the Institution of Civil Engineers 73, 541–563.

Chan, F., Barksdale, R.D., Brown, S.F., 1989. Aggregate base reinforcement of surfaced pavements. Geotextiles and Geomembranes 8, 165–189.

Giroud, J., Han, J., 2004a. Design Method for Geogrid-Reinforced Unpaved Roads. I. Development of Design Method 12.

Giroud, J., Han, J., 2004b. Design Method for Geogrid-Reinforced Unpaved Roads. II. Calibration and Applications 11.

Haas, R., Walls, J., Carroll, R.G., 1988. Geogrid Reinforcement of Granular Bases I• n Flexible Pavements 9.

Halliday, A., Potter, J., 1984. The performance of a flexible pavement constructed on a strong fabric. TRRL Laboratory Report.

Holtz, R.D., Christopher, B.R., Berg, R.R., 1998. GEOSYNTHETIC DESIGN AND CONSTRUCTION GUIDELINES. PARTICIPANT NOTEBOOK. NHI COURSE NO. 13213 (No. FHWA-HI-95-038).

Kinney, T., Barenberg, E., 1982. The strengthening effect of geotextiles on soil-geotextile-aggregate systems. Presented at the Proceedings of the second international conference on geotextiles, Las Vegas, NV, USA, pp. 347–352.

Roodi, G.H., Zornberg, J.G., 2017. Stiffness of Soil-Geosynthetic Composite under Small Displacements. II: Experimental Evaluation. J. Geotech. Geoenviron. Eng. 143, 04017076. https://doi.org/10.1061/(ASCE)GT.1943-5606.0001769

Ruddock, E., Potter, J., McAvoy, A., 1982. A full-scale experiment on granular and bituminous road pavements laid on fabrics. Presented at the Proceedings of the Second International Conference on Geotextiles, pp. 365–370.

Smith, T., Brandon, T., Al-Qadi, I., Lacina, B., Bhutta, S., Hoffman, S., 1995. Laboratory Behavior of Geogrid and Geotextile Reinforced Flexible Pavements. Final Report Submitted to Atlantic Construction Fabrics, Inc. Amoco Fibers and Fabrics Company and the Virginia Center for Innovative Technology, February, Virginia Polytechnic Institute and State University, Department of Civil Engineering, Blacksburg, VA, USA.

Tingle, J.S., Jersey, S.R., 2009. Full-Scale Evaluation of Geosynthetic-Reinforced Aggregate Roads. Transportation Research Record 12.

Tingle, J.S., Webster, S.L., 2003. Corps of Engineers Design of Geosynthetic-Reinforced Unpaved Roads. Transportation Research Record 9.

Webster, S.L., Watkins, J.E., 1977. Investigation of construction techniques for tactical bridge approach roads across soft ground. US Waterways Experiment Station 2.

Chapter 2: Tracking Particle Displacements in Unbound Aggregate Layers of Roadways

ABSTRACT

Accelerated pavement tests were conducted on reduced-scale pavement sections under controlled environmental conditions using the model Mobile Load Simulator (MLS11). A unique monitoring system was developed as part of this study to evaluate the response of the pavement sections under rolling wheel loads. The performance of the sections with an increasing number of wheel passes was evaluated by measuring the surface rutting as well as the subsurface displacement of particles within the base layer. The sections were built in modular frames constructed above grade to facilitate access to the particles within the base layer from the sides of the frame. Surface rutting was measured intermittently using an in-house developed laser profilometer. A unique, cost-effective assembly of 30 linear position transducers was designed to continuously track the displacements of artificial particles within the base layer. The displacements, measured with the new system, were found to be particularly suitable to generate horizontal permanent displacement fields and strain fields. Overall, the new developments allowed comprehensive monitoring of the internal response of pavements subjected to wheel loading.

2.1 INTRODUCTION

Pavement performance is quantified by the period of time over which a given volume of traffic can be provided with an acceptable level of service by the road. The concept of acceptable levels of serviceability can be traced back to AASHO (American Association of State Highway Officials) road tests conducted in the 1960s. The Present Serviceability Rating (PSR), developed during these road tests, is a direct, subjective

measure of the level of service offered by a road at any given time. Since then, the evaluation of serviceability has moved from subjective measures (such as PSR) to more quantifiable objective measures such as the Pavement Serviceability Index (PSI), which is a function of measurable quantities including slope variance, length of cracking and surface rutting. PSI has been widely adopted as the measure of pavement performance since its inclusion in the AASHTO (American Association of State Highway and Transportation Officials) 1993 Pavement Design Method. Today, the Mechanistic-Empirical Pavement Design Guide (MEPDG, 2004), developed by AASHTO, involves designing pavements using limits on the various parameters that govern PSI, namely rutting and cracking.

The aforementioned methods evaluate changes in serviceability as a function of surface conditions. However, distress at the pavement surface is merely a symptom of the overall response within the pavement structure. As an example, while rutting is measured at the pavement surface, the total deformation at the surface is the cumulative sum of the change in thickness due to compression and lateral movements of the various underlying pavement layers. Similarly, while fatigue cracking is observed at the surface, the development of such cracks is directly related to the elastic tensile strains induced due to vehicular traffic load at critical locations within the asphalt layers. Thus, to improve pavement performance, the internal response of the pavement structure to external influences, such as environmental conditions and traffic loads, must be quantified and linked to the as-built characteristics of the pavement such as the modulus and thickness of its various layers. For instance, it can be hypothesized that restricting the internal movement of particles would also restrict the compression and lateral movement of internal layers, thereby reducing surface rutting. Accordingly, restricting internal movements to control surface rutting would require knowledge of the location, magnitude

and direction of such movements. Furthermore, monitoring the internal movement of particles could provide insight into the internal mechanisms that the road undergoes under external loads.

Although modern design methods and pavement evaluations consider internal stresses, strains and displacements in their methodologies, these internal parameters have been assessed primarily by predicting them through analytical (layered elastic analysis) or numerical (finite element or finite differences methods) means. While localized measurements of stresses and strains have been collected in some pavement studies via earth pressure cells and strain gauges, they employed expensive, single-use sensors that precluded obtaining comprehensive internal stress-strain distribution profiles. This is especially true when measuring strains/displacements within a pavement system, as continuous profiling may require a network of daisy-chained strain gauges that are not only cost-prohibitive but also intrusive, therefore possibly interfering with pavement response being quantified.

This paper introduces a cost-effective, novel method of monitoring internal particle movements within the unbound aggregate layers of a pavement structure. The method discussed herein combines mechanical extensometers used to monitor displacements in structures such as slopes and earth-retaining structures in the field (e.g., Zornberg et al., 1995) with low-cost external linear position transducers that accurately record the position of tell-tales. In the case of permanent structures, externalizing the sensors facilitates their reuse. Only the tell-tales are lost to the structure of the test sections, and these can be economically replaced. In addition to the particle tracking system, the pavement structure tested in this study was monitored using a 2D laser profilometer, also developed as part of this study to measure surface rutting as well as earth pressure cells to measure the stress distribution within the pavement structure.

2.2 MATERIALS AND METHODS

2.2.1 Pavement Layers

The reduced-scale pavement structure constructed for this study consisted of a 150-mm sand subgrade layer, 125-mm gravel base layer and 25-mm Hot Mix Asphalt (HMA) ride surface. The entire structure was built above grade in two modular frames, each measuring 150 mm in height, to facilitate access to the sensors from the sides of the frame. The pavement structure was 1800 mm in length, 1200 mm in width and had a total depth of 300 mm, as shown in Figure 2.1. A lightweight non-woven geotextile with very low tensile strength was used for separation between the base and subgrade, and a biaxial geogrid was placed 75 mm below the HMA surface within the base for stabilization.

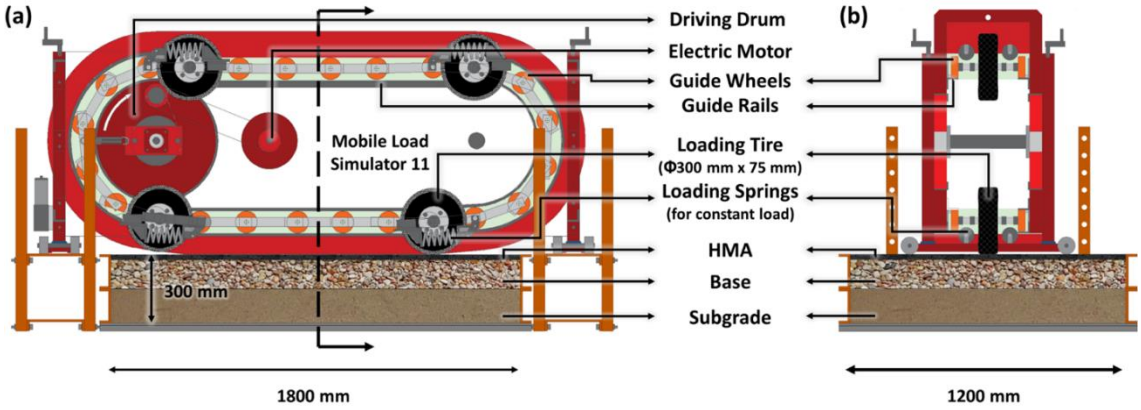

Figure 2.1. Schematic of pavement cross-section with MLS11: (a) longitudinal (b) transverse

A clean, uniformly graded sand with a D_{50} of 0.5 mm and specific gravity of 2.655, commercialized as Monterey 0/30 sand, was used as the subgrade. It classified as a poorly graded sand (SP) with a Coefficient of Uniformity (CU) of 1.8 and a Coefficient of Curvature (CC) of 1.0. The subgrade was placed in three lifts of 50 mm each, reaching

a total thickness of 150 mm. The subgrade lifts were compacted via hand tampers to a dry unit weight of 15.4 kN/m^3, corresponding to a relative density of 67%.

The base layer consisted of a clean, uniformly graded, river-washed gravel with a D_{50} of 7 mm and a specific gravity of 2.650. The base material conformed to AASHTO #8 gradation and classified as a poorly graded gravel (GP), with a CU of 1.6 and CC of 1.0. The base was placed in four 25-mm lifts and two 12.5-mm lifts, reaching a total thickness of 125 mm. The lifts were compacted via hand tampers to a dry unit weight of 17.1 kN/m^3, corresponding to a relative density of 85%.

The asphalt mixture used for the surface layer was a Thin Overlay Mix (TOM) (class A), which conformed to TxDOT Special Specification 3239 (TxDOT SS3239, 2004) and had a binder content of 6.5%.

2.2.2 Trafficking Equipment

A model Mobile Load Simulator [MLS11, previously referred to as MMLS (Kim et al., 1998; J. Lee et al., 2006)] was used to traffic the pavement sections. It consists of four loading tires connected to a chain of guide wheels that are guided along rails in a vertical obround path. The chain of guide wheels is propelled by a driving drum connected to an electric motor. This system allows repeated, unidirectional, rolling wheel loads of 2.1 kN at tire pressures of 620 kPa to be applied to the pavement surface over a track length of 1.1 m. The MLS11 is lowered onto the pavement surface using four positioning screws at the ends while a loading spring and hinge mechanism attached to each loading tire ensures the applied load remains constant with surface deformations (up to 12 mm). Table 2.1 provides further technical specifications of the loading equipment.

Property	Specification
No. of Loading Tires	4
Wheel Diameter	300 mm
Tire Width	80 mm
Total Track Width	80 mm
Total Track Length	1100 mm
Load per wheel	2.1 kN
Tire contact pressure	620 kPa
Tire footprint area	34 cm2
Loading Rate	120 passes per minute
Wheel velocity	2.5 m/s
Lateral wander	Disabled

Table 2.1. Relevant technical specifications of MLS11 equipment used in this study.

The MLS11 was originally developed in a pilot study, as a reduced-scale model of the full-scale accelerated pavement testing devices such as the MLS30 and MLS66 (van de Ven and Smit, 2000). Because of its reduced-scale, the MLS11 has a smaller tire footprint (contact area) compared to the full-scale load simulators and hence a reduced depth of influence of the applied load. Therefore, the MLS11 was predominantly used to evaluate the surface layer of full-scale flexible pavements in the field and for comparisons against full-scale vehicular load simulators (Epps et al., 2001; Gehrig et al., 2010; Martin et al., 2003; Smit et al., 2003, 1999; Walubita, 2000; Walubita et al., 2000). These field sections were predominantly non-instrumented, and their performances were primarily evaluated through the surface distress development such as rutting. In the

laboratory, the MLS11 has been used to determine and validate the performance of bituminous mixtures through the construction and trafficking of asphalt concrete slabs over an elastic medium such as polymeric foams or neoprene rubber (Bhattacharjee and Mallick, 2012; S. J. Lee et al., 2006; Lee and Kim, 2004). The asphalt slabs in these studies were typically instrumented with strip-type strain gauges to measure the elastic and plastic tensile strain development under the wheel path. This information was used to evaluate the rutting and fatigue characteristics of the various HMA mixtures used in these studies. (Kim et al., 2009) used the MLS11 to run accelerated pavement tests on asphalt slabs reinforced with carbon FRP (Fiber Reinforced Plastic) supported on cellular rubber pads. The asphalt slabs were instrumented with strain gauges which showed a 10-15% reduction in tensile strains in the transverse and longitudinal directions in the slabs reinforced with carbon-FRP. Lee et al., (2015) evaluated the performance of geosynthetic-reinforced asphalt slabs supported on top of a rigid steel plate. The mechanisms of shear flow associated with lateral movement of the pavement layers were observed under the MLS11 loading demonstrating the ability of the MLS11 loading to capture mechanisms associated with pavement surface deformations. Limited research is available on the use of MLS11 to evaluate the performance of the base and subgrade layers of reduced-scale pavement structures. Tang et al., (2008) performed accelerated pavement tests on reduced-scale pavement sections consisting of the subgrade, base and HMA surface layers. The performance of the various sections was evaluated through surface profiling in order to determine pavement ruts with increasing traffic cycles. Reduced-scale pavement sections (with subgrade, base and HMA layers) with instrumentation to measure the elastic subgrade deformations under the rolling wheel load and the cumulative subgrade rutting were studied by Tang et al., (2014). The instrumented setup consisted of an LVDT to measure the subgrade deformation and foil-

type strain gauges to measure strains in the stabilizing geogrid. A rigid pavement structure consisting of disjointed concrete slabs, on top of a silty aggregate sub-base and a non-plastic silty subgrade was trafficked using the MLS11 by Kermani et al., (2018) in order to study the fines migration and pumping commonly observed in full-scale rigid pavements. The pavement response, in terms of internal stress distribution at the interface between the sub-base and the subgrade, and the pore water pressure within the subgrade were monitored using earth pressure cells and piezometers, respectively. A review of the available literature showed no studies that report the instrumented response of the aggregate base in reduced-scale pavement sections under accelerated pavement testing under MLS11.

2.2.3 Instrumentation

The instrumentation used to monitor the performance of the pavement sections included a 2D surface profilometer to measure the surface rutting of the pavement structure; earth pressure cells to measure the vertical stress under the wheel load at specific locations within the pavement structure; and artificial particles to facilitate tracking the horizontal movement of particles within the base layer.

Profilometer

An industrial 2D laser from Micro-epsilon (model LLT2500-100) was used to develop a profiling system suitable to capture surface deformations. This laser is capable of scanning up to 300 profiles per second, with each profile consisting of roughly 640 points distributed over a width of 100 mm (roughly one sample point for every 150 microns). This laser was mounted on a glide cart that glides back and forth along a linear belt-driven actuator (Macron Dynamics Part: MSA-PSC-O-GB-AM3-2000). The actuator

consists of a 2.4-m-long extruded aluminum section, with a maximum travel length of 2.06 m, driven by an integrated stepSERVO^{TM} motor (Applied Motion Products TSM23Q-2RG) capable of displacing the profiling laser at variable speeds of 1 mm/s to 1200 mm/s. Two inductive proximity sensors are used as hardware end limit switches on either ends of the actuator resulting in 2 m of usable travel. These limits may be further adjusted based on the width of the test sections by either physically moving the end limit switches or setting up software end limits through the Step-Servo Quick Tuner software. For the purposes of this study, the actuator operated at 25 mm/s with the laser scanning 25 profiles per second, resulting in a sampling frequency of one profile per mm of pavement section.

Pavement surface profiling was completed pre-trafficking before testing commenced, at pre-determined intervals during trafficking, and post-trafficking after pavement failure. To determine the progression of the surface rut with an increasing number of wheel passes, trafficking was interrupted at pre-determined intervals (after 100, 1000, 3000, 10000 and 20000 passes from the start of testing), the MLS11 was removed from the pavement section, and the pavement surface was profiled along four different locations as depicted in Figure 2.2. Thus, a complete pavement profile consisted of one longitudinal profile (labeled ‘Long’ in Figure 2.2) along the path of trafficking, and three transverse profiles (labeled ‘Begin,’ ‘Center’ and ‘End’ in Figure 2.2) perpendicular to the direction of trafficking, each spaced 250 mm apart.

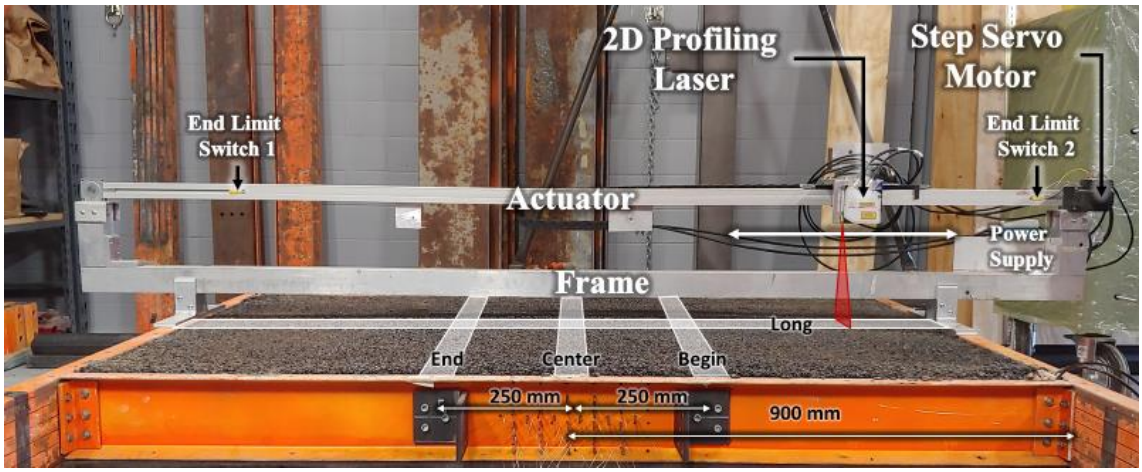

Figure 2.2. Assembled laser profilometer.

Earth Pressure Cell

The earth pressure cells selected for this study were KDC and KDE sensors from Tokyo Measuring Instruments Lab (TML), rated for 500 and 200 kPa vertical compressive stress. These sensors are 350 Ω full-bridge strain-gauge-based pressure cells that were designed to be embedded within soil. Eight sensors were used within the pavement section to capture the vertical stress distribution. The three larger KDC sensors were placed near the mid-depth of the base layer. Three of the five smaller KDE sensors were placed at the base-subgrade interface beneath the non-woven geotextile while the remaining two were placed at the bottom of the subgrade. Figure 2.3 displays the layout of all eight earth pressure cells within the pavement structure. The sensors were staggered to avoid being installed atop one another to prevent local stiffening given the pavement layer thicknesses and profile of the sensors. Figure 2.4 shows the KDE pressure cells installed on top of the subgrade with a biaxial level to ensure that the sensors are vertical.

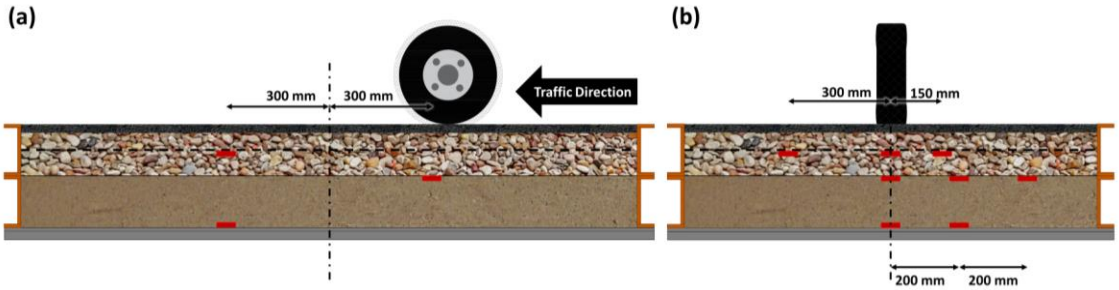

Figure 2.3. Pressure cell layout: (a) longitudinal cross-section; and (b) transverse cross-section.

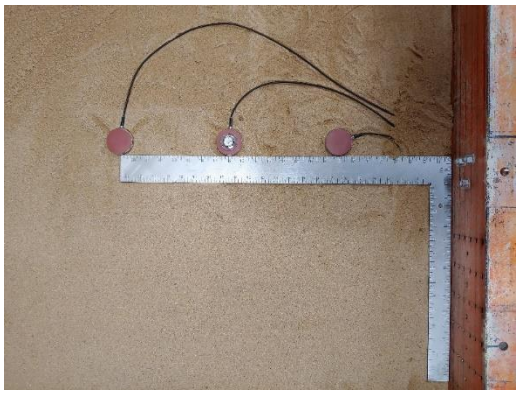

Figure 2.4. KDE pressure cells installed on top of subgrade.

Particle Tracking Sensor

Pavement surface rutting may result from the movement of particles within the various pavement layers. This mechanism has been recognized in modern mechanistic design methods wherein the surface rut is computed as the arithmetic sum of the rutting contributions by the individual pavement layers (MEPDG 2004). From the mechanistic point of view, the component of the rut attributed to the unbound aggregate base can be classified into two types: (1) one-dimensional densification of the unbound pavement layer under wheel loads, and (2) lateral flow due to incremental shear of the pavement layers with repeated traffic passes. For an adequately compacted unbound aggregate

layer, the component of rutting due to densification can be considered negligible. Thus, for well-compacted unbound aggregate layers, any vertical settlement under wheel loads attributed to the base layer must be accompanied by a corresponding lateral flow or horizontal displacement of the aggregate particles. Observing the lateral displacement of particles under trafficking is expected to provide significant insight into the development and progression of rutting in unbound aggregate layers.

In this study, the lateral movements of aggregate particles induced by wheel passes were monitored using a unique setup that combined mechanical extensometers, typically used in field embankments to monitor soil movement, with linear displacement sensors. This setup consists of artificial particles embedded within the soil matrix and tied to tell-tale wires spanning the pavement structure, the other ends of which are connected to linear position transducers mounted outside the pavement structure. As a result, any particle movement within the base is transferred through the tell-tale wires to the position sensors on the sides of the pavement structure.

The artificial particles were fabricated using a 9-mm-long, 6.5-mm-wide stainless-steel hex bolt (8-32 thread) and a 6.5-mm-wide, 2.5-mm-thick hex nut. The final profile of a fully assembled artificial particle comprises a 6.5-mm-wide, 5-mm-tall hex-head with a 4-mm-wide, 4-mm-tall threaded base (Figure 2.5a). The following steps were taken to improve the interaction between the artificial particles and the surrounding aggregate particles: (1) the final profile of the artificial particles was selected to correspond closely to the D_{50} of the base material (7 mm); (2) the hex nuts and bolts were chosen due to their shape with sharp edges and threaded base; (3) the polished surfaces of the hex nuts and bolts were sanded with a coarse-grit sandpaper; and (4) the particles were installed with the axis of the bolt-nut assembly perpendicular to the direction of the tell-tale.

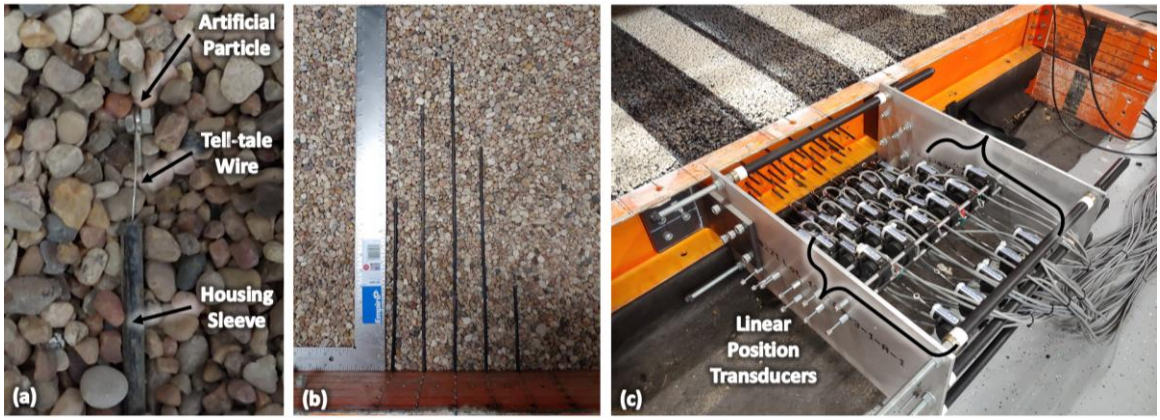

Figure 2.5. Particle tracking assembly (a) artificial particle connected to tell-tales (b) housing sleeves run from artificial particles to outside of box; and (c) linear position transducers mounted onto overhanging frame.

A total of 30 artificial particles were installed within the base, forming a dense array of trackable particles as displayed in Figure 2.6. They were installed in six layers at a vertical spacing of 25 mm, with five sensors per layer located 75 mm, 150 mm, 225 mm, 300 mm, and 450 mm laterally away from the location of the wheel path. Since each artificial particle was connected to a linear potentiometer outside the pavement structure, the five sensors installed at the same depth in each layer were staggered 50 mm from each other longitudinally.

Spring-back 316 stainless steel wire 0.5 mm in diameter was utilized for the tell-tale wires. These wires were looped between the nut and bolt of the artificial particles and held in place by 20-24 AWG wire ferrules crimped next to the bolt thread. The nut and bolt assemblies were also fastened to prevent any play between the tell-tale wires and artificial particles. The tell-tale wires were routed from the artificial particles located within the base to the displacement sensors located outside the pavement structure, at the sides of the modular frames. Excluding the first 40 mm from the particle, the entire

length of the tell-tale wires , was protected against possible damage using high-performance bicycle brake housing as a sleeve (Figure 2.5b). The first 40 mm remained exposed to allow for particle movements toward the edge of the pavement structure. The housing sleeve contains a Teflon-lubricated inner liner tube to reduce any friction against the sliding of the tell-tale wires to facilitate an accurate no-ply transfer of particle movement to the outside of the pavement. The liner tube is encased within the walls of the middle coiled high-carbon steel, which protects the tell-tale wires against pinching, bending and other damage from the surrounding aggregate particles. The coiled steel is covered in a polymeric outer layer to minimize any increase in resistance to aggregate particle movement near the housing.

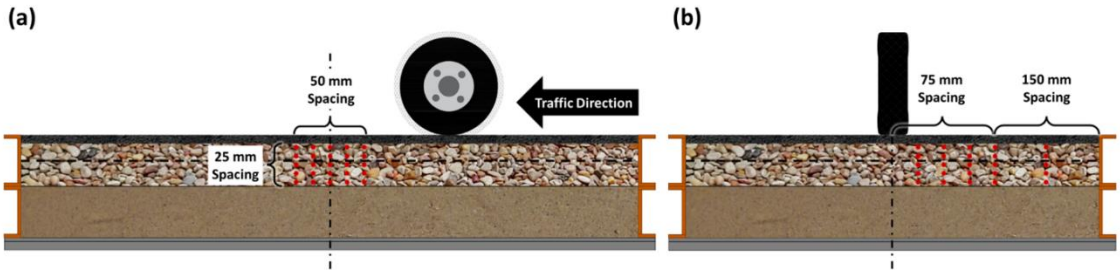

Figure 2.6. Layout of trackable artificial particles: (a) longitudinal cross-section; and (b) transverse cross-section.

The free ends of the tell-tale wires were connected to an eye fitting on the linear position transducers mounted outside the pavement structure, which measure the lateral movement of the artificial particles (Figure 2.5c). The linear position transducers from Unimeasure (LX-PA Series) are ratiometric sensors that output a fraction of the input excitation voltage according to the position of the potentiometer using a voltage divider circuit. These analog sensors divide a 1000 Ω potentiometric circuit over a range of ± 25 mm with a high degree of linearity (± 1% full-scale). Figure 2.5c shows the frame,

designed to hold over 30 sensors in a tight matrix over the edge of the pavement, to which these sensors were mounted.

2.3 RESULTS AND DISCUSSION

This section details the response of the pavement test section to trafficking by the MLS11 with no lateral wander. The pavement section was subjected to 20,000 wheel passes while the vertical stress distribution within the pavement structure and horizontal particle movements in the base layer were continuously measured. Trafficking was briefly interrupted after 100, 1000, 3000, and 10000 wheel passes to measure surface deformations using the profilometer. The initial and final surface profiles were also determined before and after the end of the trafficking cycles.

2.3.1 Surface Rutting

Figure 2.7 shows the center rut profile of the pavement section after 10,000 passes, determined by subtracting the initial center-transverse profile from that obtained after 10,000 passes. Figure 2.7a shows the profile measured by the laser profilometer as a 2D contour plot. The x-axis corresponds to the transverse distance from the center of the wheel path of the laser as it was guided across the pavement section when measuring the surface profile. The y-axis provides the lateral distance from the center of the laser perpendicular to the direction of motion. The darker center region (in blue), around 0 mm in the transverse direction, represents the area that is deeper than in the initial profile, which corresponds to the wheel path. The adjacent darker regions (in red), around ±200 mm, represent the areas that are shallower than in the initial profile, which correspond to the heave on either side of the wheel path. The lighter region between the darker red and darker blue regions shows the location of zero vertical deformation, or pivot point,

around which the pavement surface deforms. The development of rut from a depression along the wheel path accompanied by shear upheavals on either side of the wheel path is known to be associated with the lateral flow of materials in the pavement layers (MEPDG 2004).

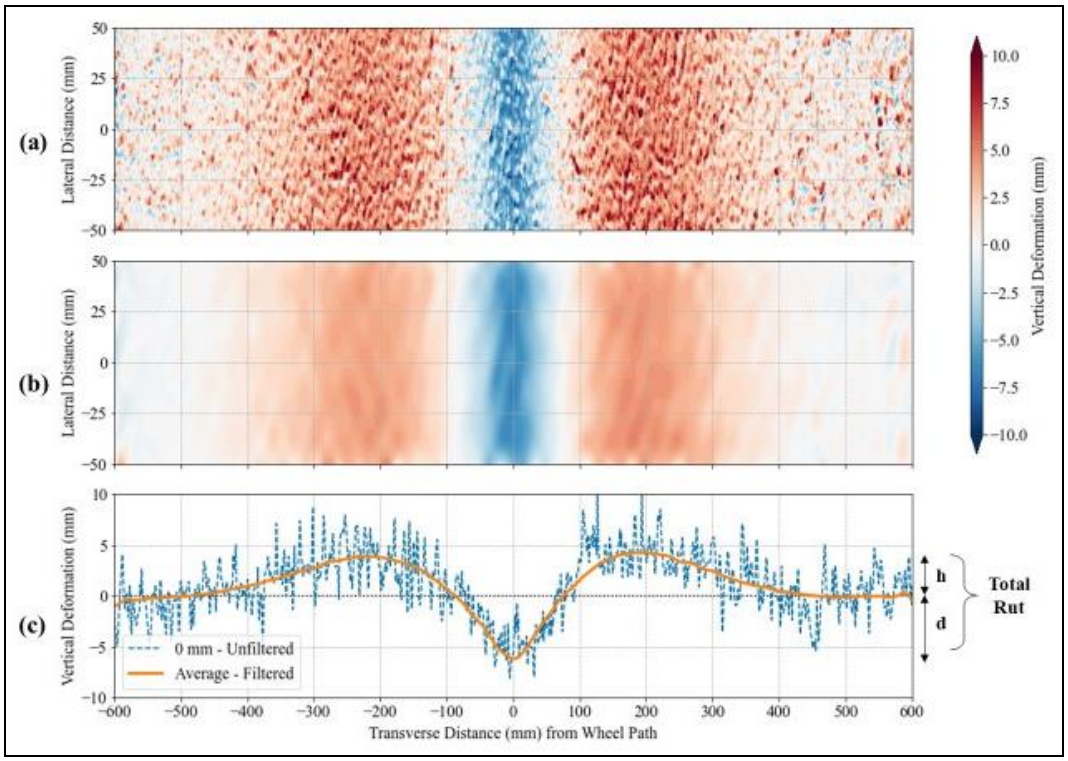

Figure 2.7. Transverse profile after 10,000 wheel passes: (a) raw 2D contour; (b) filtered 2D contour; and (c) 1D profile.

The measured profile contains high-frequency noise due to laser reflections from the sharp edges of the particles in the HMA surface. To remove this noise , the measured profile was filtered using a low-pass, 5th order Butterworth filter with a cut-off frequency of 0.035 samples/mm along both axes. Figure 2.7b shows the filtered surface profile. The

filtering attenuated the noise by 99% or more for particle sizes up to 10 mm, which is the maximum aggregate size used in the TOM-A mix of the HMA layer.

In addition to these reflection artifacts, the overall surface texture of the HMA surface also introduces some particle shape noise into the profiles. To remove the noise due to individual particles, the average transverse profile for the 100-mm lateral distance scanned by the laser was determined as indicated by the solid orange line in Figure 2.7c. This is the same data shown in Figure 2.7b but averaged along the lateral direction (y-axis). The dashed blue line in Figure 2.7c corresponds to the transverse profile measured at the center of the laser (0 mm lateral distance) before filtering. The process of averaging removed the noise due to individual particle shapes and also allowed for small errors in the lateral placement of the profilometer during profiling after various numbers of wheel passes, resulting in a clean rut profile.

Figure 2.8 shows the average profiles obtained at the transverse profile location 'Center' at increasing number of trafficking cycles. The rut progression is primarily driven by the lateral flow of base material through shearing as evidenced by: (1) the increase in heave next to the wheel path proportionate with an increase in the depression along the wheel path; and (2) the location of the transition from depression to heave remaining at a constant distance (around ±80 mm) from the center of the wheel path. From the average profiles, the total rut at the center of the pavement section is determined as the sum of the vertical depression depth (d) under the wheel path and corresponding heave (h) adjacent to the wheel path, as shown in Figure 2.9.

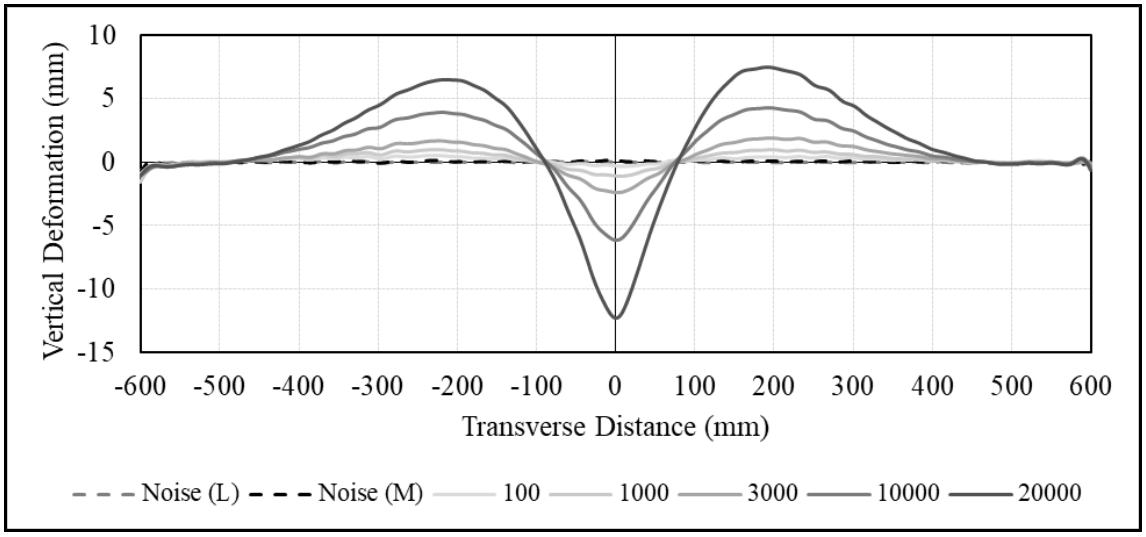

Figure 2.8. Rut profiles with increasing number of wheel passes.

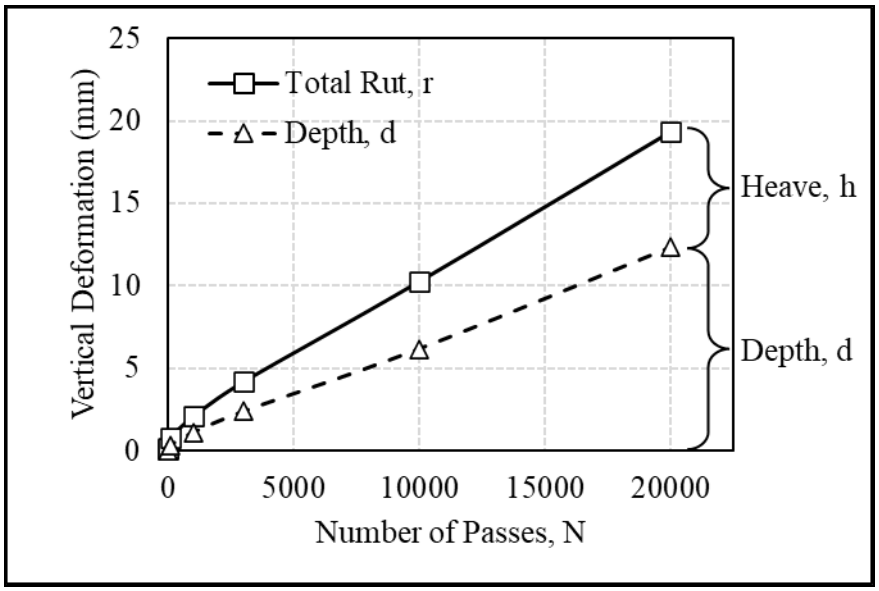

Figure 2.9. Rut, heave, and depression depth as a function of number of passes, N.

The ruts are also measured at two other transverse profile locations, ‘Begin’ and ‘End,’ which are 250 mm on either side of the ‘Center’ location. The rut measured at all three locations and their average are given in Figure 2.10. The rut measured at the center

of the trafficked length is very close to the average of all three locations. In contrast, the ruts measured at ‘End’ are higher than the average and those measured at ‘Begin’ are lower than the average by less than 15%, which is considered acceptable for the purposes of this study.

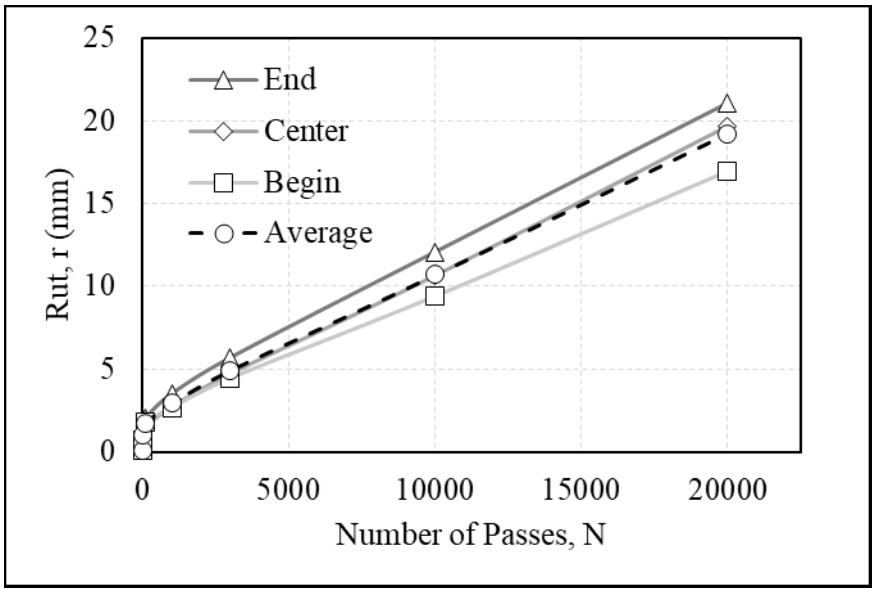

Figure 2.10. Rut vs. number of passes along pavement section.

2.3.2 Sub-surface Displacements

As previously described, the particle tracking sensor is a flexible, protected tell-tale wire connected to an artificial particle within the pavement structure on one end and to a linear position transducer on the other end. The flexible nature of the system accommodates possible vertical movements of the pavement layers without significantly affecting the measurement of horizontal displacements. An upper bound on the measurement error due to potential vertical movements of the pavement layer can be obtained by considering the vertical movements as measured by the profilometer at the surface. It is assumed that the vertical movement of pavement layers beneath the surface

results in a final subsurface profile with a larger radius of curvature (i.e., is straighter) than the surface profile. Figure 2.11 Figure 2.10illustrates the case of a particle located on the surface at the center of the wheel path (dashed square). Theoretically, this particle will undergo a maximum vertical displacement with zero horizontal displacement to reach its final position (solid square). As a result, a tell-tale wire running from this particle to the edge of the pavement would measure only the error due to the vertical displacement. Since the particle does not undergo any horizontal displacements, the vertical displacement of the pavement layer would result in an increased wire length within the pavement. Thus, the overhanging portion of the wire outside the pavement is reduced in length by ΔL, which equals the difference in the length of the surface deformation profile before and after the vertical displacement. Therefore, the error due to vertical displacements is always registered by the linear position sensor as if the particle moved toward the center of the wheel path (negative displacement by convention).

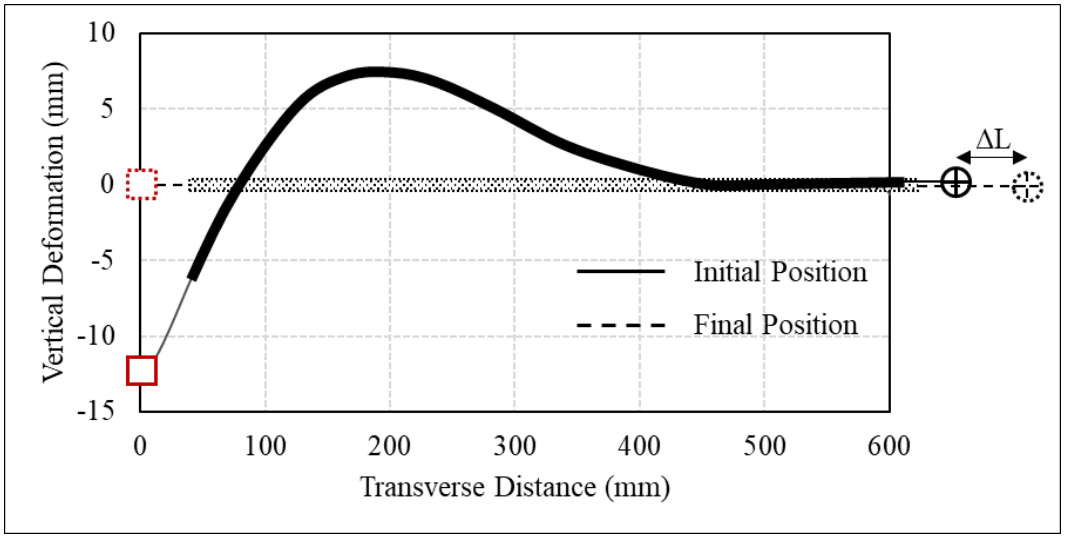

Figure 2.11. Measurement error due to vertical displacement at surface.

By calculating the length of the vertical displacement curve (i.e., surface profile) from the center of the wheel path to the edge of the pavement, and comparing it to the original length before trafficking, the maximum error in horizontal displacement measurements due to vertical displacements can be determined. Table 2.2 summarizes the maximum error in horizontal displacement measurements at increasing number of passes. As can be seen in the table, the maximum error calculated at the end of the test (after 20,000 wheel passes) is less than 1.5 mm, which is about 10% of the vertical displacement under the wheel path. This is the maximum possible error in the horizontal displacement measurement for a particle on the surface of the pavement located at the center of the wheel path. For particles within the pavement and away from the wheel path as shown in Figure 2.6, the error in horizontal displacement measurement is expected to be significantly smaller.

Considering that the subsurface profiles have a larger radius of curvature than the surface profile, a lower bound for the minimum radius of curvature of the layers within the base can be determined. The radius of curvature along the surface profile is determined from the first and second derivatives of the profile. From the surface profile obtained after 20,000 passes, the minimum radius of curvature was found to be 70 mm at the center of the wheel path. The tell-tale wires and housing sleeve were chosen such that their minimum radii (25 mm and 50 mm, respectively) were smaller than the minimum radius of curvature required (70 mm), allowing them to be flexible enough to accommodate the subsurface profile movements.

Number of passes	**Surface profile length**	**Maximum error**	**Vertical depression depth**	**Percentage of vertical displacement**
N	**2L**	**ΔL**	**d**	**ΔL/d**
	(mm)	(mm)	(mm)	(%)
0	1200.00	0.00	0.0	0.0%
100	1200.05	-0.03	0.4	7.8%
1000	1200.11	-0.05	1.1	4.8%
3000	1200.16	-0.08	2.4	3.4%
10000	1200.83	-0.42	6.2	6.7%
20000	1202.82	-1.41	12.3	11.4%

Table 2.2. Maximum error in horizontal displacements due to vertical settlement.

Figure 2.12 shows the cumulative displacements after 10,000 passes measured by the particle tracking sensors at six different depths within the base and five different transverse distances from the wheel path. The transverse horizontal displacement under the wheel path is zero due to the symmetry of displacements across the wheel path. At 600 mm from the wheel path, the transverse horizontal displacement is also zero since this is the edge of the pavement section bounded by steel channels.

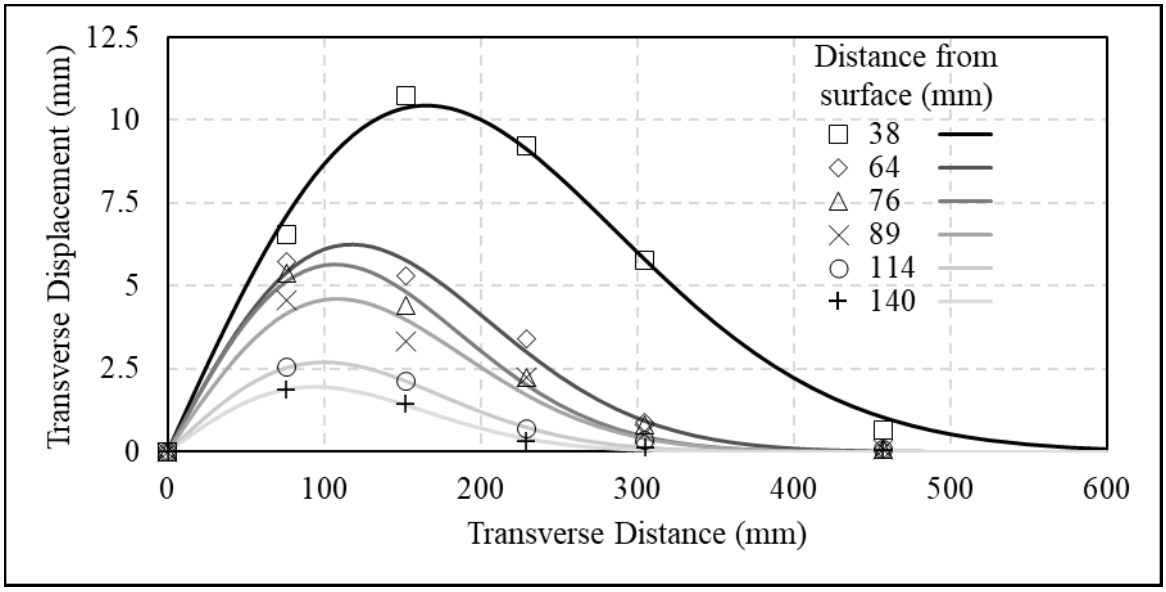

Figure 2.12. Cumulative particle displacements after 10,000 passes.

To interpolate the horizontal displacement data along the transverse direction from the wheel path, the five measured transverse displacements at any particular depth and two transverse displacements determined from the boundary conditions were fitted with a function, as indicated by the solid lines in Figure 2.12. The best-fit function representing the cumulative horizontal displacements must have properties that capture the behavior of the particles in the base under trafficking. Therefore, the function chosen to fit the transverse displacement data should:

1. be equal to zero at the origin (wheel path), where the horizontal displacement is zero due to symmetry.
2. be an 'odd' function, i.e., symmetric about the origin (wheel path), so that the transverse horizontal particle displacements are symmetric about the wheel path but reversed in direction on either side of the wheel path.
3. monotonically increases to a maximum at a given distance from the wheel path (region of tensile strains around the wheel path) and then asymptotically

decreases to zero at infinity (region of compressive strains away from the wheel path).

Among the several functions considered for fitting the transverse displacement data, the following function satisfies the above characteristics and best fit the measured data:

$$u = Axe^{-Bx^2} \tag{2.1}$$

where u is the transverse horizontal displacement away from the wheel path.

x is the transverse distance from the wheel path.

A and B are fitting parameters greater than zero.

Particle displacements at six different depths within the base layer were fitted with the function in Equation (2.1). The best-fit parameters, A and B, after 10,000 passes for each depth, z, are shown in Figure 2.13. The parameter A decreases approximately linearly with increasing depth, while the parameter B increases in a log-linear fashion with increasing depth. The linear and log-linear functions that correspond to the best fit displacement data are shown in the figure. The transverse horizontal strains are obtained as the derivative of Equation (2.1), as follows:

$$\varepsilon_x = \frac{du}{dx} = A(1 - 2Bx^2)e^{-Bx^2} \tag{2.2}$$

where ε_x is the transverse horizontal strain (tension is positive)

Setting Equation (2.2) equal to zero, the location of peak displacement can be obtained as follows.

$$A\left(1 - 2Bx_{peak}^2\right)e^{-Bx_{peak}^2} = 0$$

$$1 - 2Bx_{max}^2 = 0$$

$$x_{peak} = \pm\frac{1}{\sqrt{2B}} \qquad \text{OR} \qquad B = \frac{1}{2x_{peak}^2} \tag{2.3}$$

where x_{peak} is the location of the peak horizontal displacement from the center of the wheel path.

The magnitude of peak displacement is obtained by substituting Equation (2.3) into Equation (2.1):

$$u_{peak} = \frac{A}{\sqrt{2Be}} \qquad \text{OR} \qquad A = \frac{u_{peak}}{x_{peak}}\sqrt{e} \tag{2.4}$$

where u_{peak} is the magnitude of the peak horizontal displacement.

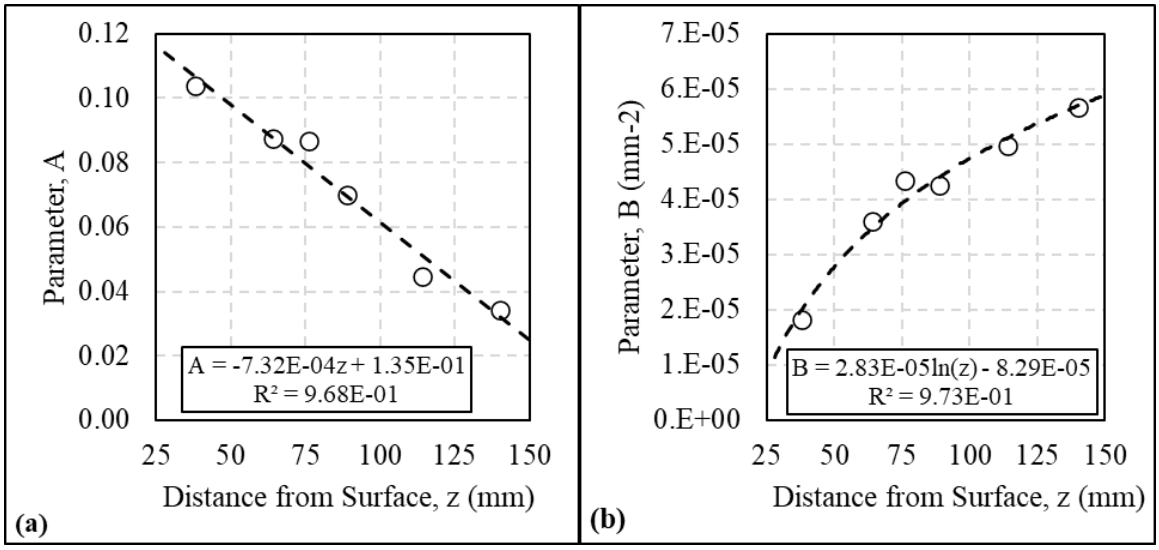

Figure 2.13. Fitting parameters vs. depth, z, after 10,000 passes: (a) parameter A; and (b) parameter B.

Figure 2.14 shows the location and magnitude of the peak horizontal displacements at various depths within the base layer after 10,000 passes. As expected, the peak displacement occurred in the layers closest to the surface and decreased with increasing depth. Interestingly, the location of the peak displacement approaches the

center of the wheel path with increasing depth. From Equation (2.2), it can be inferred that the fitting parameter A corresponds to the maximum tensile strain under the wheel path (when x = 0). Also, from Equation (2.3), the fitting parameter B correlates with the location of the peak horizontal displacement. Thus, Equation (2.1) for the horizontal displacement (and (2) for tensile strain) can be redefined using the location and magnitude of the peak horizontal displacement, as follows.

$$u = u_{peak}\left(\frac{x}{x_{peak}}\right)e^{\frac{1}{2}\left[1-\left(\frac{x}{x_{peak}}\right)^2\right]} \tag{2.5}$$

$$\varepsilon_x = \varepsilon_{x,peak}\left[1-\left(\frac{x}{x_{peak}}\right)^2\right]e^{-\frac{1}{2}\left(\frac{x}{x_{peak}}\right)^2} \tag{2.6}$$

where $\varepsilon_{x,peak}$ is the peak tensile strain under the center of the wheel path.

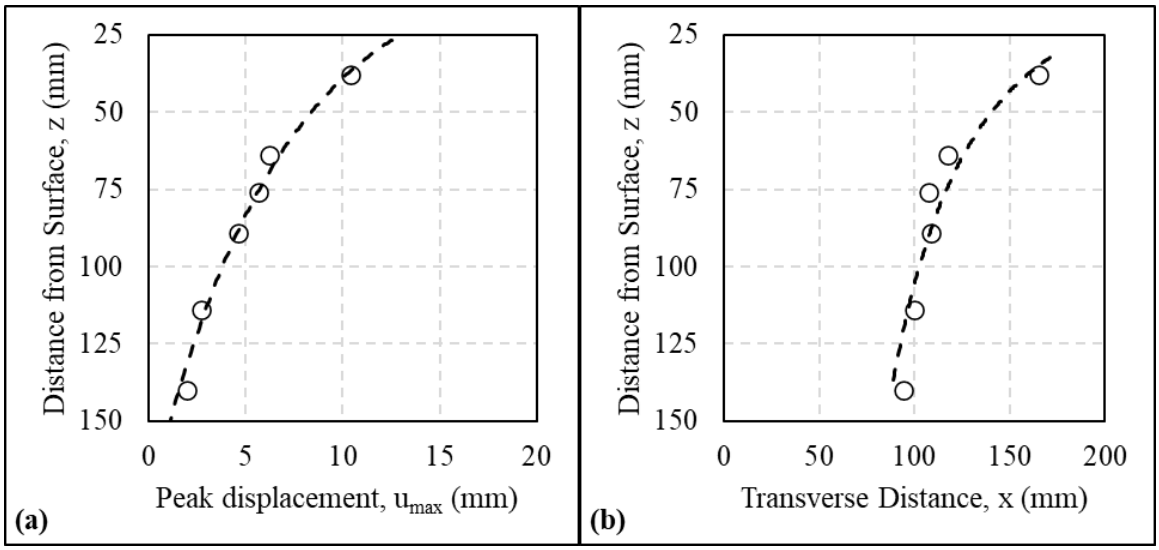

Figure 2.14. Peak displacement after 10,000 passes: (a) magnitude, u_{peak}; and (b) location, x_{peak}.

From Figure 2.13, the fitting parameters A and B for the horizontal displacement function are determined for any depth within the base layer. Consequently, Equations (1)

and (2), using the fitting parameters for a particular depth, can be used to predict the horizontal particle displacements and tensile strains at any point within the base layer. This information was used to generate the horizontal displacement fields and tensile strain fields within the base layer at increasing traffic cycles. Figure 2.15 presents the development of horizontal displacements with increasing number of wheel passes as contour plots. The x-axis of the contour plots corresponds to the distance from the wheel path in the transverse direction, with 0 mm at the center of the wheel path and 600 mm at the edge of the pavement. The y-axis corresponds to the depth from the surface of the completed pavement section, with the HMA-base layer interface at 25 mm and the base-subgrade interface at 150 mm. The contours represent the horizontal displacements, and the darker regions correspond to higher displacements. The displacement contours progress from near the HMA-base interface to the bottom of the base layer with increasing surface rut due to trafficking. Peak displacements occurred between 100 mm and 200 mm from the wheel path near the HMA-base interface. As surface rut increased, the contour level (shade of red) representing the highest displacement near the HMA-base interface became darker indicating an increase in displacement at this location. This resulted in a downward and outward movement of the pre-existing contours away from the HMA-base interface. The top-down progression of the horizontal displacement contours observed with this particular pavement configuration implied that the displacement measured is always higher closer to the surface and decreases with increase in depth. Thus, an increase in surface rut is accommodated by the lateral flow of material in the base layer, leading to the transfer of shear from the sub-layer near the top of the base to the sub-layer below, and from that sub-layer to the next, and so on, resulting in decreased displacements with increasing depth within the pavement structure. The data provide direct evidence of rutting caused by the lateral flow mechanism , as further

substantiated by: (1) the accompanying heave adjacent to the wheel path in the surface deformation profiles (Figure 2.8); and (2) the essentially linear progression of rut and heave with increasing number of wheel passes (Figure 2.9), corresponding to the secondary phase of rutting with little to no volume changes (MEPDG 2004).

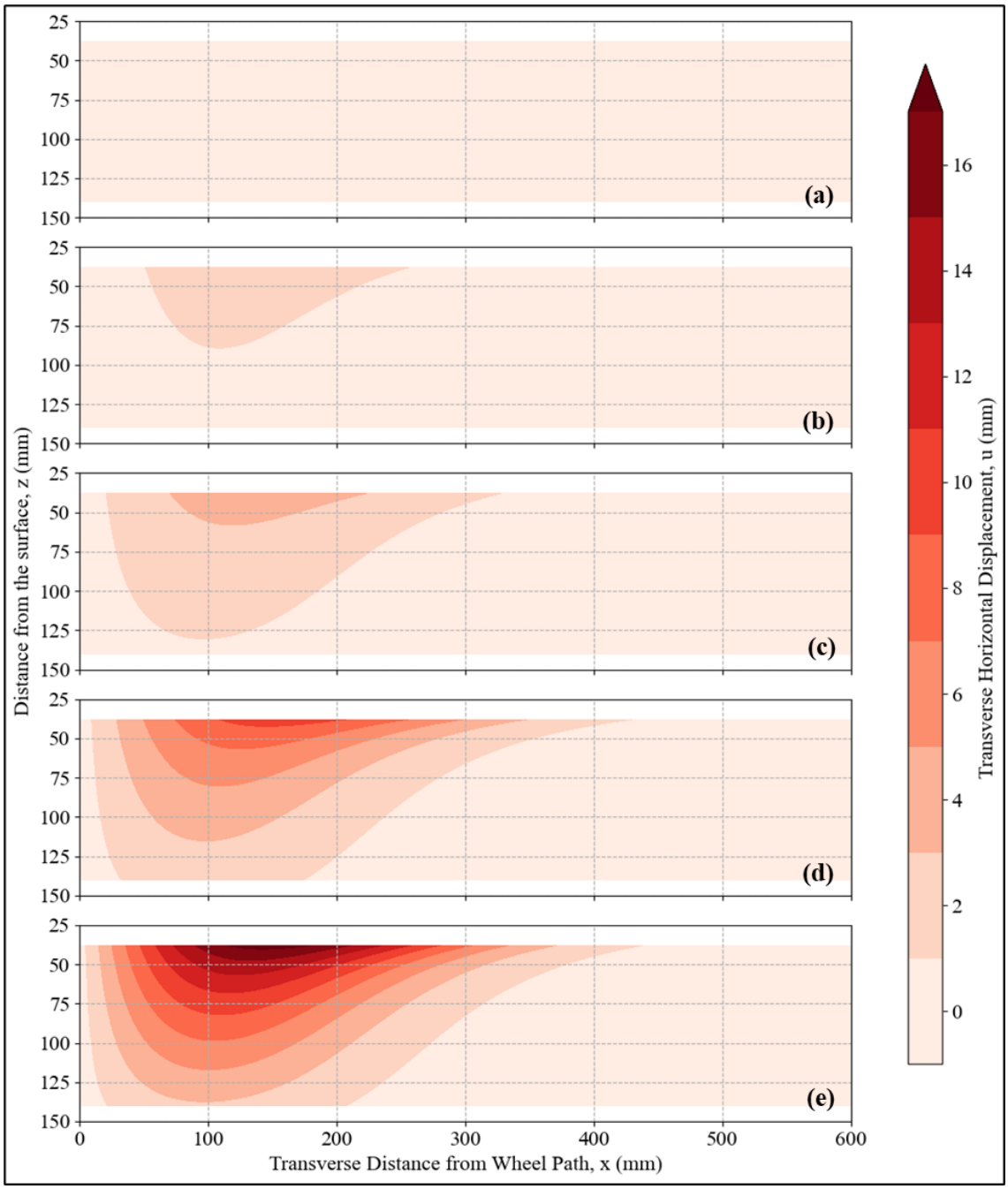

Figure 2.15. Cumulative horizontal displacements (mm) after: (a) 100; (b) 1,000; (c) 3,000; (d) 10,000; and (e) 20,000 passes.

Figure 2.16 shows the vertical gradient of horizontal displacements as contour plots with increasing trafficking cycles. The vertical gradient is a measure of one of the two components of the shear strain within the base and represents the efficiency of the shear transfer from one sub-layer of the base to the adjacent sub-layers. Light contour levels represent regions with a comparatively low vertical gradient in horizontal displacements, i.e., movement of any particle in this region is accompanied by a movement of the same degree of the vertically adjacent particles (high shear transfer efficiency). Dark the contour levels represent regions with a comparatively high vertical gradient in horizontal displacements, which implies a region with low shear transfer efficiency, i.e., movement of a particle in this region does not significantly affect the vertically adjacent particles. In the initial phases of trafficking, no significant vertical gradients were observed within the base layer, which corresponds to the initial phase of rutting with minimal shear development. The results indicate that increasing surface rut resulted in an overall increase in the vertical gradient of horizontal displacements but was found to occur near the HMA-base interface at the location of the heave in the surface deformation profiles (Figure 2.8). The base aggregates closer to the HMA-base interface experienced larger lateral flow relative to the aggregates deeper within the base due to loss of confinement from the heave on the surface, resulting in reduced shear strength closer to the surface than deeper within the base. As the base aggregates towards the surface displaced laterally, the aggregates deeper within the base developed lateral displacements through the transfer of shear, the efficiency of which increased with depth. Thus, the difference in horizontal displacements between base aggregates with change in depth was more likely to be smaller at deeper depths than at shallower depths, as seen in Figure 2.12 (the difference in displacements between sensors at depths of 38 mm and 64 mm is greater than that between 114 mm and 140 mm).

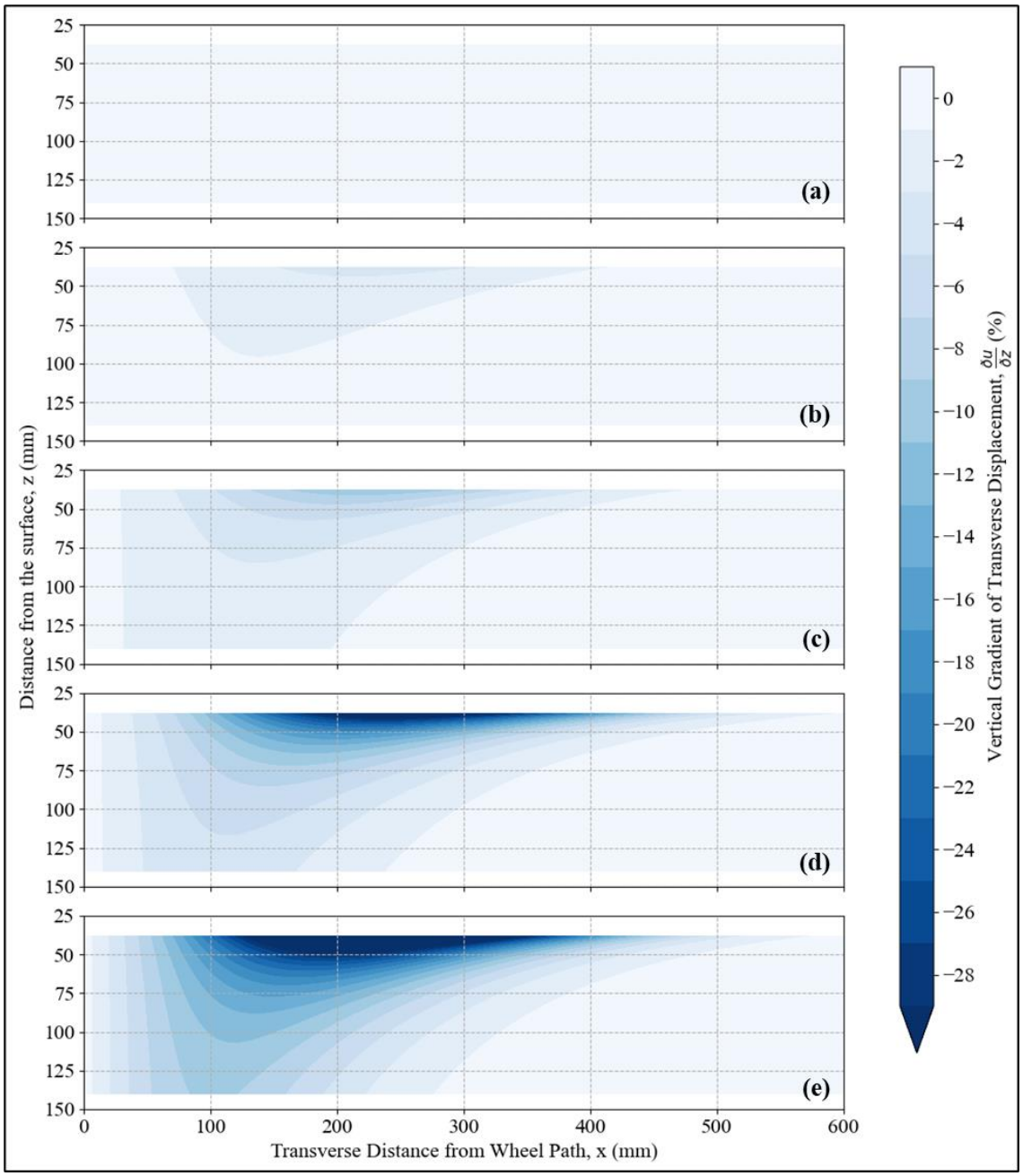

Figure 2.16. Vertical gradient of transverse displacement (%) after: (a) 100; (b) 1,000; (c) 3,000; (d) 10,000; and (e) 20,000 passes.

The horizontal tensile strains within the base with increasing trafficking are presented as contour plots in Figure 2.17. The red contours correspond to regions of tensile strains (positive) while the blue contour levels represent regions of compressive strains (negative), with darker shades representing higher strain levels (tensile or compressive depending on the color). Tensile and compressive zones within the strain field are clearly demarcated by the white (lightest) contour level (denoting near 0% strain). The tensile zone occurs in the vicinity of the wheel path, with the maximum tensile strain along occurring towards the surface at the center of the wheel path (x = 0 mm). Cumulative compressive strains developed away from the wheel path, after a zone of zero strain (white contour level), corresponding to the location of maximum displacement. Maximum compressive strains developed away from the wheel path, between 150 mm and 250 mm, near the location of the heave in the surface deformation profiles (Figure 2.8). The compressive zone is followed by a zone of undisturbed base with zero strains.

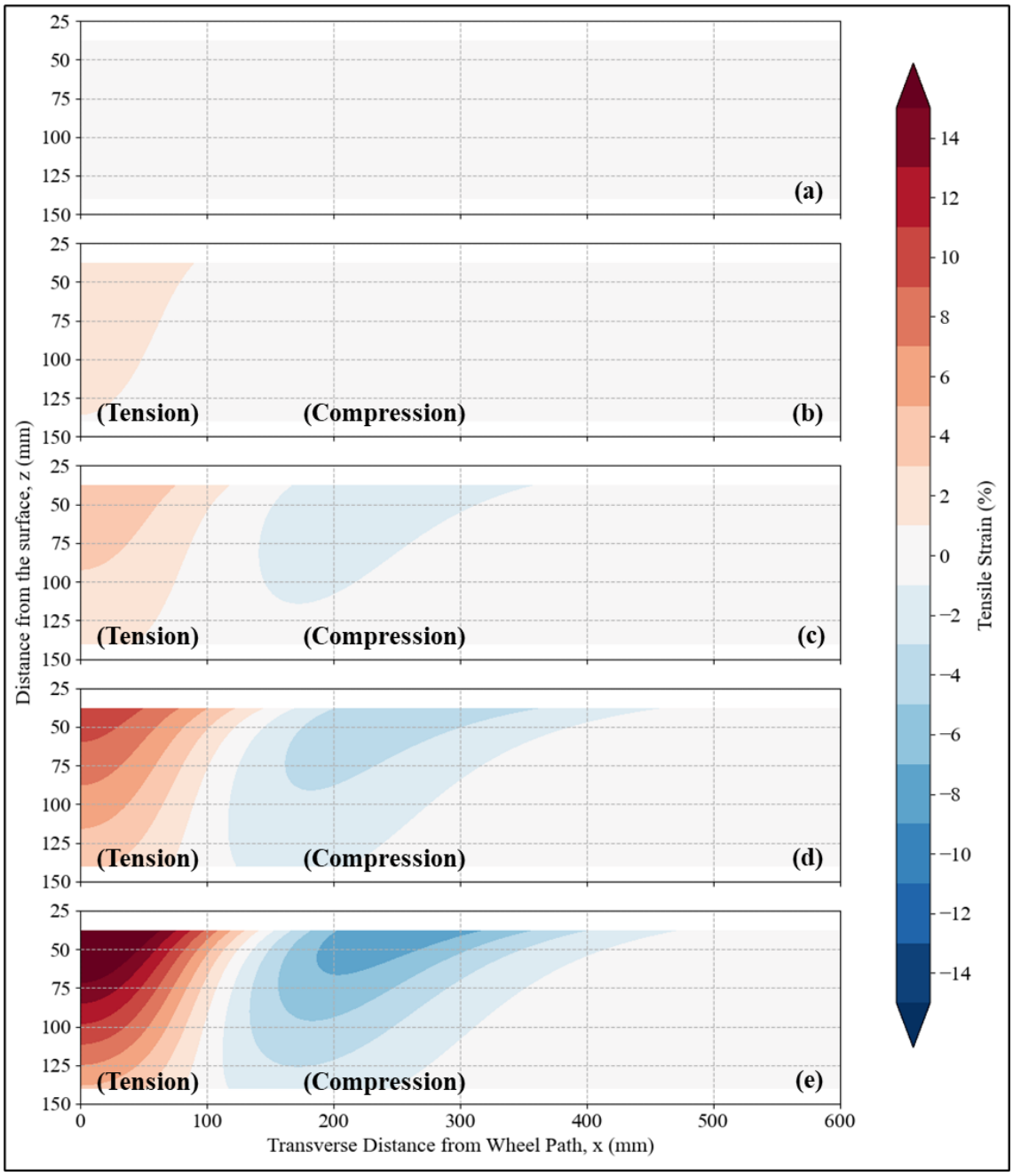

Figure 2.17. Cumulative horizontal normal strain (%) after: (a) 100; (b) 1,000; (c) 3,000; (d) 10,000; and (e) 20,000 passes.

At the end of testing, after 20,000 wheel passes, the pavement section was trenched to determine the potential change in thickness of the HMA, base and subgrade

layers. Measurements of the HMA layer thickness under the wheel path and away from the wheel path showed no significant difference, indicating that changes to the HMA layer thickness under the wheel path were negligible. Similarly, the subgrade layer thickness was measured at various locations from the center of the wheel path using a steel ruler, revealing no significant changes in thickness before and after testing. Only the base layer contributed significantly to the overall surface deformation as measured by the surface profilometer. Thus, it can be considered that the deflection profile at the HMA surface equals the change in thickness of the base layer across the pavement section. Using the initial thickness of the base (as constructed) and surface deformation profile (change in base thickness), the average vertical normal strain throughout the thickness of the base can be calculated. Figure 2.18 compares the average vertical normal strain against the average horizontal normal strain (Figure 2.17) over the thickness of the base in Figure 2.18. The x-axis in the Figure 2.corresponds to the transverse distance from the center of the wheel path, while the y-axis corresponds to the average normal strains (%) in the vertical direction (left axis) and horizontal direction (right axis - inverted). Tensile strains are shown as positive normal strains and compressive strains are shown as negative normal strains. The vertical and horizontal normal strains show good agreement, especially at distances greater than 200 mm from the wheel path, i.e., in the compressive zone of horizontal normal strains. In the tensile zone, the horizontal tensile strains were greater in magnitude for a given vertical compressive strain, indicating the base is dilatant under those conditions.

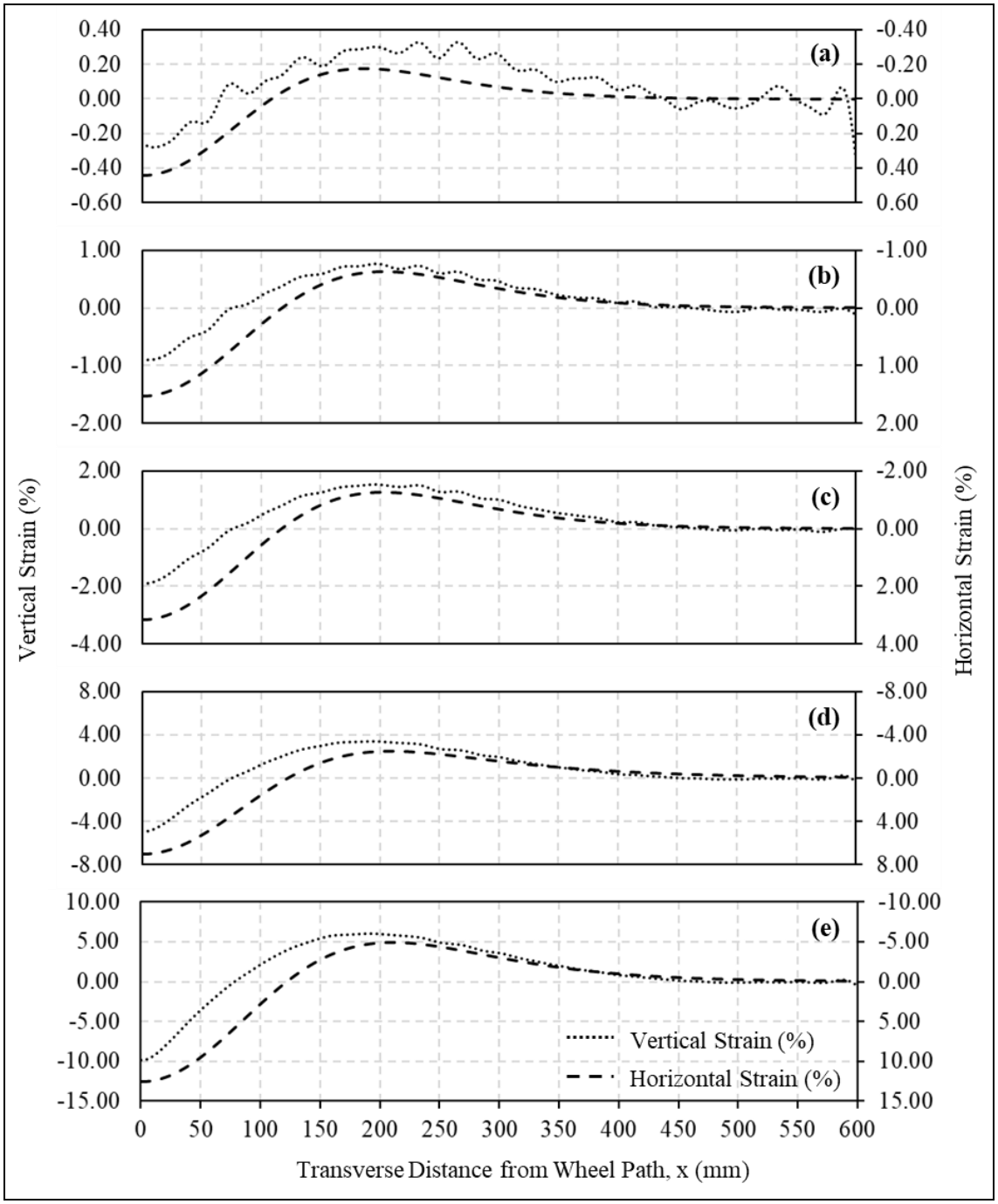

Figure 2.18. Average vertical vs. horizontal strain after: (a) 100; (b) 1,000; (c) 3,000; (d) 10,000; and (e) 20,000 passes

Assuming plane strain conditions, the volumetric strains can be calculated as the sum of the vertical and horizontal normal strains. A positive volumetric strain indicates that the base is dilatant since tension is assumed positive for normal strains. Figure 2.19 shows the volumetric strain within the base along the distance from the wheel path for increasing trafficking cycles. The base is dilatant in the tensile zone under and in the immediate vicinity of the wheel path, with dilation peaking to a maximum value of 6% between 50 mm and 75 mm immediately beyond the contact pressure radius (35 mm) at the end of testing (20,000 passes). A peak dilation of 6% is deemed reasonable given that the base was placed at a comparatively high relative density (85%). The base under the wheel path experienced higher confinement levels from the applied wheel load due to the load distribution from the HMA surface layer. This resulted in a lower critical void ratio and, consequently, in a reduced dilation under the wheel path than at locations adjacent to the wheel path that were not subjected to the same level of confinement. In the compressive zones away from the wheel path, although the confining pressure due to the load distribution of the HMA layer was lower, the horizontal compressive strains were also lower in magnitude, resulting in negligible dilation.

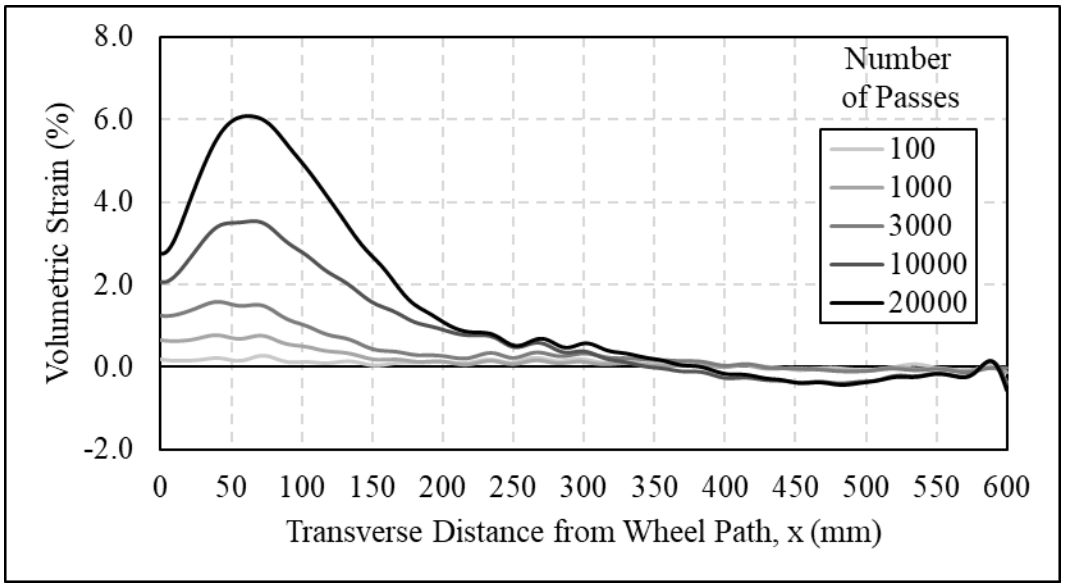

Figure 2.19. Volumetric strain with increasing number of passes.

2.3.3 Vertical Stress Distribution

Earth pressure cells installed within the pavement (Figure 2.3) were used to continuously measure the stress response within the base and subgrade layers under trafficking loads. Figure 2.20 displays the dynamic stress response of the earth pressure cell located at the base-subgrade interface at the center of the wheel path. The x-axis shows the time in number of passes (1 pass = 0.5 seconds) while the y-axis shows the vertical stress as measured by the sensors. The measured stress increased from approximately zero to a maximum value when the wheel load passed over the location of the sensor. The increase in stress under the wheel load for each pass is determined as the vertical stress under trafficking as seen in Figure 2.20. The vertical stress under trafficking at the center of the wheel path for various depths within the pavement with an increasing number of passes is presented in Figure 2.21. The vertical stress remained approximately constant, with a slight increase toward the end of the test. The solid, dotted, and dashed lines represent the average vertical stress at the middle of the base,

base-subgrade interface, and bottom of the subgrade, respectively, for the duration of testing. The earth pressure cell at the depth closest to the surface (middle of the base) registered the highest vertical stress, while the sensor farthest from the surface recorded the lowest vertical stress, capturing the dissipation of vertical stress with increasing depth within the pavement.

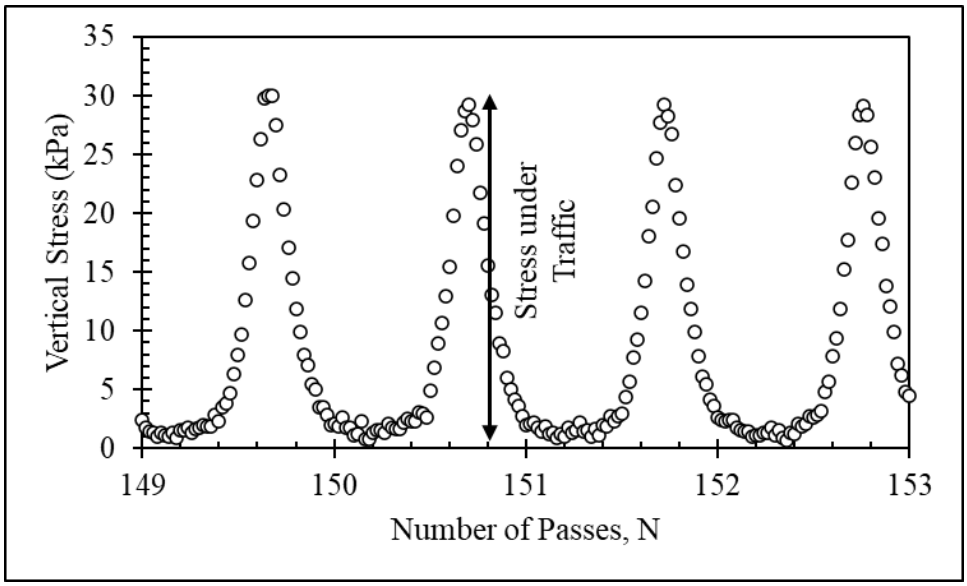

Figure 2.20. Dynamic response of earth pressure cells under traffic.

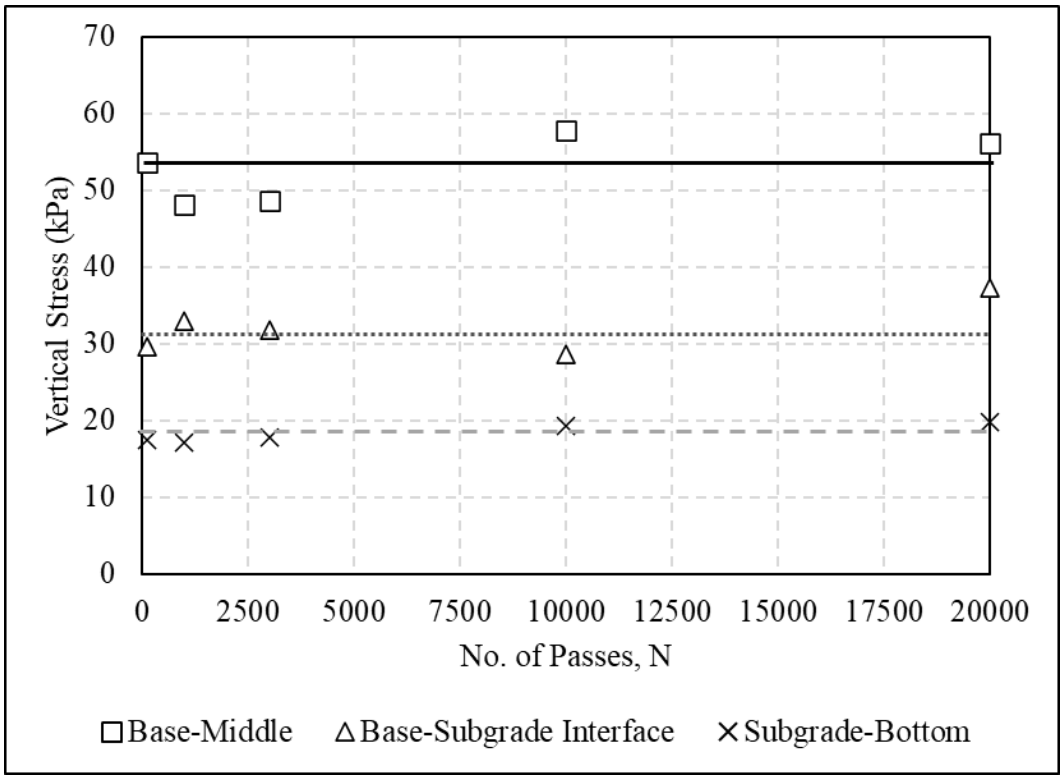

Figure 2.21. Vertical stress at center of wheel path with increasing number of passes.

The vertical stress distribution after 10,000 wheel passes at various depths within the pavement is shown in Figure 2.22. The y-axis shows the vertical stress measured under trafficking at various depths from the surface while the x-axis shows the transverse distance from the sensor locations to the center of the wheel path (at x = 0 mm). While the earth pressure cells were located on either side of the wheel path, a symmetric stress distribution was assumed, showing data points on both sides of the wheel path as measured data. The vertical stress distribution data are fitted with a parameterized form [Equation (2.7)] of Boussinesq's solution (Nwoji et al., 2017) for a vertical stress distribution under a point load.

$$\sigma_{zz} = \frac{3P}{2\pi} \frac{B^3}{\left(\sqrt{x^2 + B^2}\right)^5} \quad (2.7)$$

where P is the applied wheel load (= 2.1 kN)

B is the fitting parameter (mm)

x is the transverse distance from the center of the wheel path (mm)

Fitting using Equation (2.7) implies that the applied load (P) is consistent with the stress distribution. As previously discussed, the vertical stress under the wheel path decreases with increasing depth, . However, this trend reversed away from the wheel path, with vertical stress increasing with depth at distances of 200 mm from the wheel path, i.e., the stress distribution curves widened at locations deeper within the pavement due to the distribution of the load from the wheel over a larger area. The vertical stress distributions within the base (square markers and solid line in Figure 2.22) are clearly compatible with the horizontal normal strain distributions previously discussed in Figure 2.17. The region of horizontal tensile strains ranging from x = 0 mm to 125 mm is roughly the same distance over which the vertical compressive stress went from a maximum of around 60 kPa to less than 5 kPa. While the magnitude of horizontal strains increased with traffic, the compressive and tensile zones in the horizontal normal strain contours remained constant and consistent with the vertical stress distribution, which also remained fairly constant throughout testing.

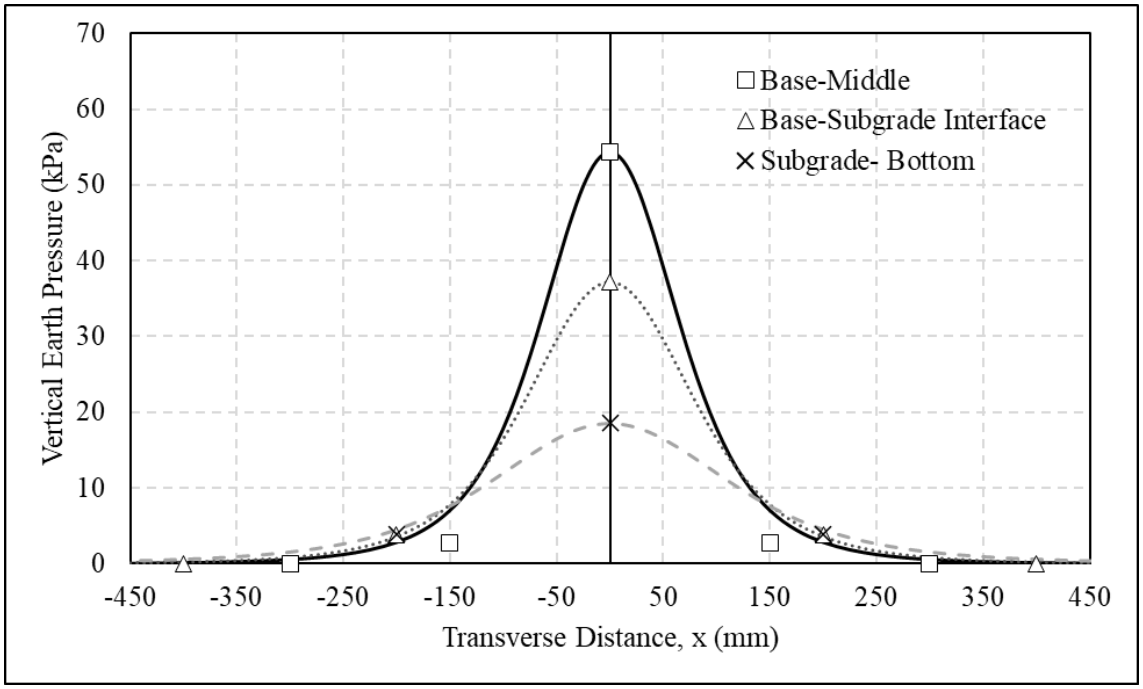

Figure 2.22. Vertical stress distribution under traffic around 10,000 passes.

2.4 CONCLUSIONS

An accelerated pavement testing facility was developed to assess the performance of reduced-scale pavement sections under controlled environmental conditions in a laboratory setting. The facility allowed quantification of the pavement performance through determination of surface deflections, internal particle movements and stress distributions within the pavement structure. To measure surface deformations under repeated rolling wheel loads, an in-house developed profilometer with a 2D laser distance meter was used to capture surface profiles with increasing trafficking cycles. Post-processing techniques involving the filtering of noise from reflections at sharp particle edges and rough pavement surfaces were developed to process the raw surface profile data into rutting profiles. The profilometer facilitated mapping of the pavement surface with a resolution of 1 mm x 1 mm. A unique particle tracking technique was developed to

measure subsurface particle movements due to surface deformations. The particle tracking sensors were made of a flexible system of tell-tale wires that offered the least impedance to the response of the pavement layers to external wheel loads. During trafficking, these sensors continuously measured transverse particle displacements perpendicular to the direction of trafficking. A dense array of 30 trackable particles, at a vertical spacing of 25 mm and transverse spacing of 75 mm, was used to measure particle displacements at various depths within the base. The measured data was combined with expected boundary conditions and fitted with a function that closely captured the physical characteristics of the horizontal displacement data. The vertical stress distribution within the pavement under trafficking was measured using earth pressure cells installed at various depths and various transverse distances from the wheel path. The measured surface deformation profiles, subsurface particle displacements and vertical stress distribution within the pavement structure were in agreement and were useful in understanding the mechanism of surface deformation development and the response of the pavement structure to repeated wheel loading.

- The reduced-scale pavement section subjected to accelerated pavement loading was adequate to the capture development of surface rut through the mechanism of lateral flow of the aggregate base.
- The in-house developed profilometer, post-signal processing, was capable of capturing the rut profiles to the desired accuracy of 0.1 mm.
- The linear progression of the rut with increasing number of wheel passes, and the proportionate increase in heave with the vertical depression under the wheel path indicated that the dominant mechanism of rut development in the test section was lateral flow.

- The array of particle tracking sensors measured the horizontal displacements within the base at close proximity to each other, facilitating the development of the horizontal displacement contours.
- The top-down progression of the displacement contours with increase in trafficking cycle demonstrated the lateral flow of base aggregates. This was confirmed from the shear transfer efficiency contours obtained from the partial derivative of the displacement contours with respect to the 'z'-axis, which showed a reduction in shear transfer efficiency near the HMA-base interface with increasing number of wheel passes.
- The horizontal normal strain contours, obtained as the partial derivative of the displacement field in the transverse direction, showed a region of tensile strain under the wheel path due to vertical deformations, and regions of compressive strain on either side of the region of tensile strains. These regions of tension and compression remained more or less a constant with increasing wheel passes, with only the magnitude of the strains increasing.
- The average of the horizontal normal strains, over the thickness of the base, was found to be compatible with the average vertical strain due to surface deformations. The maximum volumetric dilation of the base was estimated at 6% at the end of testing.
- The dynamic increase in vertical stress measured using the earth pressure cells remained constant with the increasing number of wheel passes.
- For a given depth of installation, the maximum vertical stress occurred under the wheel path and the stress decreased with increasing distance from the wheel path.
- For a given distance from the wheel path, the vertical stress decreased with an increase in depth within the pavement for location in the vicinity of the wheel

path whereas this trend was reversed for sensors located away from the wheel path. Thus, the vertical load from the trafficking wheel was distributed over a wider area at deeper locations within the pavement.

- The stress distribution within the base layer decreased from its maximum under the wheel path to near zero at about 125 mm from the center of the wheel path. This was roughly the same distance over which the horizontal normal strain changed from tension to compression indicating compatibility between the stress and strain distributions.

REFERENCES

Bhattacharjee, S., Mallick, R.B., 2012. Effect of temperature on fatigue performance of hot mix asphalt tested under model mobile load simulator. Int. J. Pavement Eng. 13, 166–180. https://doi.org/10.1080/10298436.2011.653565

Epps, A.L., Ahmed, T., Little, D.C., Hugo, F., 2001. Performance prediction with the MMLS3 at Westrack (Research Report No. FHWA/TX-01/2134-1). Texas Transportation Institute, College Station, TX.

Gehrig, R., Zeyer, K., Bukowiecki, N., Lienemann, P., Poulikakos, L.D., Furger, M., Buchmann, B., 2010. Mobile load simulators – A tool to distinguish between the emissions due to abrasion and resuspension of PM10 from road surfaces. Atmos. Environ. 44, 4937–4943. https://doi.org/10.1016/j.atmosenv.2010.08.020

Guide for Mechanistic–Empirical Design of New and Rehabilitated Pavement Structures. (Final Report No. NCHRP Project 1-37A), 2004. . Transportation Research Board, National Research Council, Washington, D.C.

Kermani, B., Stoffels, S.M., Xiao, M., Qiu, T., 2018. Experimental Simulation and Quantification of Migration of Subgrade Soil into Subbase under Rigid Pavement Using Model Mobile Load Simulator. J. Transp. Eng. Part B Pavements 144, 04018049. https://doi.org/10.1061/JPEODX.0000078

Kim, H., Sokolov, K., Poulikakos, L.D., Partl, M.N., 2009. Fatigue Evaluation of Carbon FRP-Reinforced Porous Asphalt Composite System Using a Model Mobile Load Simulator.

Kim, S.-M., Hugo, F., Roesset, J.M., 1998. Small-Scale Accelerated Pavement Testing. J. Transp. Eng. ASCE 124, 6.

Lee, J., Kim, Y.R., McGraw, E.O., 2006. Performance evaluation of bituminous surface treatment using third-scale model mobile loading simulator. Transp. Res. Rec. 1958, 59–70.

Lee, Jusang, Kim, Y.R., Lee, Jaejun, 2015. Rutting performance evaluation of asphalt mix with different types of geosynthetics using MMLS3. Int. J. Pavement Eng. 16, 894–905. https://doi.org/10.1080/10298436.2014.972916

Lee, S.J., Kim, Y.R., 2004. Development of fatigue cracking test protocol and life prediction methodology using the third scale model mobile loading simulator, in: 5th International RILEM Conference on Cracking in Pavements-Mitigation, Risk Assessment and Prevention. Edited by Petit C., Al-Qadi IL et Millien A. pp. 29–36.

Lee, S.J., Seo, Y., Kim, Y.R., 2006. Validation of material-level performance Models: Using the third-scale Model Mobile loading simulator. Transp. Res. Rec. 1949, 74–82.

Martin, A.E., Walubita, L.F., Hugo, F., Bangera, N.U., 2003. Pavement Response and Rutting for Full-Scale and Scaled APT. J. Transp. Eng. ASCE 129, 11.

Nwoji, C.U., Onah, H.N., Mama, B.O., Ike, C.C., 2017. Solution of Elastic Half Space Problem using Boussinesq Displacement Potential Functions. Asian J. Appl. Sci. 05, 7.

Smit, A. de F., Hugo, F., Epps, A., 1999. Report on the first Jacksboro MMLS tests (Research Report No. FHWA/TX-00/0-1814-2). Center for Transportation Research, Austin, TX.

Smit, A. de F., Hugo, F., Rand, D., Powell, B., 2003. Model Mobile Load Simulator Testing at National Center for Asphalt Technology Test Track. Transp. Res. Rec. 9.

Tang, X., Chehab, G.R., Palomino, A., 2008. Evaluation of geogrids for stabilising weak pavement subgrade. Int. J. Pavement Eng. 9, 413–429. https://doi.org/10.1080/10298430802279827

Tang, X., Stoffels, S., Palomino, A.M., 2014. Mechanistic-Empirical Performance Prediction of Geogrid-Modified Soft Soil Subgrade, in: Geo-Congress 2014 Technical Papers. Presented at the Geo-Congress 2014, American Society of Civil Engineers, Atlanta, Georgia, pp. 3054–3061. https://doi.org/10.1061/9780784413272.297

TxDOT SS3239, 2004. Special Specification for Thin Overlay Mix (TOM).

van de Ven, M., Smit, A. de F., 2000. The Role of the MMLS Devices in APT, in: South African Transport Conference. Presented at the Action in Transport for the New Millennium, p. 16.

Walubita, L.F., 2000. Accelerated testing of an asphalt pavement with the third-scale model mobile load simulator (MMLS3) (PhD Thesis). Stellenbosch: Stellenbosch University.

Walubita, L.F., Hugo, F., Epps, A.L., others, 2000. Performance of rehabilitated lightweight aggregate asphalt concrete pavements under wet and heated model mobile load simulator trafficking: A comparative study with the TxMLS. University of Texas at Austin. Center for Transportation Research.

Zornberg, J.G., Barrows, R.J., Christopher, B., Mitchell, J.K., 1995. CASE HISTORY: CONSTRUCTING A GEOTEXTILE-REINFORCED SLOPE. Geotech. Fabr. Rep. 13.

Chapter 3: Evaluation of Lateral Restraint using Particle Displacements

ABSTRACT

Reduced-scale pavement test sections, with and without a geogrid-stabilized base layers, were constructed and trafficked using the model Mobile Load Simulator (MLS11) to evaluate the mechanism of geogrid stabilization of the unbound aggregate base. The performance of the pavement sections was evaluated by measuring vertical surface deformations (rut), horizontal particle displacements within the base near the geogrid, and vertical stress within the pavement structure. The two control section, identical in their construction and configurations, produced acceptably repeatable performance in terms of surface rutting, and horizontal particle displacements within the base. The inclusion of the geogrid in the stabilized section resulted in the redirection and reduction of lateral flow in the vicinity of the geogrid, thus demonstrating the lateral restraint provided by the stabilizing geogrid. As a consequence of decreased shear transfer across the geogrid resulting in reduced particle displacements below the geogrid, the stabilized section also showed a narrowing of the rut path, with the heaves associated with lateral flow being higher for the same level of vertical deformation under the wheel path.

3.1 INTRODUCTION

Geosynthetics in roadways may provide a number of functions, ranging from mechanical functions such as separation, reinforcement, and stiffening, to hydraulic functions such as lateral drainage, filtration, and moisture barrier (Zornberg, 2017). A relevant application of geosynthetics in flexible pavements is the stabilization of unbound aggregate layers, which can be achieved by different geosynthetics through the stiffening function. This application involves the inclusion of geosynthetics within the unbound aggregate layers (or at the interface between unbound aggregate and subgrade layers) and

aims at improving aggregate layer performance by increasing its resilient modulus and, consequently, its structural capacity.

Several mechanisms have been proposed in the literature (Bender and Barenberg, 1978; Haliburton et al., 1981) to explain how geosynthetics may improve the performance of unbound aggregate layers in flexible pavements. The consensus in the literature is that geosynthetics stabilize unbound aggregates by transferring stresses to the tension-bearing geosynthetic materials, which limits the lateral movement of particles (via lateral restraint) in the vicinity of the geosynthetic. In the case of paved roads, with surface deformations limited by serviceability criteria, other mechanisms such as tensioned-membrane effect are deemed to be negligible (Sun and Han, 2019). Thus, "lateral restraint," which can be mobilized under relatively small deformations, has been recognized as the dominant mechanism of performance improvement for geosynthetic-stabilized paved roads (Christopher et al., 2008; Perkins, 1999; Sun and Han, 2019).

In a geosynthetic-stabilized aggregate layer, "Lateral restraint" may be defined as the mechanism by which the aggregate particles near a geosynthetic are restricted from lateral movements induced by traffic loads. This mitigation of movement, in the in-plane direction of the geosynthetic, is achieved through interlocking and/or friction between the aggregates and geosynthetic. While lateral restraint has been theorized as the governing mechanism leading to stabilization of unbound aggregates under small-strains, and studies such as Sun & Han (2019) have developed a mechanistic-empirical analysis of geogrid-stabilized systems based on lateral restraint, studies experimentally measuring such lateral restraint by direct measurement of particle movements have not been reported in the technical literature.

An important objective of this study is to experimentally demonstrate the development of lateral restraint by measuring and analyzing the lateral displacement of

particles in the aggregate bases of both geosynthetic-stabilized and control pavement sections subjected to rolling wheel loads. A unique assembly of particle tracking sensors was developed (Chapter 2), which is suitable for collection of experimental data needed to generate displacement field data. The horizontal displacements of particles within the aggregate base, vertical surface deformation at the pavement surface and vertical stress within the pavement structure were measured in both stabilized and control pavement sections constructed as part of this study as they were trafficked to failure using the model Mobile Load Simulator (MLS11). The repeatability of accelerated pavement tests is initially evaluated in this study by comparing the horizontal internal particle displacement and vertical surface deformation measurements of two non-stabilized (control) sections. Subsequently, the results from a stabilized section are compared to those from the non-stabilized sections to demonstrate the development of lateral restraints within them. Overall, the methodology developed in this study was able to capture the mechanisms associated with geogrid-stabilization of unbound aggregate base.

3.2 MATERIALS AND METHODS

3.2.1 Pavement Layers

Three reduced-scale pavement sections (Control I, Control II, and Stabilized sections) were constructed as part of this study. All three sections consisted of a 25-mm Hot Mix Asphalt (HMA) ride surface, 125-mm gravel base and 150-mm sand subgrade resting on top of a bed of steel channels (shown in gray in Figure 3.1). The pavement layers were constructed above grade to facilitate access from the sides to the sensors within the pavement section and confined on all sides by a modular frame consisting of two 150-mm tall steel channels stacked on top of each other (shown in orange in Figure 3.1). The pavement sections measured 1800-mm in length and 1200-mm in width, with a

total height of 300-mm. A low strength non-woven geotextile was used for separation between the base and subgrade to prevent intermixing under compaction and trafficking. In the stabilized section, a biaxial geogrid was placed 75-mm below the HMA surface within the base for stabilization.

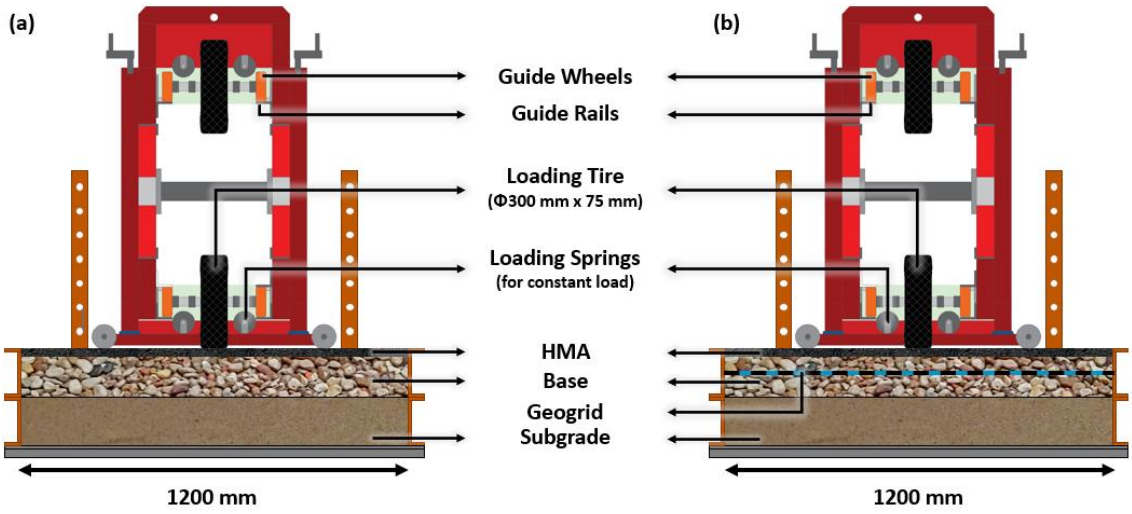

Figure 3.1. Pavement test sections used in this study: (a) Control I & II; and (b) Stabilized.

As the grain size distribution curves in Figure 3.2 show, both the base and subgrade consisted of uniformly graded soil with a Coefficient of Uniformity (CU) ranging from 1.6 to 1.8 and a Coefficient of Curvature (CC) of 1.0. The base aggregate and subgrade sand were classified according to USCS as poorly graded gravel (GP) and sand (SP), respectively. The base aggregate is a river-washed pea gravel with a gradation conforming to AASHTO #8 aggregate size (AASHTO M43-05, 2022) and the subgrade sand is a commercially available Monterey 0/30 sand. Table 3.1 summarizes the properties of the subgrade and base materials used in this study. The subgrade was placed in three 50-mm lifts and compacted to a dry unit weight of 15.4 kN/m^3. The base was

placed in four 25-mm lifts and two 12.5-mm lifts to a total thickness of 125-mm and compacted to a dry unit weight of 17.1 kN/m^3, corresponding to a relative density of 85%. The asphalt mixture used for the surface layer was a thin overlay mix (coarse - class A) conforming to TxDOT Special Specification 3239 (TxDOT SS3239, 2004) with a binder content of 6.5%. The geogrid used for base stabilization in this study was an integrally-formed, polypropylene, biaxial geogrid with aperture dimensions of 38-mm x 38-mm. The geogrid had similar tensile strength and stiffness properties in both the machine and cross-machine directions as specified by the manufacturer. The manufacturer-specified Minimum Average Roll Value (MARV) of the tensile strength at 2% strain was 6.5 kN/m, and the tensile strength at 5% strain was 13 kN/m. The MARV of the ultimate tensile strength of the geogrid was specified as 20 kN/m.

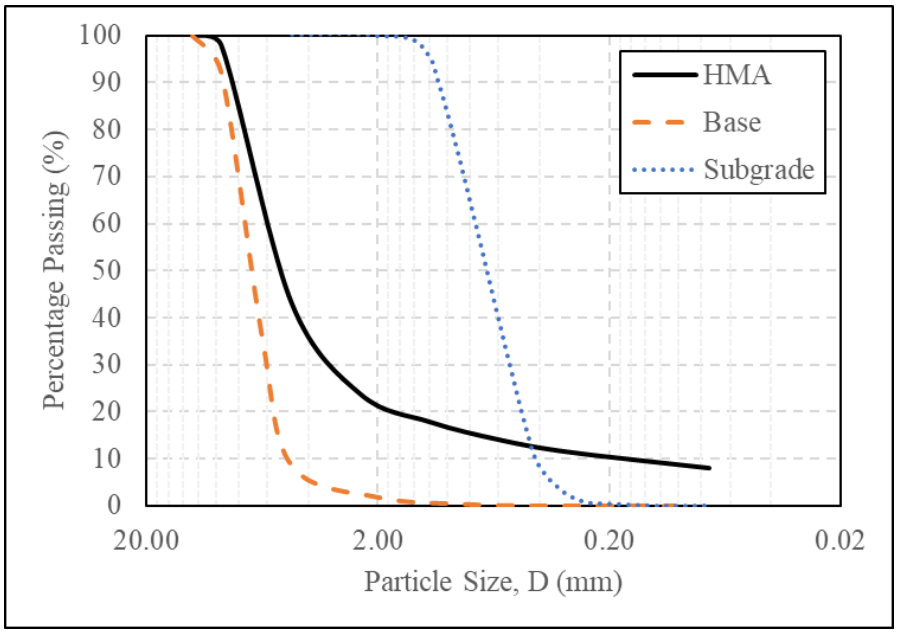

Figure 3.2. Grain size distribution of pavement materials.

3.2.2 Trafficking Equipment

The pavement sections were trafficked with the MLS11 [previously referred to as MMLS in literature (Smit et al., 1999; van de Ven and Smit, 2000)]. The MLS11 is a reduced-scale accelerated wheel loading device that consists of four loading tires connected to a chain of guide wheels. An electric motor drives the system of loading tires and guide wheels along rails in a vertical obround path, resulting in the application of repeated, unidirectional, rolling-wheel loads. The continuous circular motion of the loading tires allows for rapid application of loads up to 7200 passes per hour, facilitating quick turnaround of tests. The rolling wheel loads are applied to the pavement surface by lowering the MLS11 onto the surface using four positioning screws at the ends. A spring and hinge mechanism attached to each loading tire ensures that the applied load remains constant within acceptable levels of surface deformation (up to 12-mm). The specifications of the loading equipment are summarized in Table 3.2. The MLS11 has been predominantly used to evaluate the performance of asphalt concrete mixtures used as surface layers in flexible pavements (Epps et al., 2001; Martin et al., 2003; Smit et al., 2003, 1999). In the laboratory, the MLS11 has been used to determine the performance of bituminous mixtures in terms of their fatigue characteristics (Bhattacharjee and Mallick, 2012; Lee and Kim, 2004), rutting potential (S. J. Lee et al., 2006; Van de Ven et al., 1997), and in the development of newer test methods for evaluation of surface treatment methods (J. Lee et al., 2006). In the context of reinforced pavement layers, several studies such as Baek (2020), Kim et al. (2009), and Raab et al. (2016) have conducted reduced-scale testing of asphalt concrete slabs with the MLS11 and were able to capture the mechanisms associated with the mitigation of fatigue cracks due to reinforcement of the asphalt surface layer with carbon-fiber reinforced plastics and geosynthetics. Lee et al., (2015) demonstrated the development of rut through the mechanism of shear flow in the

HMA surface layer and its reduction due to the reinforcing geosynthetics by conducting reduced-scale tests on control and reinforced asphalt slabs using the MLS11. Limited research is reported on the use of MLS11 and reduced-scale pavement testing to evaluate the mechanisms associated with stabilization of unbound aggregate layers. Tang et al. (2008) utilized the MLS11 in testing reduced-scale pavement sections with geogrids to stabilize weak subgrade soil. The sections were instrumented with an LVDT to measure the subgrade deformations, which was the primary measure of performance in this research. No studies on the geogrid-stabilization of unbound aggregate base in reduced-scale flexible pavements with comprehensive instrumentation was reported in the literature.

	Base	**Subgrade**
Commercial Name	River-washed Gravel (AASHTO #8)	Monterey Sand (0/30)
Average Size, D_{50} (mm)	7.0	0.5
Coefficient of Uniformity, CU	1.6	1.8
Coefficient of Curvature, CC	1.0	1.0
ASTM Classification	GP	SP
Specific Gravity, Gs	2.650	2.655
Dry Unit Weight (γ_d), kN/m^3	17.1	15.4
Relative Density (%)	85	67

Table 3.1. Properties of base and subgrade used in this study.

3.2.3 Instrumentation

The performance of the pavement sections was evaluated by measuring the surface rut, internal particle displacements and vertical stress distribution within the pavement structure. The surface rut generated after a given number of wheel passes was obtained by measuring the profile of the surface with a custom-built profilometer comprising a 2D industrial profiling laser mounted to an electronically controlled actuator. Additional information on the construction, capabilities, and procedure to obtain surface profile measurements are discussed in Chapter 2. The profilometer captures the shape of the pavement surface before and after trafficking, with the change in surface profile due to trafficking determined as the difference between the profiles obtained before trafficking begins and after a given number of passes. Thus, surface profiles were obtained at pre-determined levels of trafficking (after a given number of passes) by stopping the test, removing the MLS11, profiling the surface, and continuing trafficking until the next pre-determined traffic level or the end of testing. The change in surface profile after a given number of passes was used to determine the rut on the pavement surface. The surface profiles were measured along the four different locations (begin, center, end and long) indicated in Figure 3.3. The rut obtained from the three transverse profiles (begin, center and end) were averaged to determine the overall rut for that section at a given number of passes. For the two control sections, pavement surface profiles were measured before the start of testing (0 passes), and after 100, 1000, 10000, and 20000 (end of testing) passes. For the stabilized section, the surface profiles were measured before the start of trafficking (0 passes), and after 100, 1000, 10000, 30000, and 82500 (end of testing) passes. Thus, the overall rut of a section with an increasing number of wheel passes was obtained for the control and stabilized sections. Chapter 2 discusses in

detail the procedures adopted to process the raw surface profile data into pavement rut profiles and rut curves for a pavement section.

Property	**Specification**
No. of Loading Tires	4
Wheel Diameter	300 mm
Tire Width	80 mm
Total Track Width	80 mm
Total Track Length	1100 mm
Load per wheel	2.1 kN
Tire contact pressure	620 kPa
Tire footprint area	34 cm^2
Loading Rate	120 passes per minute
Wheel velocity	2.5 m/s
Lateral wander	Disabled

Table 3.2. Relevant technical specifications of MLS11 used in this study.

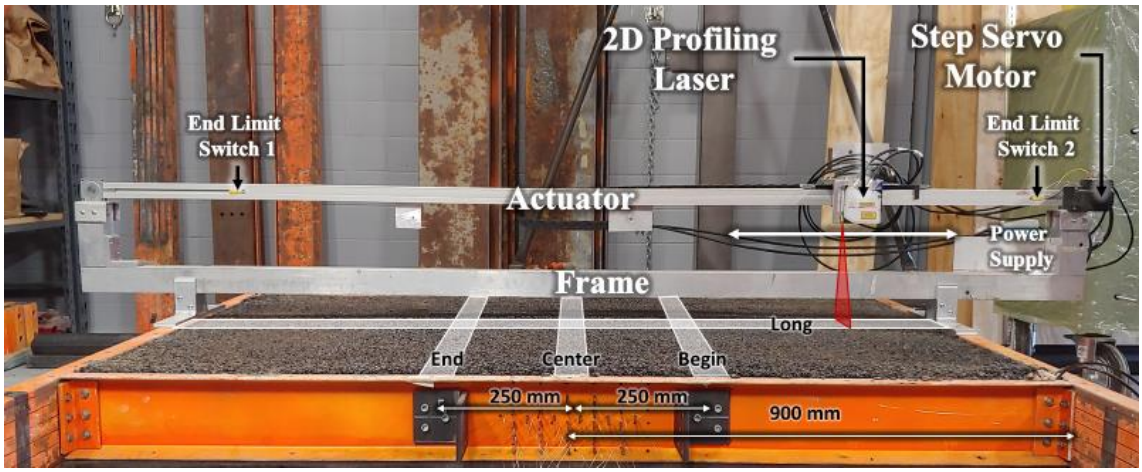

Figure 3.3. Assembled laser profilometer.

Two sizes of earth pressure cells (comparatively larger KDC and smaller KDE) from Tokyo Measuring Instruments Lab (TML) were used to measure the vertical compressive stress within the pavement structure. The larger diameter pressure cells (KDC) were installed at locations within the base due to its larger particle size, while the smaller cells (KDE) were installed within the subgrade at locations below the base and at the bottom of the subgrade. Three pressure cells were installed directly under the center of the wheel path and five pressure cells were installed at various offsets from the center of the wheel path to capture the distribution of stresses from the point of loading within the pavement structure. The two pressure cells within the base and at the top of subgrade are rated for 500 kPa maximum compressive stress, while the other pressure cells are rated for 200 kPa. Figure 3.4 shows the cross-sectional layout of the earth pressure cells within the pavement structure in the control and stabilized sections. As can be seen in the longitudinal cross-section, the pressure cells were installed in a staggered vertical arrangement, i.e., the cells installed at mid-depth within the base were longitudinally separated from those installed at the top of the subgrade, and not on top of each other. This approach was adopted to avoid having a comparatively stiff vertical section of

sensors due to the relatively thick sensor profiles compared to the pavement layer thicknesses. The continuous response of the earth pressure cells under trafficking, measurement of the dynamic stress developed within the pavement structure due to the rolling wheel load from the continuous response, and development of stress distribution plots from spot-measurements of the dynamic stress within the pavement are discussed in Chapter 2.

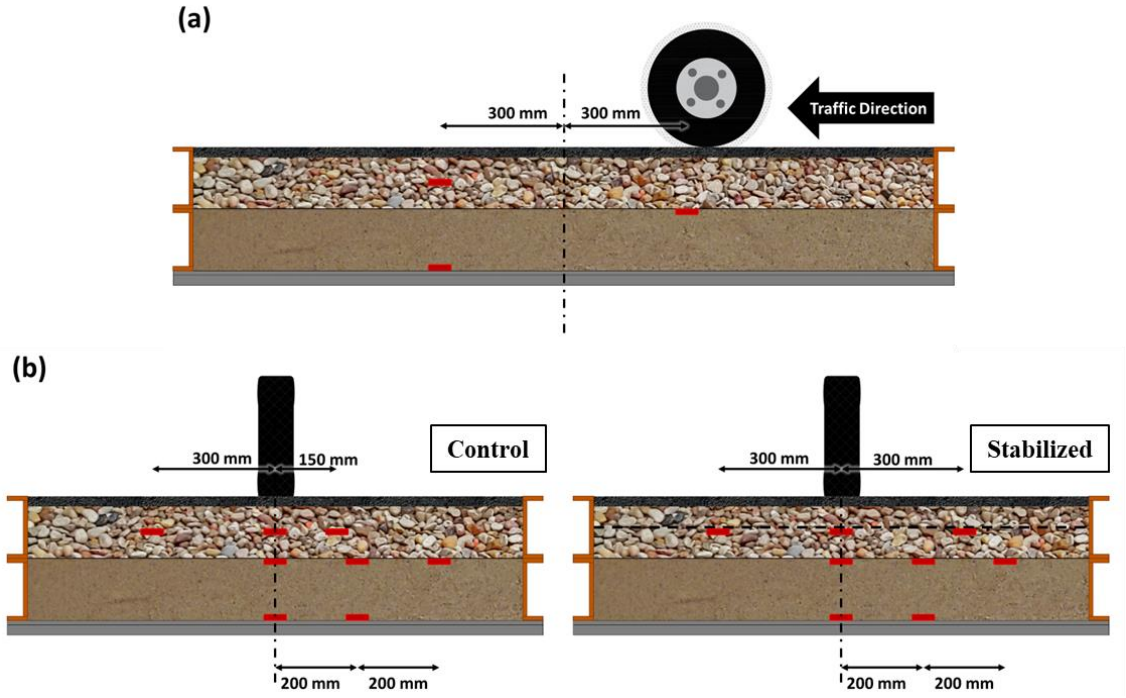

Figure 3.4. Pressure cell layout in: (a) longitudinal cross-section; and (b) transverse cross-section of control and stabilized sections.

A unique particle tracking sensor was used to measure the lateral movement of the aggregate particles within the base of the control and stabilized pavement sections. This sensor consisted of a linear displacement sensor affixed to the side of the pavement structure and connected horizontally via a tell-tale wire to a particle within the gravel

matrix of the base. The tell-tale wires transfer the movements of the attached particles within the base to the externally-affixed displacement sensors. Thus, any relative movement between the aggregate particle and displacement sensor is recorded. Because the displacement sensors are securely mounted to the frame of the pavement structure, the measured displacements can be considered the absolute movement of the particles within the base. To prevent damage to the tell-tale wires from adjacent gravel particles, which could impede the accurate transfer of movements from the attached particle to the sensor, the wires were sheathed in a well-lubricated housing sleeve. A detailed description of the development of the sensor, and its working principles and limitations are discussed in Chapter 2. Figure 3.5 displays the layout of the trackable particles installed within the base of the control and stabilized sections. Particle movements were measured at five different depths at a 25-mm vertical spacing within the base. At each depth, particles at five different offsets from the wheel path (75-mm, 150-mm, 225-mm, 300-mm, and 450-mm) were monitored for lateral movement toward or away from the wheel path. These sensors were aimed at measuring the development of restraint by the geogrid against internal particle movements. The continuous measurement of particle displacement under traffic loading, development of the horizontal displacement function as a function of the lateral distance from the wheel path, interpolation of the fitting parameters of the displacement function with depth, and method of generating the displacement fields, strain fields, vertical gradient fields, and average volumetric dilations from these measurements are discussed in detail in Chapter 2.

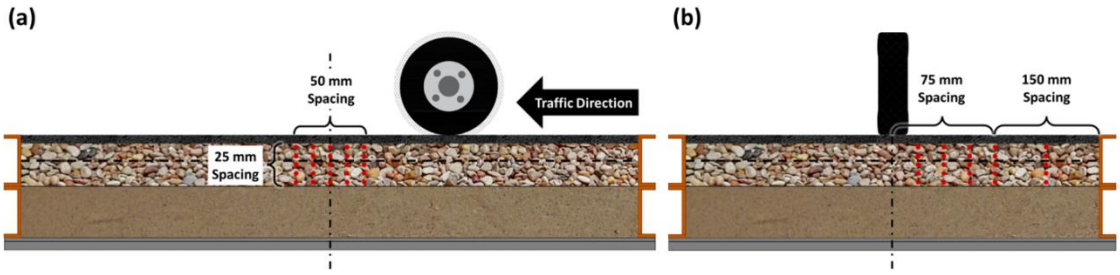

Figure 3.5. Trackable artificial particle layout: (a) Longitudinal cross-section; and (b) Transverse cross-section.

3.3 RESULTS AND DISCUSSION

The measured response of the two control sections and stabilized section subjected to rolling wheel loads (with no lateral wander) of the MLS11is discussed in this section. While the lateral movement of particles within the base and vertical stress within the pavement structure were measured continuously as the test sections were trafficked to failure, the surface deformation reached after a specific number of rolling wheel load passes was determined intermittently. Specifically, trafficking was interrupted after a pre-determined number of passes, namely after 100, 1000, 3000, 10000 and 30000 passes. This approach facilitated use of the profilometer to measure the surface profiles, which could not be done with the MLS11 on top of the pavement section. The initial and final surface profiles were also measured before and after the end of testing.

3.3.1 Geogrid-induced Reduction in Surface Deformation

The rut measured with increasing number of wheel passes in the two control (C-1 and C-2) sections and the stabilized (S) section is presented in Figure 3.6. The x-axis shows the number of load repetitions in thousands of wheel passes, and the y-axis shows the total rut, r, measured as the sum of the depth of deformation, d, along the wheel path, and the vertical heave, h, adjacent to the wheel path, as discussed in Chapter 2. The two

control sections, indicated by dashed lines and square (C-1) and triangular (C-2) markers, demonstrate the repeatability of the accelerated pavement tests performed as part of the study. For the two control sections, the surface profiles and, therefore, the rut depths (r) were measured after 100, 1000, 3000 and 10000 passes, in addition to the surface profile measurements before (0 passes) and after the end of trafficking (20000 passes for C-1 and 20800 passes for C-2). For the stabilized section, the surface profiles were measured after 100, 1000, 3000, 10000 and 30000 passes, in addition to measurements before (0 passes) and after the end of trafficking (82,440 passes). The two control sections were found to perform within 10% of each other in terms of surface rut after a given number of wheel passes, while the stabilized section performed significantly better than the control sections with the number of wheel passes to the end-of-test being four times those in the control sections. The 10% variability between the two control section repeats (C-1 and C-2) was considered acceptable for the purposes of this study.

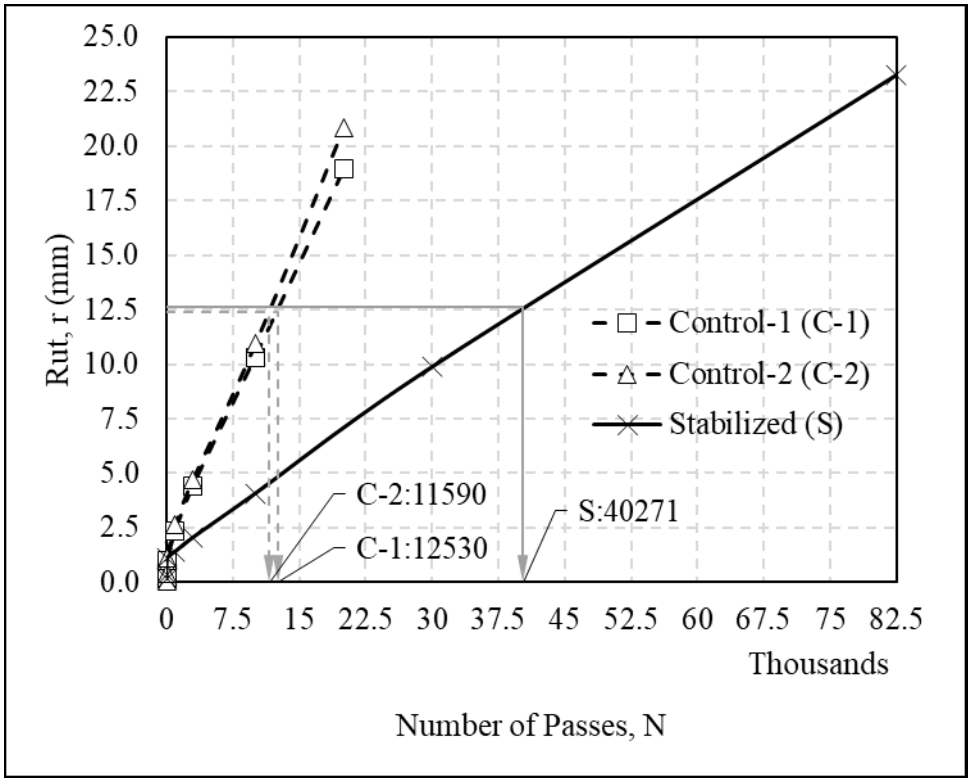

Figure 3.6. Rut, r, vs. number of passes, N, in control (C-1 and C-2) and stabilized (S) sections.

Although the surface profiles, and hence rut measurements, were obtained at discrete intervals of wheel passes during testing, the rut curve (as a function of number of wheel passes) can be used to estimate the rut on the pavement surface at any given number of wheel passes, N, through interpolation. Thus, given a failure rut depth, r, the number of passes to failure, N_r, for any pavement section can be readily obtained using the rut curves. As an example, the number of passes to failure, N_r, at a failure rut depth (r = 12.5 mm), for the two control sections and stabilized section were determined as shown in Figure 3.6. The two control sections reached a rut of 12.5-mm after about 12000 passes, while the stabilized section was subjected to over 40000 passes before reaching the same rut. This corresponds to a 330% improvement in performance in the stabilized

section compared to the variability of 10% amongst the control sections. Since the control and stabilized sections were essentially identical in all aspects except the stabilizing geogrid, the improved performance of the stabilized section is a direct result of the stabilization provided by the geogrid.

To quantify this improvement in pavement performance due to the stabilizing geogrid, the concept of Traffic Benefit Ratio (TBR) is utilized herein. AASHTO R50 (2009) defines the TBR as the ratio of the number of load cycles (wheel passes) in a stabilized pavement structure to reach a defined failure state to the number of load cycles for a control section to reach the same defined failure state. By definition, TBR is the function of the defined failure state, i.e., failure rut in this study, and thus for different failure rut values, the TBR can be determined as a function of the pavement rut, r. Figure 3.7 shows the TBR of the stabilized section compared against the two control sections (S/C-1 and S/C-2 – solid lines) for various levels of failure rut, r_f. It also shows the control sections compared against each other (C-1/C-2 and C-2/C-1 – dashed lines) to demonstrate the repeatability of the TBR curves. The traffic ratio determined amongst the control sections remained very close to the ideal value of 1.0 (perfect repeats), with the largest deviation occurring at the lowest failure rut measurement of 2.5-mm, where the likelihood of rut measurement errors is highest. The TBR of the stabilized section compared with the two control sections (C-1 and C-2) rises sharply to a maximum value of 4 and 5 at 3-mm rut and then decreased with increasing rut depth to a constant asymptotic value of 3.2 and 3.5, respectively. Thus, the stabilized section performed roughly 3.3 times better than the control sections.

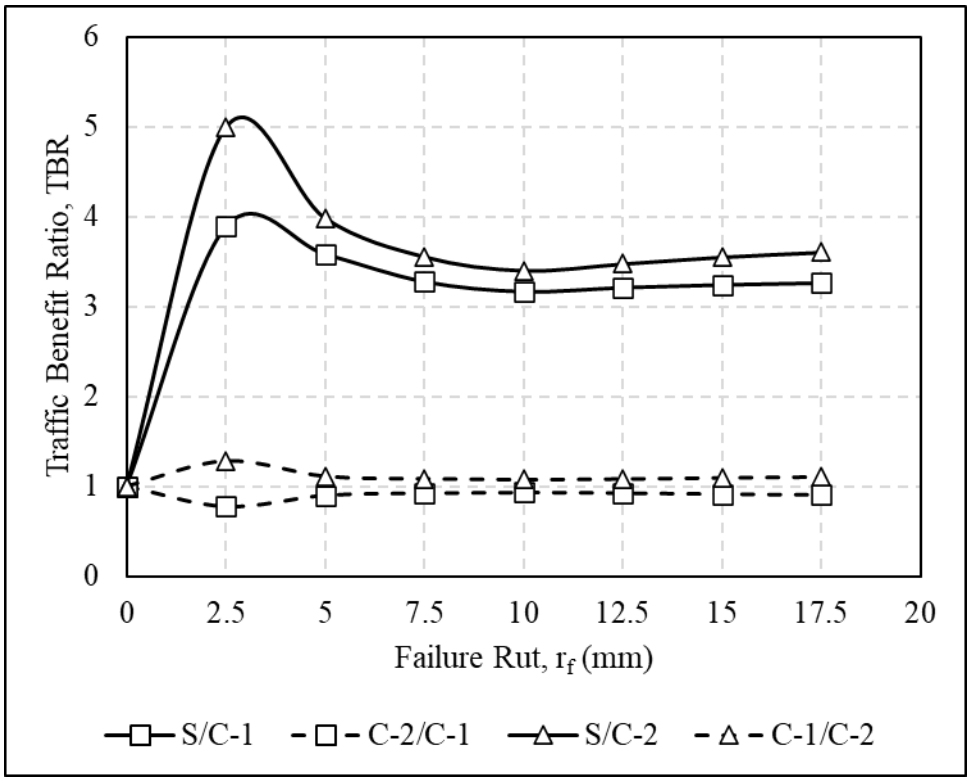

Figure 3.7. Traffic Benefit Ratio (TBR) as a function of failure rut, r_f.

Figure 3.8 compares the shapes of the surface profiles as measured from the control and stabilized sections for the same vertical deformation depths, *d*. The x-axis shows the horizontal distance from the center of the wheel path and the y-axis shows the vertical deformation of the surface as measured by the profilometer. The surface profiles obtained from the control sections (C-1: blue and C-2:orange) at 1000 (dotted), 3000 (dashed) and 10000 (solid) passes were compared with those obtained from the stabilized section (S: gray) at 3000 (dotted), 10000 (dashed) and 30000 (solid) passes, so that the vertical deformation depth, d, under the wheel path at x = 0 mm was the same for the control and stabilized section profiles being compared. For a given pavement section (control or stabilized), the surface profiles obtained after three different numbers of passes (dotted, dashed, and solid lines of the same color) were found to intersect

approximately at a single point, indicated by a solid circle of the same color, which corresponds to approximately to a negligible value of deformation value (i.e., w ≅ 0 mm at these points). These are the points around which the HMA surface essentially rotated with an increasing number of wheel passes. Also, the existence of the points of rotation is consistent with the development of rut through lateral flow of base materials, resulting in heave on both sides of the wheel path (MEPDG 2004). The location of this point of rotation determines the width of the rut along the wheel path. The point of rotation (R) was located comparatively closer to the center of the wheel path in the stabilized section (at x_r = 64 mm) than in the control sections (at x_r = 83.5 mm for both C-1 and C-2), implying a narrower rut path in the stabilized section compared to the control sections. The inclusion of geogrid in the path of the radial flow of base aggregates redirected the flow resulting in a narrowed rut path. Instead of a radially outward particle flow from the point of application of the wheel load, the particles tended to move more laterally outward (horizontally parallel to the plane of the geogrid). With the geogrid laterally restraining the in-plane particle movement closer to it, the particles tend to move away from the geogrid (vertically) at locations away from the wheel path. Additionally, for the same vertical deformation depth (d) under the wheel path, the maximum heave (h) was comparatively higher and occurred closer to the wheel path in the stabilized section, whereas the maximum heave was comparatively smaller and occurred farther away from the wheel path in the control section.

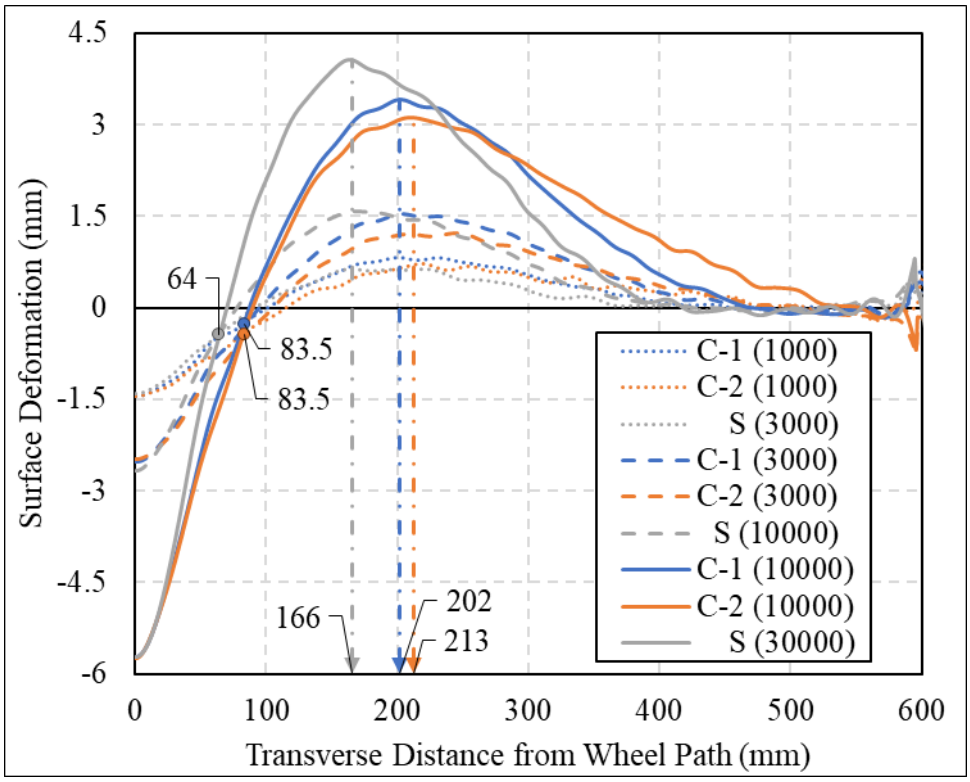

Figure 3.8. Comparison of surface profiles of control (C-1 and C-2) and stabilized (S) pavement sections.

The estimated heave (h) as a percentage of the total rut (r) for various levels of rutting (in both the control and stabilized sections) is shown in Figure 3.9. As can be observed in Figure 3.8 and Figure 3.9, the stabilized section exhibited a larger normalized heave compared to the control sections at all levels of rut (r). The magnitude of the normalized heave was found to increase with increasing rut dept, indicating that lateral flow became the dominant rut development mechanism at higher rut levels. The development of tension in the stabilizing geogrid causes an increase in the horizontal compressive stresses within the aggregate adjacent to the wheel path. Thus, for similar levels of tensile strains (under similar vertical deformations) under the wheel path, the soil adjacent to the wheel path would be subjected to higher horizontal compressive

stresses in the stabilized section than in the control sections. Since the vertical compressive stress due to the wheel load is similar in both the control and stabilized sections, the soil adjacent to the wheel path would be subjected to higher horizontal compressive stresses (in the stabilized section) and would undergo larger horizontal compressive strains. This produces larger vertical tensile strains adjacent to the wheel path, resulting in comparatively larger heave next to the wheel path in the stabilized section compared to the control sections.

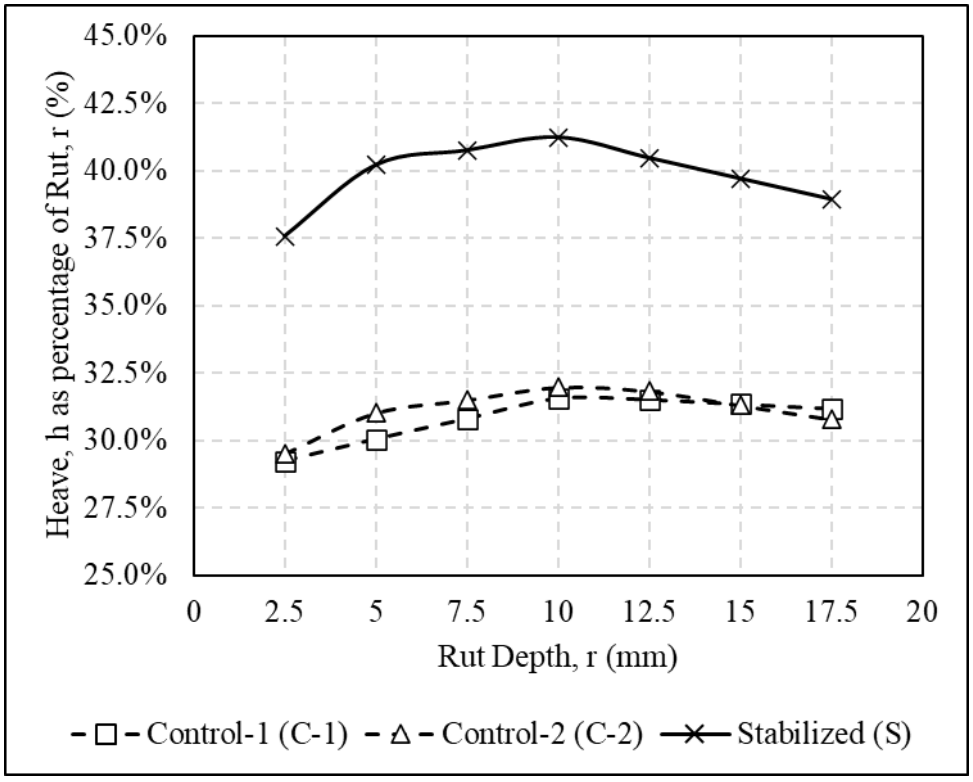

Figure 3.9. Normalized heave, h/r (%) for control and stabilized sections with increasing rut.

3.3.2 Development of Lateral Restraint

As detailed in Chapter 2, the lateral displacements measured by the particle tracking sensors installed at the same depth within the base were fit with a displacement function, and the fitting parameters were interpolated with depth to evaluate the lateral displacements at any transverse distance from the wheel path and for any depth within the base. The horizontal displacement field and the horizontal normal strain field within the base layer were developed from the lateral displacements evaluated for the two control sections and the stabilized section. To assess the repeatability of the particle displacement measurements, the displacement fields obtained from the two control sections are compared in Figure 3.10. For illustrative purposes, comparisons were made at three different stages of trafficking, namely after 3,000, 10,000 and 20,000 passes, to represent the pavement behavior at early, mid, and late stages in the life of the pavement sections. The x-axis of the contour plots shows the distance from the wheel path in the transverse direction, with 0-mm at the center of the wheel path and 600-mm at the edge of the pavement. The y-axis shows the depth from the surface of the completed pavement section, with the HMA-base layer interface at 25-mm and base-subgrade interface at 150-mm. The contours represent horizontal displacements, with the darker regions showing higher displacements. The displacement contours progressed from near the HMA-base interface to the bottom of the base layer with increasing surface rut due to trafficking. As expected, the contours show that displacement magnitude increased with an increasing number of passes, with the maximum lateral displacement within the base occurring towards the top of the base about 150-mm from the center of the wheel path. The lateral displacements were found to decrease with depth within the base layer, with the location of the peak displacement (at a given depth) approaching the wheel path with increasing depth. The contours representing the displacement fields obtained from the two control

sections are very similar, both in terms of their shape as well as the actual magnitude of the displacement contours. The section control-2 exhibited slightly higher displacements compared to control-1, which was consistent with the fact that control-2 also showed slightly higher levels of rut for the same number of passes (Figure 3.6) compared to control-1. Since the difference in the pavement surface rut and displacement contours at any given number of passes between the two control sections is particularly smaller (an order of magnitude) than the corresponding difference between the stabilized and control sections, the experiment is deemed to have an acceptable level of repeatability for the purposes of this study.

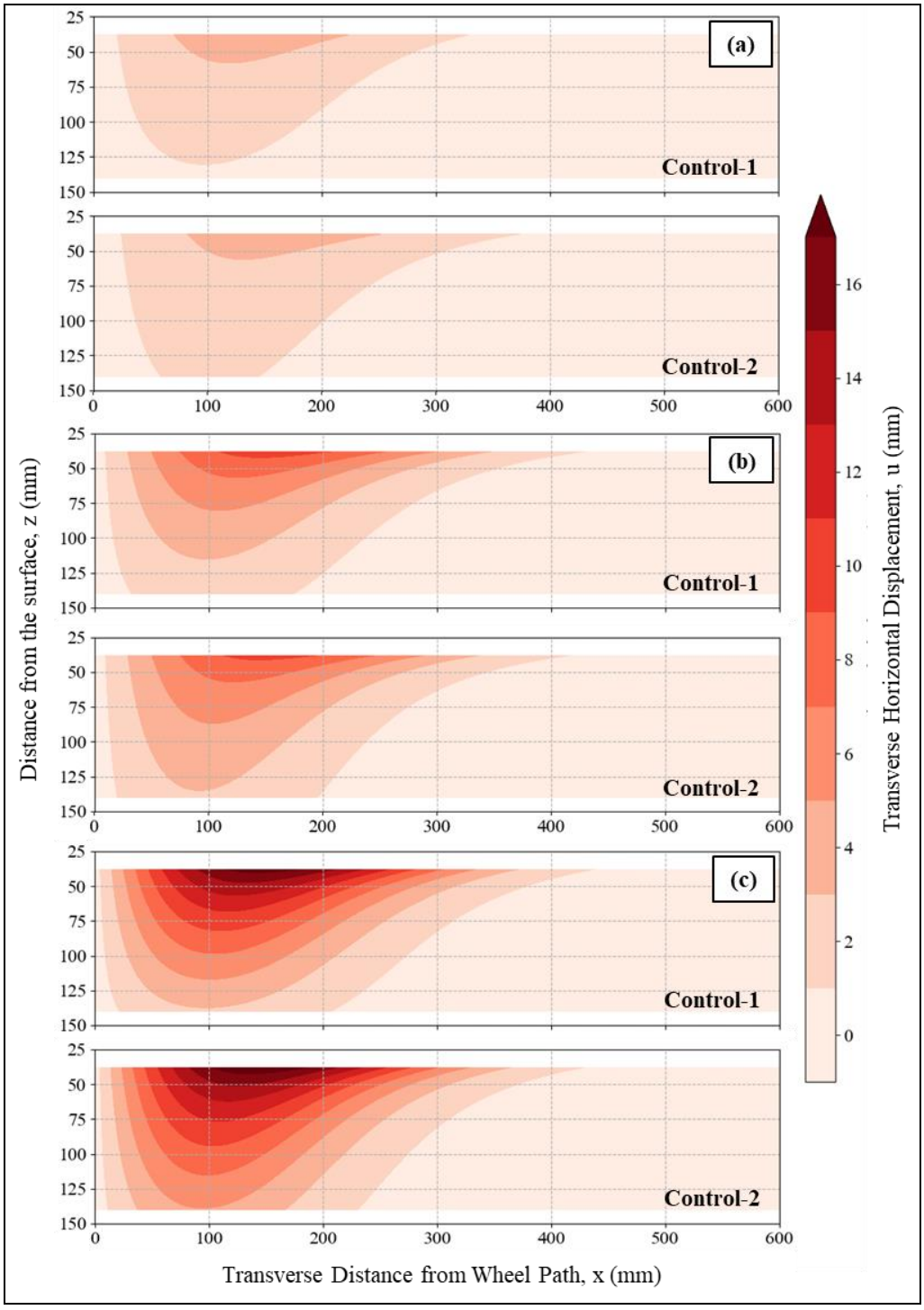

Figure 3.10. Displacement fields after: (a) 3000; (b) 10000; and (c) 20000 passes in Control (C-1 and C-2) sections.

Since the similarity in behavior of both control sections has been established, only section control-1 will be used for comparison with the stabilized section. To compare the displacement fields of the control and stabilized sections, two different approaches were adopted. The first approach involves comparing the displacement contours in the control and stabilized sections at similar number of passes, i.e., a load-based approach. Figure 3.11 compares the displacement contours observed in the control and stabilized sections after 3000, 10000 and 20000 passes. The depth of geogrid installation within the base is indicated by the dashed horizontal line (at z = 75 mm) in the displacement contours of the stabilized section. In the control section, the initial displacements under the wheel path were essentially vertical (i.e., near-zero horizontal displacement component under the wheel path) and flowed radially outward, peaking to a maximum horizontal displacement next to the wheel path. In the stabilized section, the inclusion of the geogrid within the path of this radial flow impedes the movement of particles, resulting in the reduction in magnitude and redirection of the orientation of the lateral flow. The displacement contours appear vertically compressed and stretched out near the top of the base layer in the stabilized section compared to the control section. In the region closer to the surface (above the elevation of the geogrid), the particle displacements were distributed over a larger region than in the control section due to the redirection of lateral flow, from a radial to a more horizontal direction away from the wheel path. Lateral displacements in the immediate vicinity of the geogrid (both above and below it) were significantly reduced. Such reduction can be attributed to the aggregate particles being restrained by their interaction with the geogrid through interlocking and friction. Horizontal particle movements were also significantly reduced at all locations below the geogrid. Because of the presence of the geogrid, the lateral flow of particles due to traffic above the geogrid

was not effectively transferred to the particles interlocked in the geogrid, which reduced the transfer of shear to the particles below the geogrid. Thus, the inclusion of a geogrid within an unbound aggregate layer in a flexible pavement results in: (1) redirection of lateral flow above the geogrid over a wider distance from the wheel path; (2) lateral restraint of the unbound aggregates in the immediate vicinity of the geogrid; and (3) reduced transfer of shear to the aggregate layer below the geogrid.

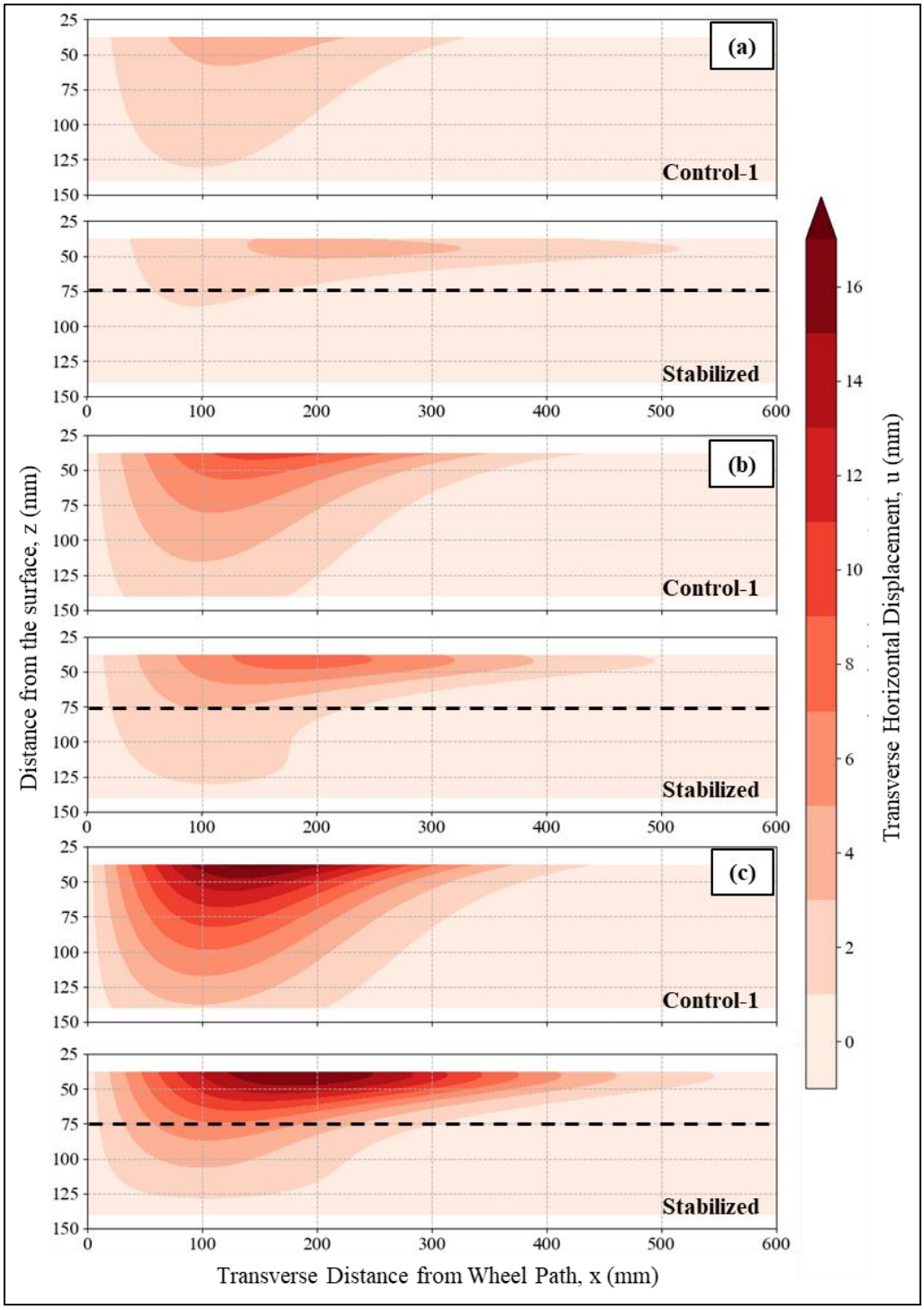

Figure 3.11. Displacement fields after: (a) 3000; (b) 10000; and (c) 20000 passes in Control (C-1) and stabilized (S) sections.

The second approach used to assess the displacements within the control and stabilized sections involved comparing the displacement contours at similar levels of vertical deformation depths (d) along the wheel path, i.e., a displacement-based approach. Figure 3.12 compares the lateral displacement contours of the particles in the base at vertical deformations under the wheel path of 1.5-mm, 2.6-mm, and 5.7-mm. The effects of lateral flow redirection and reduced shear transfer across the geogrid are observable in the contours of the stabilized section. However, for the same level of vertical deformation under the wheel path, the displacements observed above the geogrid location were comparatively higher in the stabilized than in the control section, while the displacements at locations below the geogrid were lower. Since the radial flow of the aggregates in the base was impeded by the geogrid, the particles above the geogrid were displaced farther to accommodate the same level of vertical deformation with reduced particle flow below the geogrid, resulting in increased lateral deformations above the geogrid. Also, increased lateral particle displacements were observed closer to the wheel path (x = 0 mm) in the stabilized section compared to the control section, indicating the redirection of mostly vertical movement under the wheel path in the control section to lateral movement in the stabilized section parallel to the geogrid plane. This increased lateral displacement between the surface HMA layer and geogrid resulted in the larger heave observed in the stabilized section for the same vertical deformation under the wheel path (Figure 3.8) compared to the control section. Thus, the geogrid improved the rutting performance of the unbound aggregate layer by redirecting the radial flow path to become more horizontal, and then reducing the redirected lateral flow of aggregates by providing restraint against lateral movement through aggregate interlocking and friction.

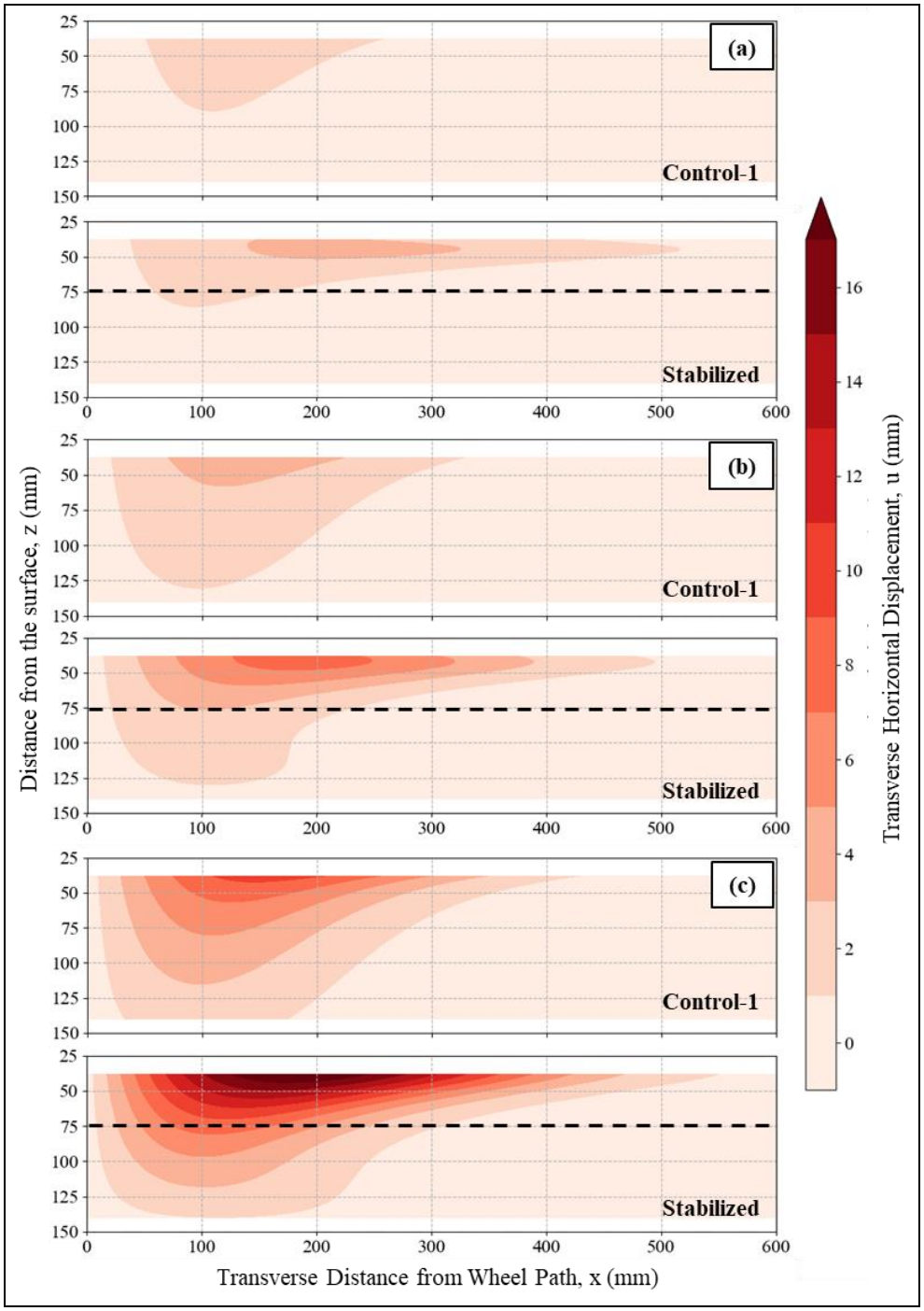

Figure 3.12. Displacement fields at vertical deformation depths, d, under wheel path of: (a) 1.5-mm; (b) 2.6-mm; and (c) 5.7-mm in control (C-1) and stabilized (S) sections.

Figure 3.13 shows the vertical gradient of the horizontal displacement field in the control and stabilized sections. The vertical gradient, which is one component of shear strain in the material, is helpful to quantify the effectiveness of shear transfer from one aggregate to another immediately below it since as it measures the change in lateral displacement with increasing depth. A smaller gradient (lighter contour) implies low relative displacement between adjacent aggregates along the depth, indicating an effective transfer of shear, while a larger gradient (darker contour) represents a comparatively larger slip between adjacent aggregates along the depth. At comparatively low traffic levels (e.g., N = 3000 passes), when cumulative plastic deformations are low, the light contour lines show a very high shear transfer efficiency. With increasing number of cycles, the shear transfer efficiency was found to decrease in the regions of large lateral flow. Thus, in the stabilized section, the shear transfer efficiency was lower than in the control section in the regions above the geogrid characterized by larger lateral flow (due to redirection), while the efficiency was higher than in the control section below the geogrid location.

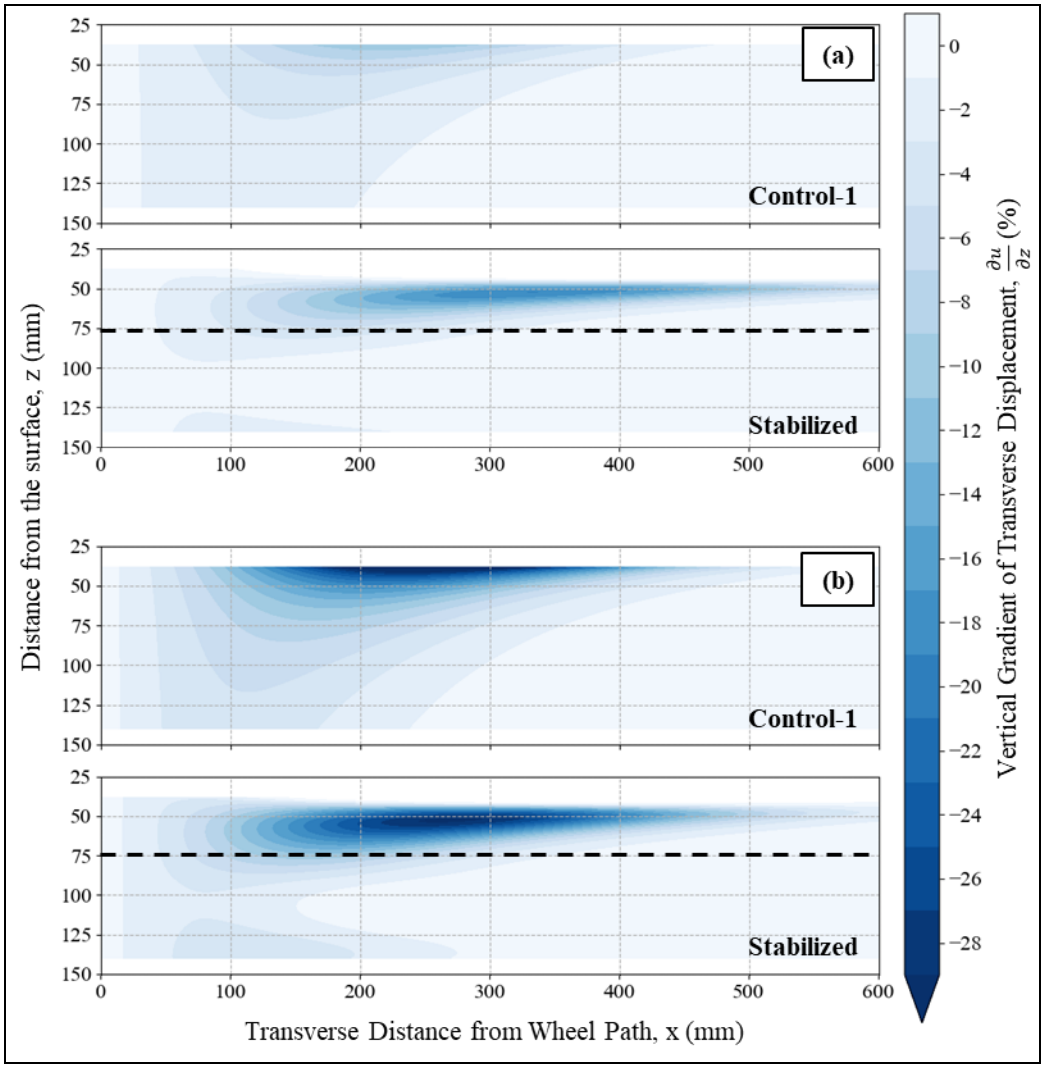

Figure 3.13. Gradient of lateral displacement field after: (a) 3000; and (b) 10000 passes in control (C-1) and stabilized (S) sections.

The horizontal normal strain distribution within the base layer was defined from the partial derivative of the horizontal displacement field with respect to the transverse distance from the wheel path, *x*. Figure 3.14 compares the horizontal normal strain (ε_x) contours in the base of the control and stabilized sections obtained from the partial derivative of the displacement contours after 3000, 10000 and 20000 passes. The region where strains are tensile is shown in red contours and compressive strains are represented

by blue contours. Regions with comparatively large strains are shown using a darker shade of red or blue, with the white contour representing a region of negligible strain. In both the control and stabilized sections, the region under the wheel path (x = 0 mm) showed the maximum tensile strain, which decreased with depth. Adjacent to the tensile region under the wheel path is a region of negligible strain (white contour), which marks the location of maximum horizontal displacement and the transition from a tensile region under the wheel path to a compressive region farther from the wheel path. Although the magnitudes of tensile and compressive strains increased with increasing number of passes, the regions of tension and compression, and that of negligible strain, remained reasonably constant with increasing traffic in both the stabilized and control sections. The normal strains induced within the geogrid-stabilized base were lower than those induced in the control section for the same number of passes due to the lateral restraint effect. The stabilization of the base by the geogrid also reduced the depth to which the normal strains were induced due to the external wheel load. Finally, due to the redirection of lateral flow by the geogrid and the reduced shear transfer across the geogrid in the stabilized section, the strains induced (both compressive and tensile) were distributed over a wider area in the region above the geogrid and over a narrower area in the region below the geogrid.

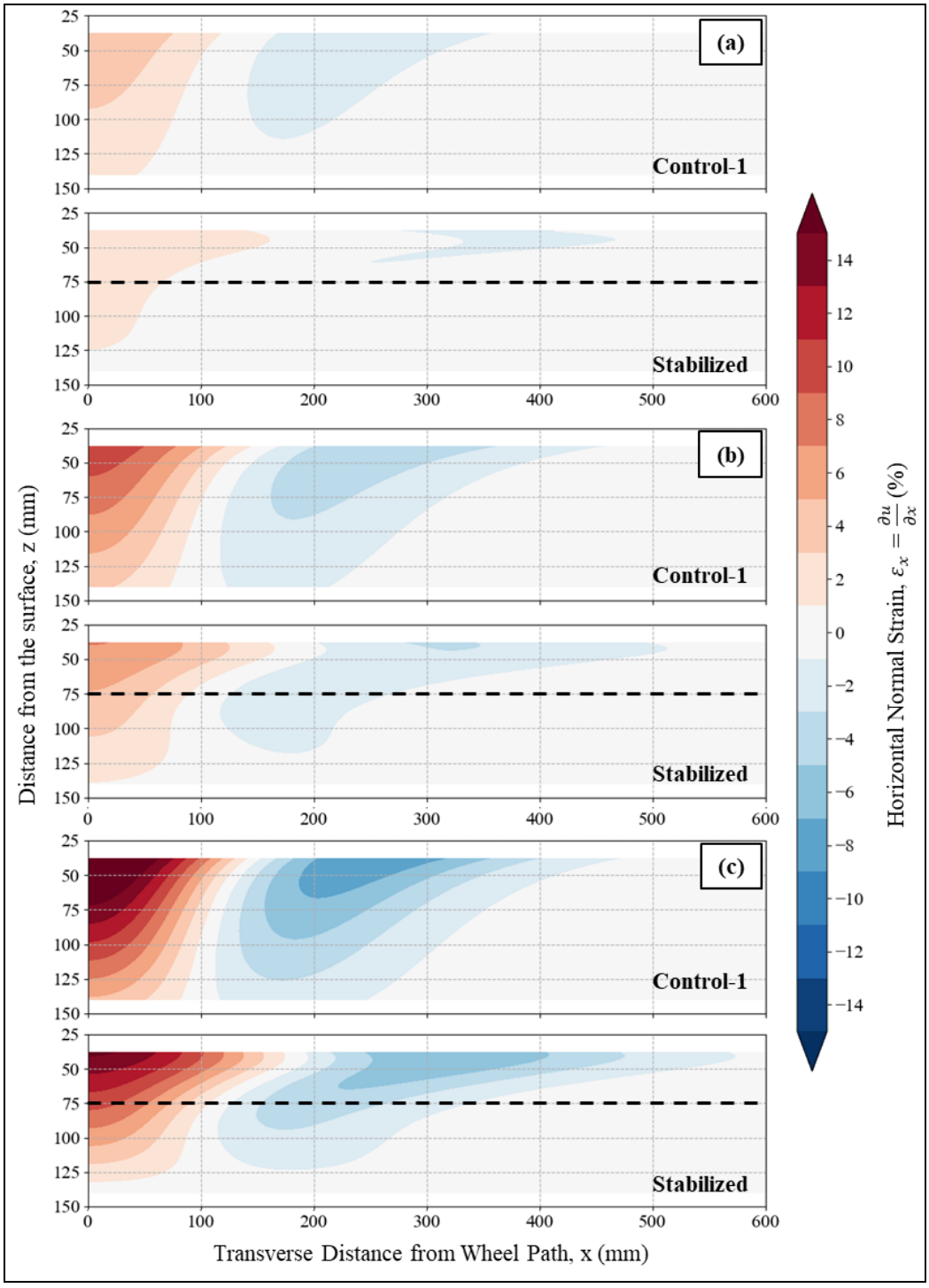

Figure 3.14. Normal strain fields after: (a) 3000; (b) 10000; and (c) 20000 passes in control (C-1) and stabilized (S) sections.

Figure 3.15 compares the horizontal normal strain contours for the control and stabilized sections at the same level of vertical deformation depth (d) along the center of the wheel path (x = 0 mm). Since the vertical deformations were the same and geogrid stabilization reduced the depth of influence of the external load, the vertical deformations were compensated by an increase in tensile strains under the wheel path in the stabilized section. This in turn resulted in an increase in compressive strains adjacent to the wheel path, which led to increased heave in the stabilized section for the same vertical deformation along the wheel path.

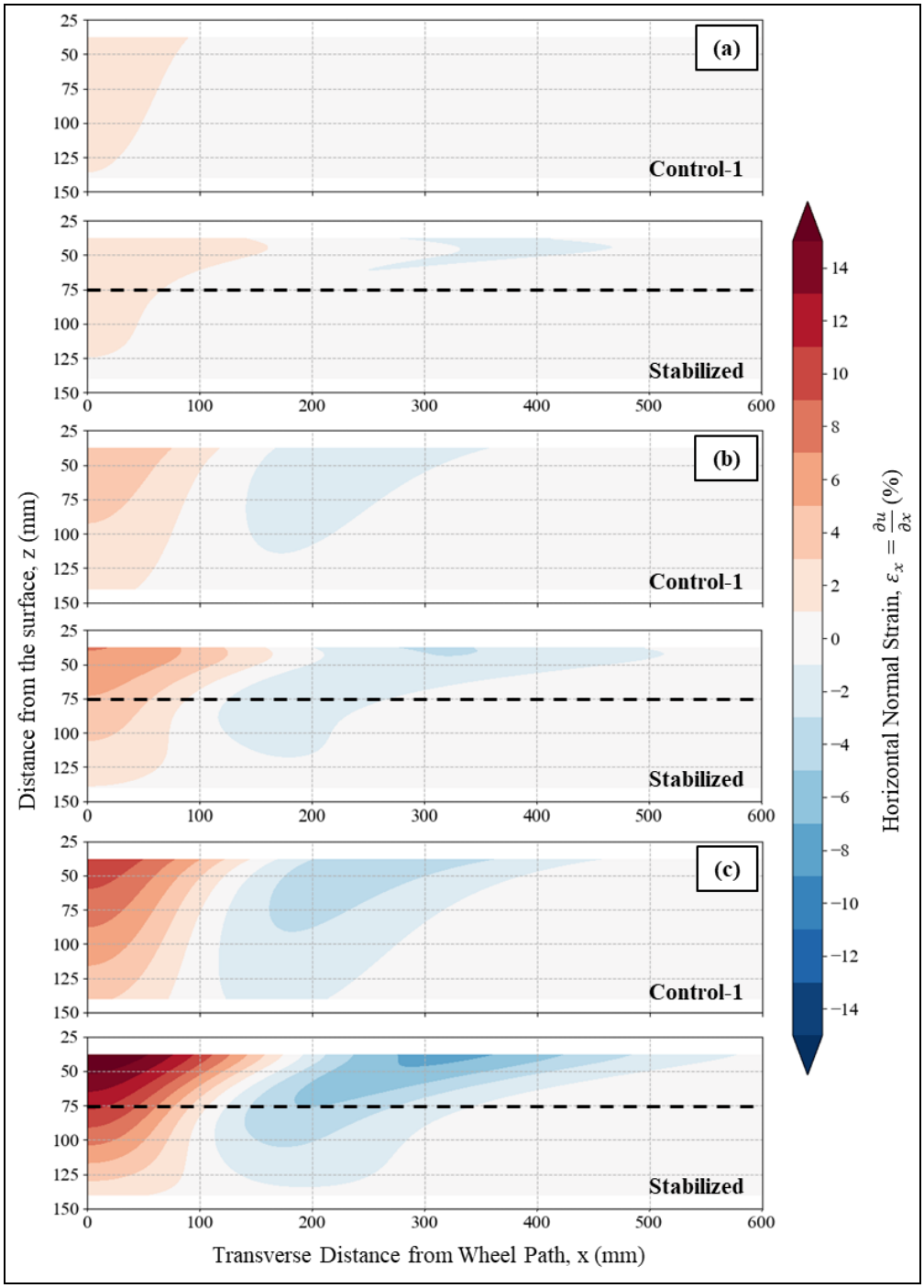

Figure 3.15. Normal strain fields at: (a) 1.5-mm; (b) 2.6-mm; and (c) 5.7-mm vertical deformation depth, d, along wheel path in control (C-1) and stabilized (S) sections.

Post-trafficking forensic trenching of the control and stabilized pavement sections at the end of testing showed no changes in the thickness of the subgrade and HMA layers. Thus, the surface deformation as measured by the profilometer can be assumed to equal the change in thickness of the base layer across the pavement section. This change in base layer thickness can be normalized with the initial base layer thickness (125-mm) to obtain the average vertical normal strain over the thickness of the base for increasing number of passes. The horizontal normal strain fields, such as those shown in Figure 3.14, were used to determine the average horizontal normal strain over the thickness of the base at any distance from the center of the wheel path. If plane strain conditions are assumed, the volumetric strain, averaged over the depth of the base as a function of the transverse distance from the wheel path, equals the sum of the vertical and horizontal normal strains. Since tensile strains are assumed to be positive, a positive volumetric strain indicates dilation. Chapter 2 details the methodology of obtaining the volumetric strains from the surface rut profiles and horizontal normal displacement fields. Figure 3.16 presents the results of a volumetric strain analysis on the control section after 100, 1000, 3000, 10000 and 20000 passes as dashed lines. Since the surface rut in the stabilized section was not measured after 20000 passes, the volumetric strain analysis after 100, 1000, 3000, 10000 and 30000 passes are shown as solid lines instead. Overall, the base aggregates exhibited a dilatant behavior, which agrees with the high relative density (85%) at which the base was placed during construction of the pavement section. For a similar number of passes (i.e., load), the control section showed a greater tendency for dilation than the stabilized section. For similar levels of vertical deformation (d) under the wheel path, i.e., comparing curves 1000 (C) – 3000 (S), 3000 (C) – 10000 (S), and 10000 (C) – 30000 (S), the stabilized section showed more significant dilation than the control section. The dilation in the control section was more constant with distance from the wheel path,

whereas the dilation in the stabilized section quickly reduced to zero with increasing distance. This implies volume changes in the control section were more distributed throughout the width of the pavement section, whereas these were more localized in the stabilized section, resulting in the narrower rut path and larger heave (Figure 3.8). After 30,000 passes, the stabilized section exhibited some contractive behavior far away from the wheel path, between 300-mm and 400-mm, corresponding to the location of maximum compressive strains in the normal strain field (Figure 3.15c).

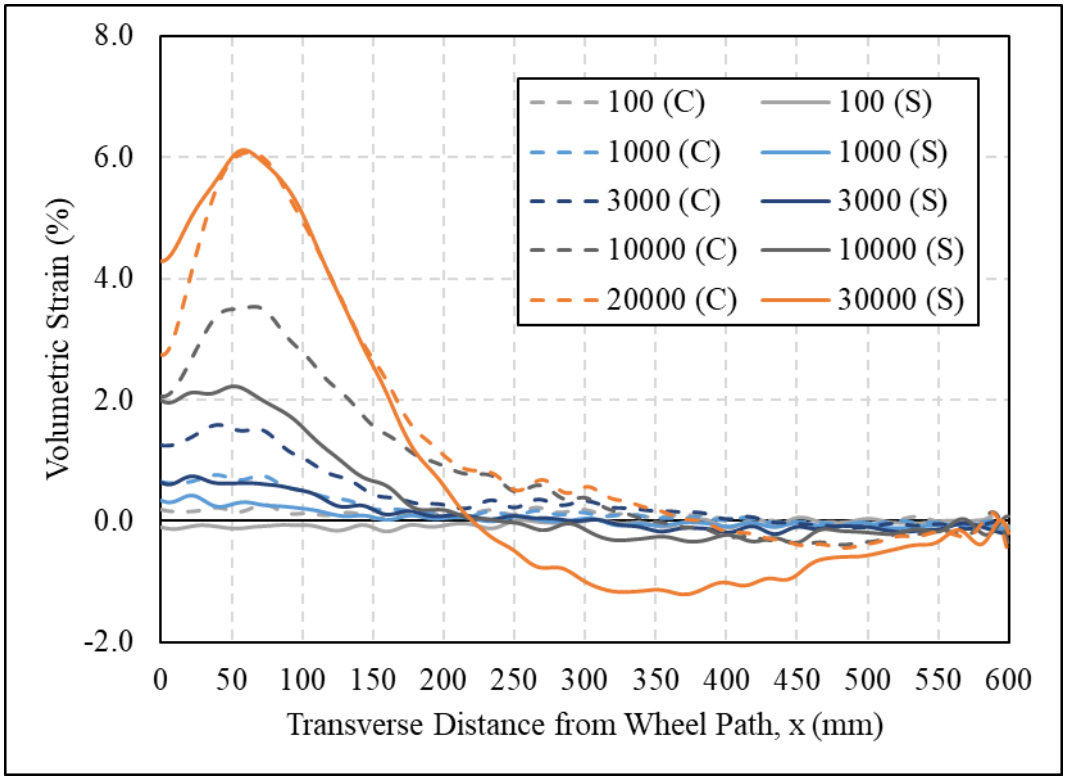

Figure 3.16. Volumetric strain with increasing number of passes in control (C-1) [dashed] and stabilized (S) [solid] sections.

3.3.3 Distribution of Vertical Stress

The vertical stress within the base and subgrade layers of the pavement section were continuously measured during trafficking using earth pressure cells, the layout of which is detailed in Figure 3.4. From the continuously monitored dynamic response of the earth pressure cells, the increase in stress due to the wheel load was determined for each pass. As discussed in Chapter 2, this dynamic increase in stress under the wheel load remained more or less a constant in both the control and stabilized sections throughout testing. The typical dynamic increase in stress recorded around the 3000^{th} wheel pass in the control and stabilized sections are compared in Figure 3.17. The y-axis shows the dynamic increase in vertical stress under traffic recorded by the earth pressure cells at various depths within the pavement structure, and the x-axis shows the transverse distance from the center of the wheel path at which the earth pressure cells were installed. The square, triangular and circular markers represent the earth pressure cells installed at mid-depth in the base, at the base-subgrade interface, and at the bottom of the subgrade, respectively. The blue markers represent the dynamic stress increase measured in the control section and the gray markers represent those in the stabilized section. The vertical stress under the center of the wheel path in both the control and stabilized sections decreased with an increase in depth, thus capturing the distribution of the applied load over a wider area with an increase in depth. Furthermore, the stress responses measured in the stabilized section were lower than those measured in the control section at the center of the wheel path, indicating a wider distribution of the applied load in the stabilized section due to increased unbound aggregate layer modulus induced by the increased confinement.

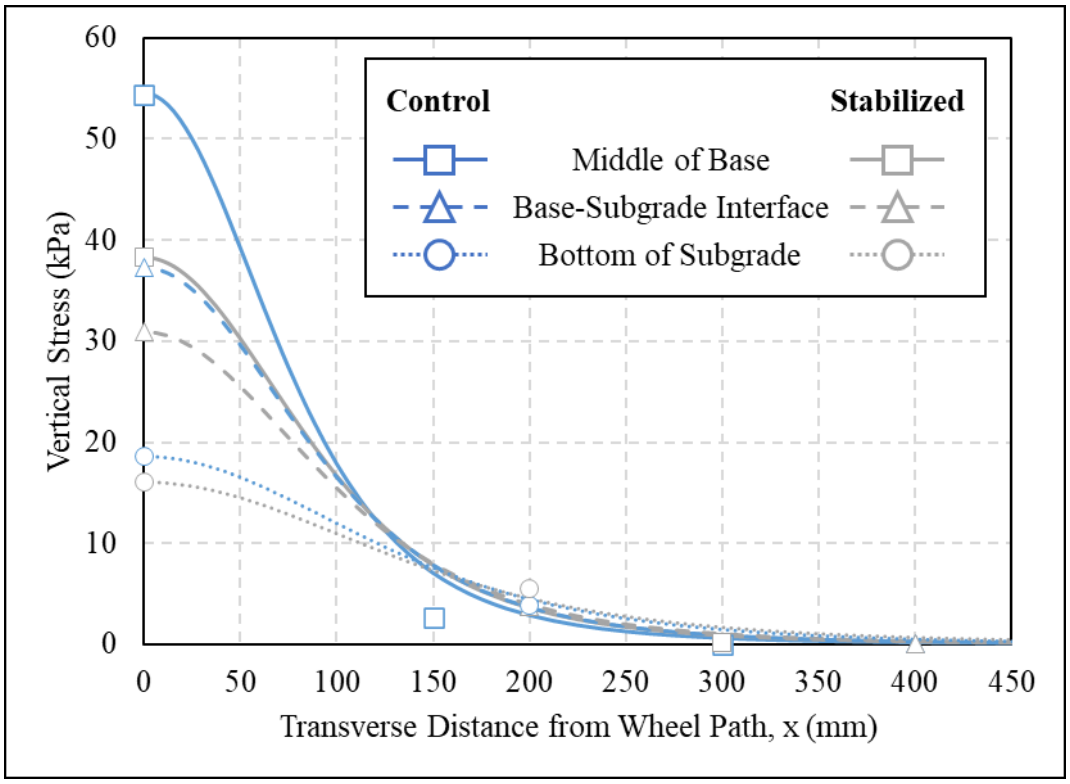

Figure 3.17. Vertical stress distribution after approximately 3000 passes in control and stabilized sections.

The discrete stress measurements within the control and stabilized sections at each depth were fitted with a parameterized form of the Boussinesq solution (Nwoji et al., 2017) for vertical stress distribution due to a point load, as detailed in Chapter 2. The solid, dotted, and dashed lines in Figure 3.17 represent the best fit curves for the vertical stress distribution at the middle of the base, base-subgrade interface, and bottom of the subgrade, respectively, with blue lines representing the control section and gray lines representing the stabilized section. The vertical stress decreased with depth under the wheel path and the vertical stress was distributed over an increased width at greater depths, resulting in increased vertical stresses with depth at locations far from the wheel

path (x > 150-mm). A wider distribution of vertical stress was also observed in the stabilized section, with lower vertical stress under the wheel path and increased vertical stresses away from the wheel path behaving analogous to a pavement section with increased thickness. In fact, the stress distributions at mid-base in the stabilized section and on top of the subgrade in the control section were very similar, indicating that the stabilized base, with reduced thickness, was equivalent in performance to the control section base, with full thickness. This wider distribution of vertical stress within the base of the stabilized section is considered compatible with the wider horizontal normal strain distribution (tensile region) under the wheel path when compared to the control section (Figure 3.14). While the magnitude of horizontal strains increased with traffic, the zones of compression and tension in the horizontal normal strain contours remained constant and consistent with the vertical stress distribution, which remained fairly unchanged throughout testing.

3.4 CONCLUSIONS

In this study, Accelerated Pavement Tests (APTs) were conducted on reduced-scale pavement sections under controlled environmental conditions, with the primary goal of evaluating the mechanisms involved in the stabilization of unbound aggregate layers by geogrids in flexible pavements. Two of the APTs were performed on non-stabilized (control) pavement sections to evaluate the repeatability of the tests, while the third APT was performed on a stabilized pavement section to evaluate the effectiveness of the stabilizing geogrid. Pavement section performance was monitored by measurements of vertical deformations at the surface, lateral displacements of particles in the base, and vertical compressive stresses within the base and subgrade. The horizontal displacement of aggregate particles within the base was measured using the particle

tracking sensor developed, as part of the previous study in Chapter 2, to assess the development of lateral restraint and other associated mechanisms involved in geogrid stabilization of unbound aggregate layers. The displacement data from over 25 particle tracking sensors installed within the base were used to develop a horizontal displacement field, vertical gradient of horizontal displacements, and horizontal normal strain fields for the two control sections and one stabilized section. The APT program discussed herein aided an understanding of the mechanisms involved in the stabilization of unbound aggregate layers in flexible pavements. The measurement of responses from two identical control sections helped establish the repeatability of the testing procedure. The development of lateral restraint was observed as a reduction in the lateral displacement of particles near the geogrid, and the particle tracking sensors proved very useful in measuring this effect. The measured surface deformation profiles and vertical stress distribution within the pavement structure in the control and stabilized sections were compatible with internal particle displacements and aided in understanding the pavement response to traffic.

- Surface rut measurements showed that the variability of rut between the two control sections (C-1 and C-2) was about 10%, with a traffic ratio of 1.0 ± 0.1.
- The displacement contours of the two control sections were found to be very similar in overall shape and equal in magnitude of the contours. The particle displacement measurements were found to be repeatable within 1 mm of displacement for similar rut.
- For the purposes of comparison between the stabilized and control sections through rut and particle displacement measurements, the APTs were found to have acceptable repeatability.

- Comparison of the surface rut measurements between the control (C-1) and stabilized (S) sections showed that the stabilized (S) section was capable of handling a 230% increase in traffic compared to the control sections. In other words, for a similar number of passes, the stabilized section produced shallower surface ruts compared to the control sections.
- Examination of the actual surface profiles revealed that the surface profiles from the stabilized section showed that for the same vertical deformation depth, (d), the rut profiles were narrower and the accompanying heave due to lateral flow about 20% taller than those in the control sections. The heave (h) as a fraction of the total rut (r) was found to be higher in the stabilized section.
- Displacement contours from the stabilized section showed redirected and reduced displacement of particles compared to the control for similar number of passes. At the same level of vertical deformation under the wheel path, the stabilized section showed redirection of particle flow accompanied by increased particle displacements at locations above the geogrid and decreased particle displacements at locations below the geogrid. Therefore, the inclusion of the geogrid to stabilize the unbound aggregate base resulted in redirection of the lateral flow in the base, mitigation of horizontal particle displacements near the geogrid and a reduction in the transfer of shear across the geogrid.
- The cumulative horizontal normal strains in the stabilized section were distributed over a wider area with lower magnitudes than in the control sections for similar number of passes.
- For the same level of deformation under the wheel path, the strains in the stabilized section above the geogrid were higher than those in the control section.

This increased strain magnitudes closer to the surface resulted in increased heave in the stabilized section compared to the control sections.

- The stabilized section showed lower volumetric dilation compared to the control sections at similar number of passes due to the increased confinement provided by the geogrid.
- The lateral restraint provided by the geogrid resulted in increased layer moduli, the effect of which was observed in the wider and shallower stress distributions in the stabilized section compared to the control section. Lower peak stresses under the wheel path and higher distributed stresses away from the wheel path were observed in the stabilized section relative to the control section.
- Vertical stress measurements remained more or less constant throughout testing in both the control and stabilized sections.

REFERENCES

AASHTO M43-05, 2022. Standard Specification for Sizes of Aggregate for Road and Bridge Construction.

AASHTO R50, 2009. Standard Practice for Geosynthetic Reinforcement of the Aggregate Base Course of Flexible Pavement Structures.

Baek, C., 2020. Performance evaluation of fiber-reinforced, stress relief asphalt layers to suppress reflective cracks. Applied Sciences 10, 7701.

Bender, D.A., Barenberg, E.J., 1978. Design and behavior of soil-fabric-aggregate systems. Transportation Research Record.

Bhattacharjee, S., Mallick, R.B., 2012. Effect of temperature on fatigue performance of hot mix asphalt tested under model mobile load simulator. International Journal of Pavement Engineering 13, 166–180. https://doi.org/10.1080/10298436.2011.653565

Christopher, B.R., Cuelho, E.V., Perknis, S.W., 2008. Development of geogrid junction strength requirements for reinforced roadway base design, in: Proceedings of GeoAmericas 2008 Conference, Cancun, Mexico. pp. 1003–1012.

Epps, A.L., Ahmed, T., Little, D.C., Hugo, F., 2001. Performance prediction with the MMLS3 at Westrack (Research Report No. FHWA/TX-01/2134-1). Texas Transportation Insitute, College Station, TX.

Guide for Mechanistic–Empirical Design of New and Rehabilitated Pavement Structures. (Final Report No. NCHRP Project 1-37A), 2004. . Transportation Research Board, National Research Council, Washington, D.C.

Haliburton, T.A., Lawmaster, J.D., McGuffey, V.C., 1981. Use of Engineering Fabrics in Transportation-related Applications. Haliburton Associates.

Kim, H., Sokolov, K., Poulikakos, L.D., Partl, M.N., 2009. Fatigue Evaluation of Carbon FRP-Reinforced Porous Asphalt Composite System Using a Model Mobile Load Simulator.

Lee, J., Kim, Y.R., McGraw, E.O., 2006. Performance evaluation of bituminous surface treatment using third-scale model mobile loading simulator. Transportation research record 1958, 59–70.

Lee, Jusang, Kim, Y.R., Lee, Jaejun, 2015. Rutting performance evaluation of asphalt mix with different types of geosynthetics using MMLS3. International Journal of Pavement Engineering 16, 894–905. https://doi.org/10.1080/10298436.2014.972916

Lee, S.J., Kim, Y.R., 2004. Development of fatigue cracking test protocol and life prediction methodology using the third scale model mobile loading simulator, in: 5th International RILEM Conference on Cracking in Pavements-Mitigation, Risk Assesment and Prevention. Edited by Petit C., Al-Qadi IL et Millien A. pp. 29–36.

Lee, S.J., Seo, Y., Kim, Y.R., 2006. Validation of material-level performance Models: Using the third-scale Model Mobile loading simulator. Transportation research record 1949, 74–82.

Martin, A.E., Walubita, L.F., Hugo, F., Bangera, N.U., 2003. Pavement Response and Rutting for Full-Scale and Scaled APT. J. Transp. Eng. 129, 11.

Nwoji, C.U., Onah, H.N., Mama, B.O., Ike, C.C., 2017. Solution of Elastic Half Space Problem using Boussinesq Displacement Potential Functions. Asian Journal of Applied Sciences 05, 7.

Perkins, S.W., 1999. Geosynthetic reinforcement of flexible pavements: laboratory based pavement test sections (Research Report No. FHWA/MT-99-001/8138). Montana. Department of Transportation.

Raab, C., Arraigada, M., Partl, M.N., 2016. Effect of reinforced asphalt pavements on reflective crack propagation and interlayer bonding performance, in: 8th RILEM International Conference on Mechanisms of Cracking and Debonding in Pavements. Springer, pp. 483–488.

Smit, A. de F., Hugo, F., Epps, A., 1999. Report on the first Jacksboro MMLS tests (Research Report No. FHWA/TX-00/0-1814-2). Center for Transportation Research, Austin, TX.

Smit, A. de F., Hugo, F., Rand, D., Powell, B., 2003. Model Mobile Load Simulator Testing at National Center for Asphalt Technology Test Track. Transportation Research Record 9.

Sun, X., Han, J., 2019. Mechanistic-empirical analysis of geogrid-stabilized layered systems: Part I. Solutions. Geosynthetics International 26, 273–285. https://doi.org/10.1680/jgein.19.00006

Tang, X., Chehab, G.R., Palomino, A., 2008. Evaluation of geogrids for stabilising weak pavement subgrade. International Journal of Pavement Engineering 9, 413–429. https://doi.org/10.1080/10298430802279827

TxDOT SS3239, 2004. Special Specification for Thin Overlay Mix (TOM).

van de Ven, M., Smit, A. de F., 2000. The Role of the MMLS Devices in APT, in: South African Transport Conference. Presented at the Action in Transport for the New Millenium, p. 16.

Van de Ven, M., Smit, A. de F., Lorio, R., McGennis, R., 1997. Validation of some superpave design parameters by wheel testing with the scale model mobile load simulator, in: Eighth International Conference on Asphalt PavementsFederal Highway Administration.

Zornberg, J.G., 2017. Functions and Applications of Geosynthetics In Roadways. Procedia Engineering 189, 298–306. https://doi.org/10.1016/j.proeng.2017.05.048

Chapter 4: Properties governing the Performance of Geogrid-Stabilized Flexible Pavements

ABSTRACT

Geosynthetics for stabilization of unbound aggregate layers in pavements are typically specified using their unconfined mechanical properties and/or their interaction properties under soil confinement for large displacements. However, geogrids used to stabilize the base layer of a pavement system are neither unconfined nor undergo large displacements. Using the results from accelerated pavement testing on multiple geogrids, this study evaluates the suitability of different variables commonly used to specify geogrids to capture the benefits resulting from their use to stabilize their base. The properties evaluated include a newly developed property, K_{SGC}, which is the coefficient of the Soil-Geosynthetic Composite stiffness obtained from Soil-Geosynthetic Interaction (SGI) tests. A series of identical one-third scale accelerated pavement tests (APTs) were performed on pavement test sections stabilized with various geogrids, diverse in terms of geometry and materials. The rutting from these sections was compared to that in the non-stabilized (control) section to evaluate the Traffic Benefit Ratio (TBR) at failure rut for each geogrid. The TBR showed poor correlations with index properties of the geogrid such as aperture size, tensile stiffness, and strength, and with performance properties of the geogrid with the base aggregate such as the pull-out resistance. On the other hand, the TBR showed a strong linear correlation to the soil-geosynthetic composite stiffness (K_{SGC}) of the geogrid-base aggregate composite. It is concluded that K_{SGC} is a particularly good indicator of the performance of pavements with geosynthetic-stabilized road bases.

4.1 INTRODUCTION

Over the past several decades, the role of geosynthetics in transportation projects has expanded into several new applications ranging from conventional structural improvement applications such as stabilization of weak subgrades or mitigation of reflective cracking in asphalt concrete to novel hydraulic applications such as facilitating drainage (Zornberg, 2017). The market has kept pace with these expanding applications of geosynthetics with several manufacturers introducing newer products claimed to perform the specific functions. The proliferation of geosynthetics for various applications demands the identification of appropriate properties that can be used to determine the geosynthetic best suited for the application in question. This study aims to provide a property that has the best potential to be used for selection of geosynthetics for stabilization of base courses in paved roads.

Stabilization of unbound pavement layers involves the inclusion of geosynthetics within an unbound aggregate layer and/or at the interface between layers. This is aimed at improving pavement performance by increasing the aggregate layer stiffness through trans-fer of stresses to the geosynthetic material. In paved roads, this transfer of stresses, to tension-bearing geosynthetic materials, limits the lateral movement of the stabilized pavement layer. This “lateral restraint”, which can be mobilized under relatively small deformations, is considered the dominant mechanism of performance improvement for geosynthetic-stabilized paved roads. Perkins et al. (2010) reports lateral restraint as involving the: (a) restrain of lateral movement of base, or subbase, aggregate (confinement); (b) increase in modulus of base aggregate due to confinement; (c) improved vertical stress distribution on subgrade due to increased base modulus; and (d) reduced shear strain along the location of the geosynthetic.

Geosynthetics are commonly marketed using index properties (such as aperture geometry, tensile strength and stiffness, flexural rigidity) which are inherent to the particular geosynthetic. Engineering projects specify geosynthetics based on these index properties as well as performance properties that govern their interaction with surrounding soils (such as pull-out resistance, interface shear strength). While these properties are particularly relevant in many engineering applications such as earth-retaining walls, embankments, or slope stability, they are not suited for the design of stabilized road bases.

These properties capture either the small-strain, unconfined behavior (as in the case of tensile stiffness or flexural rigidity) or the large-displacement confined interaction of the geosynthetics with the surrounding soil. However, under serviceable limits for surface pavement, the geosynthetic is under confined conditions but does not undergo large dis-placements. Thus, AASHTO R50 (2009), the standard for geosynthetic reinforcement of road bases recommends performing full-scale tests with geosynthetics to predict their field performance. Since this could be cost-prohibitive, researchers have developed correlations between geosynthetic properties and their field performance in stabilization (Archer and Wayne, 2012; Christopher et al., 2008). Thus, the current state of practice is to select geosynthetics for stabilization based on index properties determined under unconfined conditions or interaction properties under large displacements or a combination of both.

However, under serviceable limits for surfaced pavements, the geosynthetic would undergo relatively small displacements and thus the performance of the geogrid-stabilized pavements is expected to be governed by the interaction between the surrounding soil and the geogrid under small-displacement conditions. This is not considered in any of the conventional geosynthetic selection and testing procedures. In

this study, the soil-geosynthetic composite stiffness (K_{SGC}) characterized in the Soil-Geosynthetic Interaction (SGI) test (Roodi and Zornberg, 2017; Zornberg et al., 2017), is proposed for use in selection of geogrids for base stabilization. The SGI test quantifies the stiffness of the soil-geosynthetic interface under low strains which is a pertinent property for evaluating the confined performance of geosynthetic products in base-stabilized pavements.

4.2 ACCELERATED PAVEMENT TEST

4.2.1 Test Setup

In order to assess the performance of flexible pavement with stabilized base, reduced-scale pavement sections were constructed in the laboratory under controlled environmental conditions. These sections involved identical pavement configurations but stabilized with seven different types of geogrids. The testing program also included a section without stabilizing geosynthetic that served as the control against which the stabilized sections were compared to quantify the improvement in performance due to stabilization. A wide variety of geogrid products with different material and geometric properties were selected to be used for the stabilization of the base. All eight pavement sections consisted of a 150 mm subgrade, 125 mm base, and 25 mm hot mix asphalt (HMA) ride surface. The entire structure was built above grade in two modular frames, each 150 mm tall, which bounded the pavement sections on all four sides. The pavement structure was 1800 mm in length and 1800 mm in width with a total depth of 300 mm as shown in Figure 4.1. A low strength non-woven geotextile is used for separation between the base and the subgrade to prevent layer-intermixing under compaction and trafficking. The geogrid in stabilized sections was placed at a depth 75 mm below the HMA surface within the base.

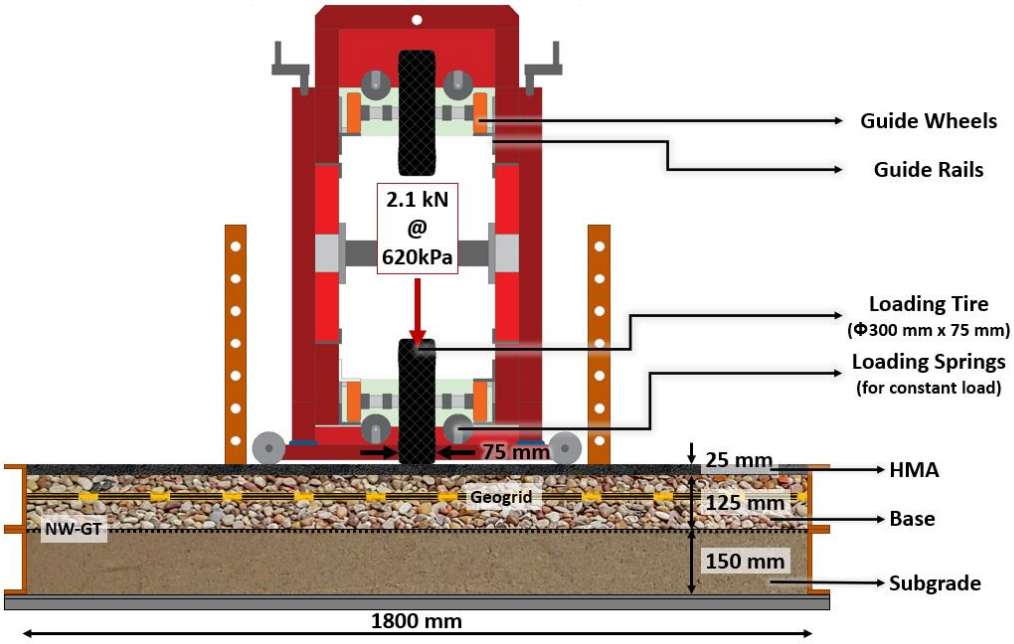

Figure 4.1. Schematic of the pavement cross-section used in this study.

4.2.2 Materials Used

A commercially available sand (Monterey 0/30), which is a clean uniformly graded sand with a D_{50} of 0.5 mm, and USCS classification of SP was used as the subgrade. The subgrade was placed in three lifts of 50 mm each, compacted to a dry unit weight of 15.4 kN/m^3 corresponding to a relative density of 67%. The base material used was a clean uniformly graded river-washed pea gravel with a D_{50} of 7 mm. This conformed to AASHTO #8 gradation (AASHTO M43-05, 2022) and classified as a poorly graded gravel (GP). The base was placed in one lift of 25 mm and two lifts of 50 mm, to a total thickness of 125 mm, compacted to a dry unit weight of 17.1 kN/m^3, corresponding to a relative density of 85%. Table 4.1 summarizes the properties of the subgrade and base material used in this study. The asphalt mixture used for the surface layer was a thin overlay mix (coarse) conforming to TxDOT Special Specification 3239

(2004) with a binder content of 6.5%. The seven different types of stabilizing geogrids, diverse in their material as well as geometric properties, are labelled GG1 to GG7 as shown in Figure 4.2. The geogrids GG2 and GG7 had triangular apertures while the other geogrids had rectangular apertures. Geogrids GG1, GG2, and GG7 were punched and drawn from polypropylene sheets, while GG3 was manufactured by extruding polypropylene strips and laser welding them resulting in a stronger junction. Geogrid GG4 and GG5 were made up of polyester yarns that were woven and coated with polyvinyl-chloride for increased aperture stability. The aperture sizes of the geogrids ranged from 15-mm (GG6) to 40-mm (GG3).

	Base	**Subgrade**
Commercial Name	River-washed Gravel (AASHTO #8)	Monterey Sand (0/30)
Average Size, D_{50} (mm)	7.0	0.5
Coefficient of Uniformity, CU	1.6	1.8
Coefficient of Curvature, CC	1.0	1.0
ASTM Classification	GP	SP
Specific Gravity, Gs	2.650	2.655
Dry Unit Weight (γ_d), kN/m^3	17.1	15.4
Relative Density (%)	85	67

Table 4.1. Properties of base and subgrade soils used in this study.

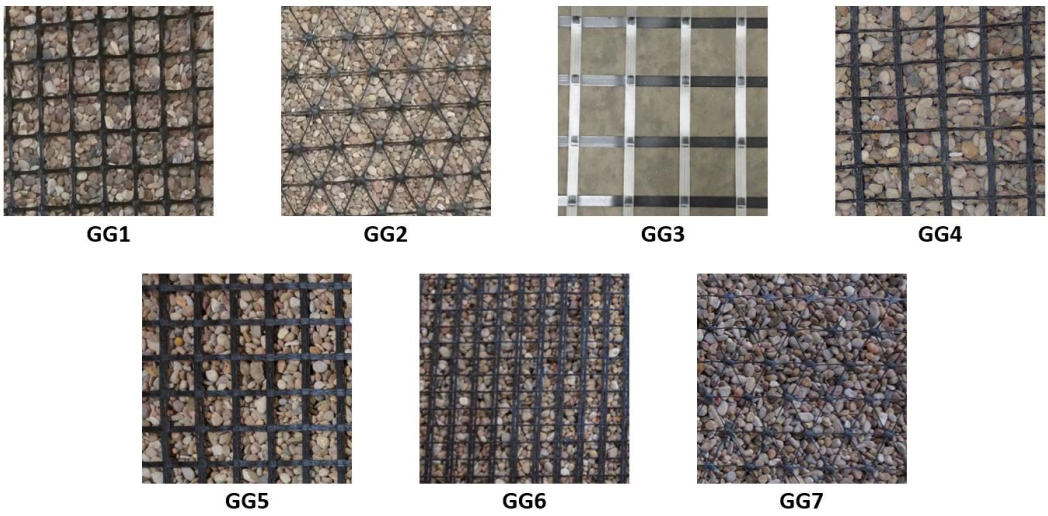

Figure 4.2. Geogrids used for stabilization in this study.

4.2.3 Trafficking Equipment

Rolling-wheel loads were applied onto the surface of the pavement sections using the model Mobile Load Simulator (MLS11, previously MMLS), a scaled-down prototype of a heavy vehicle simulator used for accelerated trafficking of pavement sections (Figure 4.3). The MLS11 is comprised of eight carriages with wheels that are guided along an obround guide rail by an electric motor and driving drum. Four of the carriages carry a 300 mm diameter loading tire and are used to apply the rolling-wheel loads on to the pavement surface, while the other four carriages serve as link sections in the continuous loop of carriages that are driven unidirectionally along the looped guide rail. The carriages with the trafficking tire contain a spring and hinge mechanism (suspension) attached to the axle that ensures the applied load remains constant within acceptable levels of surface deformation (up to 12 mm). The load is applied on to the pavement surface by lowering the MLS11 using the positioning screws on the four legs attached to the rigid frame. The continuous circular motion of the loading tires allows for rapid

application of loads up to 7200 passes per hour, facilitating a quick turnaround of tests. The specifications of the loading equipment are summarized in Table 4.2. Additional details about the operation of the equipment can be found in previous research (Epps et al., 2001; Kim et al., 1998; Kumar and Chehab, 2014; Martin et al., 2003; Smit et al., 1999; van de Ven and Smit, 2000) where the MLS11 was used to perform accelerated pavement tests. Several studies (Kim et al., 2009; Lee et al., 2015) have been performed to evaluate the benefits of using geosynthetic reinforcement to mitigate cracking and reduce rutting in asphalt concrete surface layers. With respect stabilization by geogrids, Tang et al. (2008) conducted accelerated pavement tests with MLS11 to evaluate the effectiveness of three different geogrid products in stabilizing weak pavement subgrade. They found the reduced-scale study was able to capture the effectiveness of geogrids in mitigating the development of rut through stabilization, although good correlations between the APTs and the bench-scale tests were not observed. The use of MLS11 to determine the benefits of base-stabilization by geogrids and to establish effective correlations with bench-scale test properties have not been reported.

Figure 4.3. MLS11 used for trafficking in this study.

Property	Specification
No. of Loading Tires	4
Wheel Diameter	300 mm
Tire Width	80 mm
Total Track Width	80 mm
Total Track Length	1100 mm
Load per wheel	2.1 kN
Tire contact pressure	620 kPa
Tire footprint area	34 cm^2
Loading Rate	120 passes per minute
Wheel velocity	2.5 m/s
Lateral wander	Disabled

Table 4.2 Relevant technical specifications of the MLS11 used in this study.

4.2.4 Surface Deformation Measurement

The benefits of geogrid stabilization of the base can be quantified by measuring the surface rut under increasing number of passes in the stabilized and control sections. The rut under the wheel-loading can be obtained from the measurement of the deformation of the pavement surface with traffic. In order to measure the deformed profile of the surface, a profilometer consisting of a laser distance meter (LDM) mounted on to the carriage of an actuator was used. The LDM used is the Disto D8, from Leica-geosystems, a commercial-grade laser distance meter with a Class-2 (IEC60825-1, 2014) visible red laser used in construction projects capable of making distance measurements with an accuracy of ± 1.0 mm and a resolution of 0.1 mm. The LDM communicated with

the PC over Bluetooth® and was capable of a maximum sampling frequency of 1 Hz on non-glossy, lighter surfaces. Since the HMA layer is very dark (black) and glossy, in order to reduce measurement errors and sampling time, the pavement surface was painted with non-gloss, off-white paint at locations where the profiles were obtained as shown in Figure 4.4 (begin, center, end and long).

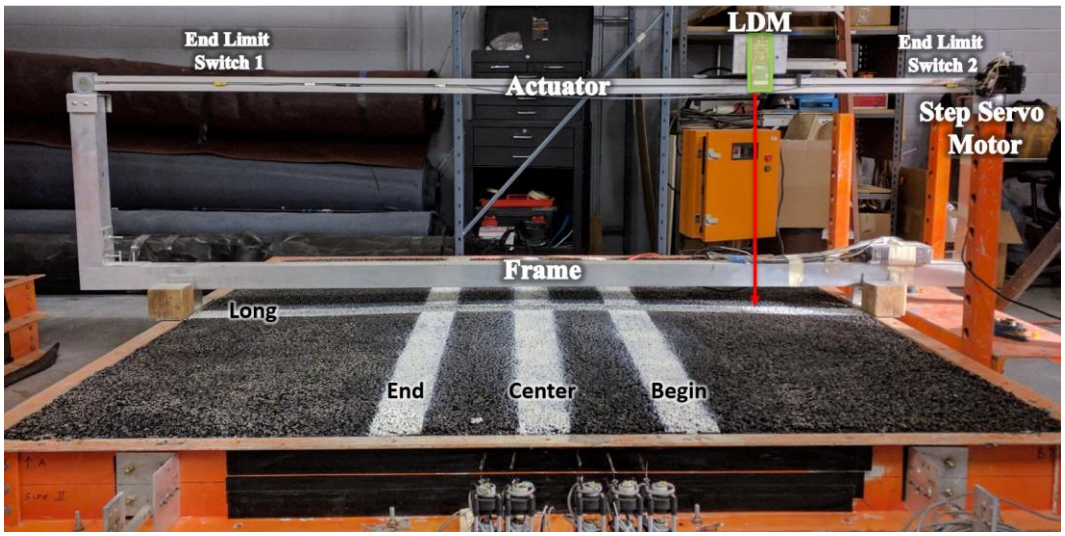

Figure 4.4. Components of the laser profilometer.

The LDM was mounted on to the glide-cart of the belt-driven actuator, from Macron-Dynamics. A step-servo motor (from Applied Motion Products, Inc.) was used to drive the pulley and belt assembly in the actuator to move the LDM mounted glide-cart back-and-forth across the longitudinal length or transverse width of the pavement section to obtain the surface profiles. In order to prevent the glide-cart from reaching the ends of the actuator at speeds, thereby causing damage to the actuator, hard stop limits were established using NPN-type end-limit proximity sensors near the ends of the actuator stroke length. The end limit switches on the step-servo motor were wired to the output of the proximity sensors to prevent stroke length exceedance. The actuator is mounted on an

aluminum frame that housed the power supply for the complete setup and provided the necessary elevation for the LDM to operate at its best accuracy.

The step-servo motor is controlled electronically from the PC and propels the LDM across the pavement surface as it profiles the distance from the bottom of the LDM to the pavement surface. By controlling the LDM sampling rate and actuator velocity, the LDM was programmed to sample the vertical distance from the actuator to the surface every 5 mm of horizontal actuator displacement. This allowed for the construction of transverse surface profiles with around 360 sample points over the 1800 mm. The surface profiles were obtained across three transverse locations, namely begin, center, and end transverse profiles, and also along the wheel path in the longitudinal direction. The surface of the pavement was profiled before the trafficking of the pavement sections, at pre-determined intervals during trafficking, and after the end of trafficking. The surface profiles post-trafficking is compared to the initial surface profile to determine the change in surface profile (the rut profile) at any given number of passes. Figure 4.5 shows an example of a transverse surface rut profile obtained from the profilometer. The x-axis represents the horizontal distance in the transverse direction from one edge of the pavement to another (x = 0 mm and x = 1800 mm). The y-axis shows the change in vertical position of the pavement surface after 10000 passes of rolling wheel load in the control section. The data collected from the LDM at approximately 5 mm intervals are shown using solid markers and a best-fit function used to fit the data is shown using the solid black line. It is observed that the pavement surface underwent a downward vertical movement, d under the wheel path, and is accompanied by heaves, h on either side of the wheel path. The surface deformation is observed to be reasonably symmetrical and hence, the location of the wheel path is assumed to be located at the point of maximum downward vertical deformation (x = 916 mm in Figure 4.5). The rut profile obtained from

the LDM is fit with a best-fit function in order to remove the influence of localized scatter in the deformation data on the final determination of rut, r. Further, the fitting process corrects the pavement profiles obtained after different number of passes for any vertical and horizontal drifts due to errors in the placement of the profilometer. This allows for a more accurate measurement of the location of the wheel path (m), the vertical deformation depth (d) under the wheel path, the location of the heaves (x_h), and the average magnitudes of the two heaves (h).

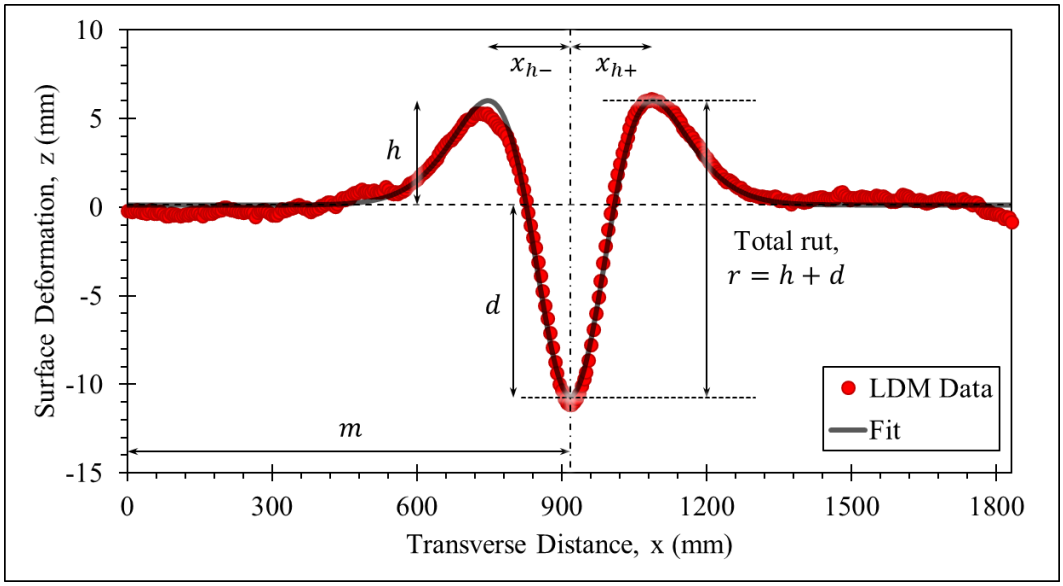

Figure 4.5. Surface rut profile as obtained from LDM and fitted function.

The fitting function used to obtain the best-fit of the rut profile data from the LDM is as follows:

$$z = \left(A_1 e^{-\frac{(x-m)^2}{2s_1^2}}\right)\left(A_2 e^{-\frac{(x-m)^2}{2s_2^2}} + (1 - A_2)\right) + B \qquad (4.1)$$

where, m is the location of the wheel path/correction for horizontal drift.

$A_1 < 0$ is the vertical deformation (d) under the wheel path.

$A_2 > 1$, $s_1 > 0$, and $s_2 > 0$ are fitting parameters that determine the shape of the surface profile.

B is the correction for vertical drift.

Equation (4.1) was selected as the function to fit the surface deformation data, $z(x)$ because its features capture the physical characteristics of the surface deformation data. Since the rolling wheel loads were applied in a controlled manner along the same wheel path with no lateral wander, provided a good quality of construction in terms of homogeneity of the material properties, any function used to define the rut profile must be symmetrical across the wheel path i.e., about $x = m$. The function must show a primary vertical deformation under the wheel path i.e., z_m and, in pavement sections subjected to lateral flow of base material, secondary vertical heaves that are symmetric about the wheel path (at $x = m \pm x_h$) i.e., z_h. Finally, the surface deformations (depression and heaves) are primarily observed in the vicinity of the wheel path and become negligible with increasing distances from the wheel path i.e., as $x - m \longrightarrow \pm \infty$. Equation (4.1) defined as a product of two modified gaussian functions satisfies all the above physical characteristics of the surface rut profile. The first term, a gaussian function $A_1 e^{-\frac{(x-m)^2}{2s_1^2}}$ with symmetry about x = m, defines the location (m) and magnitude (d) of the vertical deformation under the wheel path, whereas the second term, a modified gaussian function $A_2 e^{-\frac{(x-m)^2}{2s_2^2}} + (1 - A_2)$ also symmetric about x = m, modifies the simple gaussian function to define the locations ($x_{h\pm}$) and magnitude (h) of the heaves as a function of A_2, s_1, and s_2. Both terms, and hence the overall function, is symmetric about the location of the wheel path ($x = m$) and asymptotically decays to zero surface deformations as $|x\text{-}m|$ increases i.e., at large distances from the wheel path. The location

of the function minimum i.e., the wheel path and the function maxima i.e., the heaves are determined by setting the derivative of '*z*' with respect to '*x*' equal to zero. The derivative of the vertical deformation with the transverse distance is given by:

$$\frac{dz}{dx} = \left(-A_1 e^{-\frac{(x-m)^2}{2s_1^2}} \frac{(x-m)}{s_1^2}\right)\left(A_2 e^{-\frac{(x-m)^2}{2s_2^2}} + (1-A_2)\right) + \left(A_1 e^{-\frac{(x-m)^2}{2s_1^2}}\right)\left(-A_2 e^{-\frac{(x-m)^2}{2s_2^2}} \frac{(x-m)}{s_2^2}\right)$$

Therefore, setting the derivative to zero and simplifying yields the following

$$-A_1 e^{-\frac{(x-m)^2}{2s_1^2}} (x-m)\left[\frac{A_2}{s_1^2} e^{-\frac{(x-m)^2}{2s_2^2}} + \frac{1-A_2}{s_1^2} + \frac{A_2}{s_2^2} e^{-\frac{(x-m)^2}{2s_2^2}}\right] = 0$$

For non-trivial fitting parameters, solving for '*x*' from the above equation yields the following:

$x = m$ …….. at wheel path and (4.2)

$x = m \pm \sqrt{2s_2^2 \, ln\left(\frac{s_1^2+s_2^2}{s_2^2} \times \frac{A_2}{A_2-1}\right)}$ …… at the heaves (4.3)

Substituting the value of '*x*' at the locations of minimum and maxima, the magnitude of the vertical deformation under the wheel path (*d*) and the heaves (*h*) measured from the baseline (*B*) are obtained as follows:

$d = z_m - B = A_1$ ……. at wheel path and (4.4)

$h = z_h - B = A_1(1-A_2)\left(\frac{A_2-1}{A_2} \times \frac{s_2^2}{s_1^2+s_2^2}\right)^{\left(\frac{s_2}{s_1}\right)^2} \left[\frac{s_1^2}{s_1^2+s_2^2}\right]$..... at the heaves (4.5)

Thus, the rut profile obtained as the change in surface deformation profiles can be fit with the function in Equation (4.1), and the fitting parameters of the functions can be used to determine the location and magnitude of the vertical deformation (*d*) under the wheel path and the heave (*h*) adjacent to the wheel path. Figure 4.6 is used to establish that, for a given pavement configuration, the shape of the rut profiles remains the same with increasing number of passes and that the profiles are scalable with number of passes. This assumption of scalable rut profiles was validated as follows. The measured surface rut profiles obtained from the center transverse location of the control section after 1000, 3000, and 10000 passes are shown as solid lines (blue, orange, and gray respectively) in Figure 4.6. The total rut after 1000, 3000 and 10000 passes are obtained from the corresponding rut profiles as r_{1000}, r_{3000}, and $r_{10000,}$ respectively. The profiles obtained after 1000 and 3000 passes can then be scaled such that the total rut, after scaling, equals the total rut after 10000 passes i.e., the rut profiles after 1000 and 3000 passes are multiplied by a factor of r_{10000}/r_{1000} and r_{10000}/r_{3000} respectively. The scaled profiles after 1000 and 3000 passes are shown in Figure 4.6 as dashed-double lines (blue and orange, respectively). It is observed that the profile obtained after 10000 passes, and those obtained through scaling after 1000 and 3000 passes are very similar to each other in terms of their shape i.e., the location and magnitude of the vertical deformation under the wheel path and that of the heaves in the three profiles are essentially the same. Thus, it may be concluded that, while the magnitude of the deformation increases with increasing traffic, the overall shape of the profile i.e., the location of the heave relative to the wheel path, and magnitude of the heave relative to the vertical deformation under the wheel path remains essentially the same throughout the life of the pavement test section. This characteristic shape of the rut profiles is consistent with lateral flow being the dominant, if not the only mechanism of rut development in the pavement sections trafficked in this

study, as discussed in Papers 1 and 2. The temporal scalability of the rut profiles is also consistent with the temporal scalability of the horizontal internal particle displacements (showing lateral flow within the base) with increase in traffic. Thus, the fitting parameters that determine the profile shape (A_2, s_1, s_2) can be kept the same when fitting multiple profiles obtained after increasing number of passes, while the parameters that determine the maximum rut (A_1) and those needed to correct for horizontal and vertical drifts (m and B) are varied for the individual profiles.

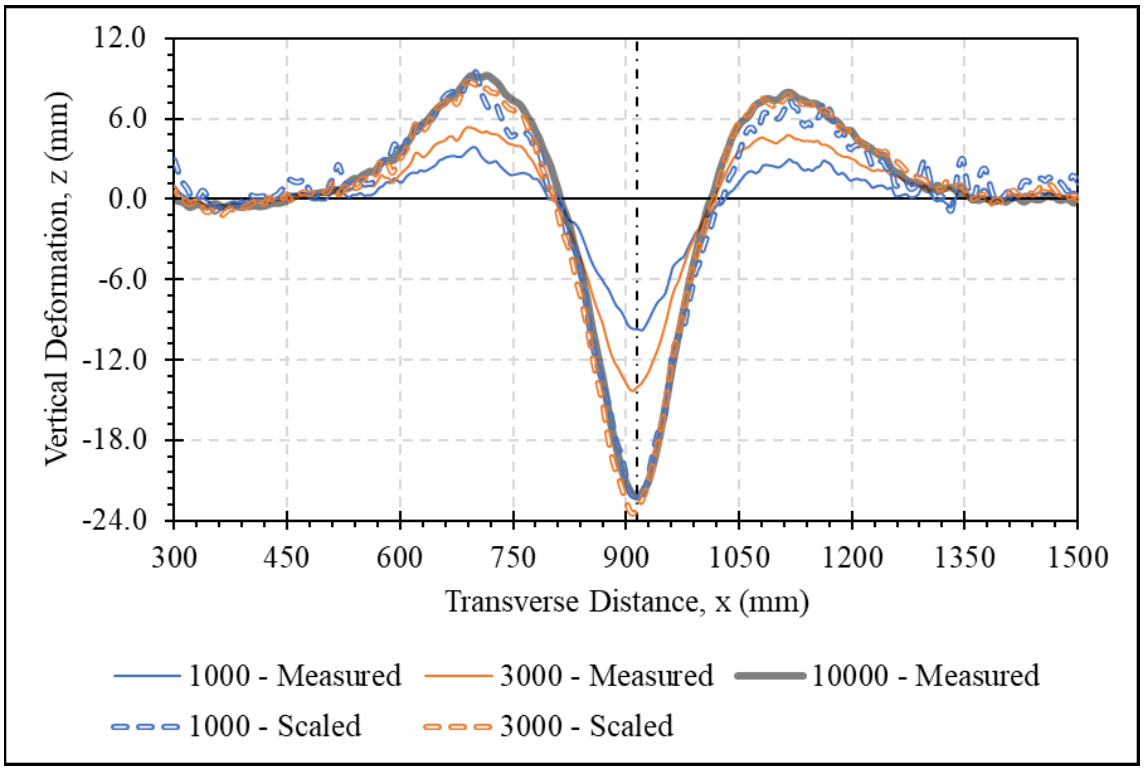

Figure 4.6. Scaling of surface rut profiles to determine similarity in profile shape with increasing traffic.

A similar analysis was performed across profiles obtained at the same number of passes, but across the three different transverse profiling locations. Figure 4.7 shows the

measured surface rut profiles obtained after 10,000 passes from the begin, center, and end transverse locations of the control section as solid lines (blue, orange, and gray respectively), post-scaling by factors of r_{center}/r_{begin}, 1, and r_{center}/r_{end}, respectively. The results indicate that the profile obtained at the three transverse profile locations after 10,000 passes are very similar to each other in terms of their shape. Thus, it was determined that the location of the heave relative to the wheel path, and magnitude of the heave relative to the vertical deformation under the wheel path remains essentially the same across the various profiling locations. Thus, the shape determining fitting parameters (A_2, s_1, s_2) of the rut profile can be assumed to be the same when fitting profiles obtained across the three different profiling locations, while the other three parameters (A_1, m, and B) are particular to each location, and account for local variability in vertical deformation (d) and drifts in profile measurements. Overall, from the observations made from Figure 4.6 and Figure 4.7, it is concluded that the shape of the rut profile associated with a particular pavement configuration (cross-section) is unique and, consequently, it can be scaled to account for temporal (increasing number of passes) and spatial (local variation along the wheel path) effects in order to generate the individual rut profiles.

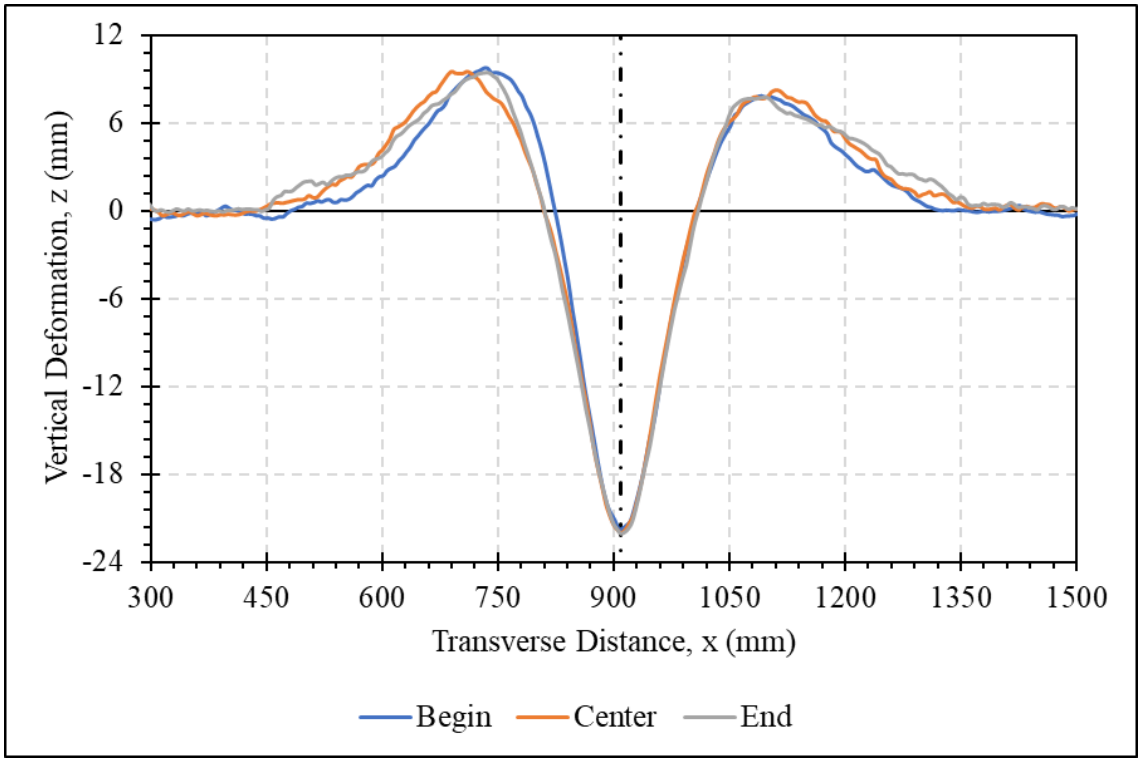

Figure 4.7. Similarity in shape of surface rut profiles obtained at different profiling locations.

Figure 4.8 shows the measured surface deformation profiles in the control section for increasing numbers of passes at the three transverse profiling locations (begin, center, and end). The circular markers represent the actual measured surface rut profiles, and the solid lines represent the fitted rut profile function with the same shape parameters (A_2 = 1.8, s_1 = 179.0 mm, and s_2 = 76.6 mm) for all of the 15 profiles measured across the various locations after increasing number of passes. The parameters for the magnitude of deformations (A_1) and drifts (m and B) are individualized for each of the 15 profiles. From the shape parameters, the location and magnitude of the heave relative to the location of the wheel path ($x - m$) and vertical deformation under the wheel path (h/d) are determined as follows:

$$x_h - m = \pm\sqrt{2s_2^2\, ln\left(\frac{s_1^2 + s_2^2}{s_2^2} \times \frac{A_2}{A_2 - 1}\right)} \tag{4.6}$$

$$\frac{h}{d} = (1 - A_2)\left(\frac{A_2 - 1}{A_2} \times \frac{s_2^2}{s_1^2 + s_2^2}\right)^{\left(\frac{s_2}{s_1}\right)^2}\left[\frac{s_1^2}{s_1^2 + s_2^2}\right] \tag{4.7}$$

The values of *(x_h – m)* and *(h/d)* are unique to the pavement section being analyzed and are independent of the level of traffic and the location of the profiling. For the control section , these values are *(x_h – m)* = 177.8 mm and *(h/d)* = 0.40. Thus, the total rut, *r*, for any level of traffic, and at any profiling location can be obtained from the individualized surface deformation parameter *(A_1)* for the particular profile and the global *(h/d)* ratio for the entire pavement section as follows. That is the rut is given by:

$$r = A_1\left[1 + \left(\frac{h}{d}\right)_{global}\right] \tag{4.8}$$

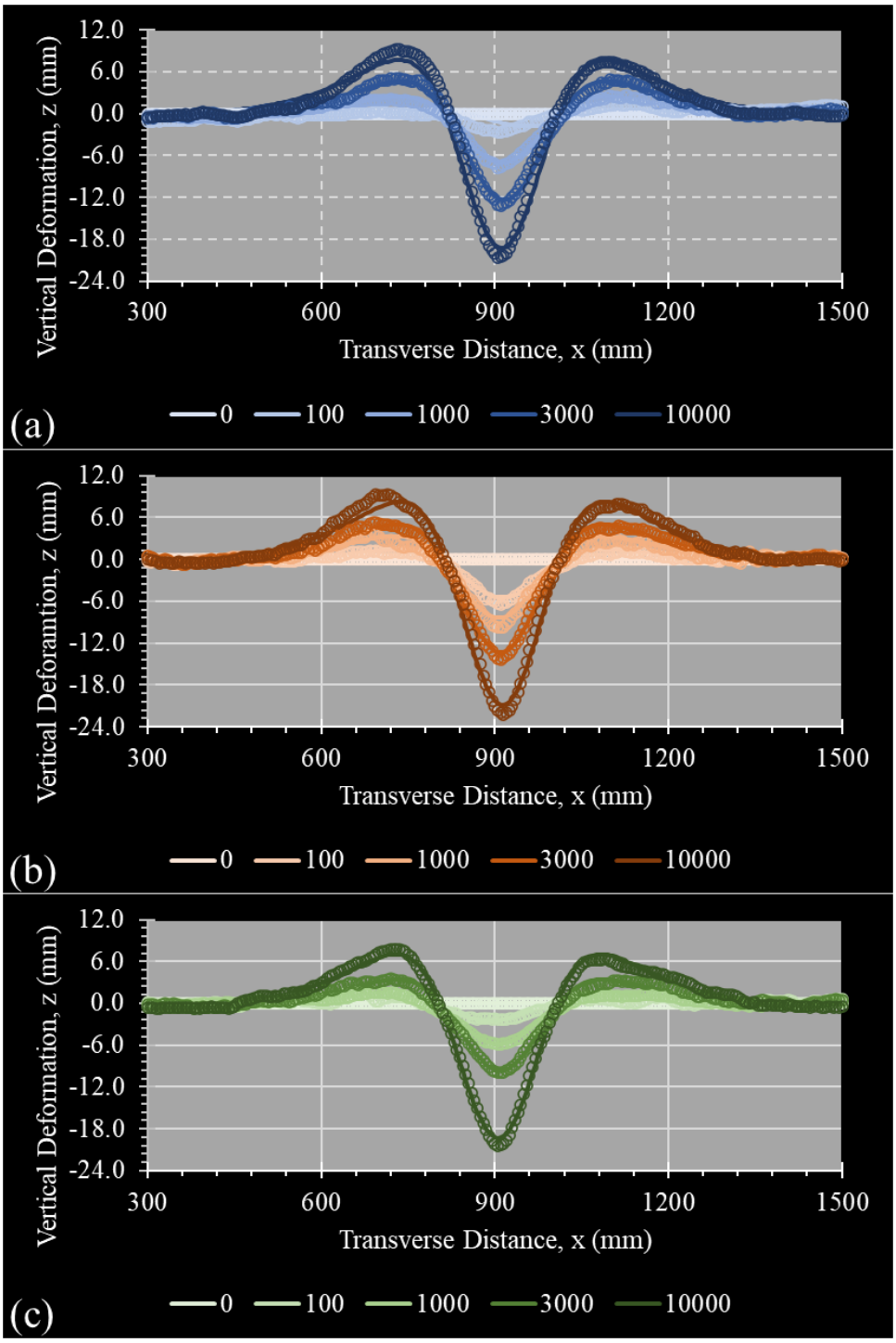

Figure 4.8. Surface deformations fit with rut profiles in the control section: (a) begin; (b) center; (c) end profile locations.

Figure 4.9 shows the results obtained by using Equation X to the each of the 5 profiles obtained at different number of passes from the three profiling locations. The total rut, r obtained at the three locations (begin (blue), center (orange), and end (gray)) were averaged for a given number of passes to obtain the average of rut development (black) with increasing number of passes, which will be used to compare the performance of the different geosynthetic-stabilized pavement sections evaluated in this study. The rut development shows a steep initial portion up to around 100 wheel passes, which can be attributed to initial compression and reorientation of the particles in the base (shakedown). This initial trend is followed by a reasonably linear, shallower rut development (from lateral flow) up to the end of the test.

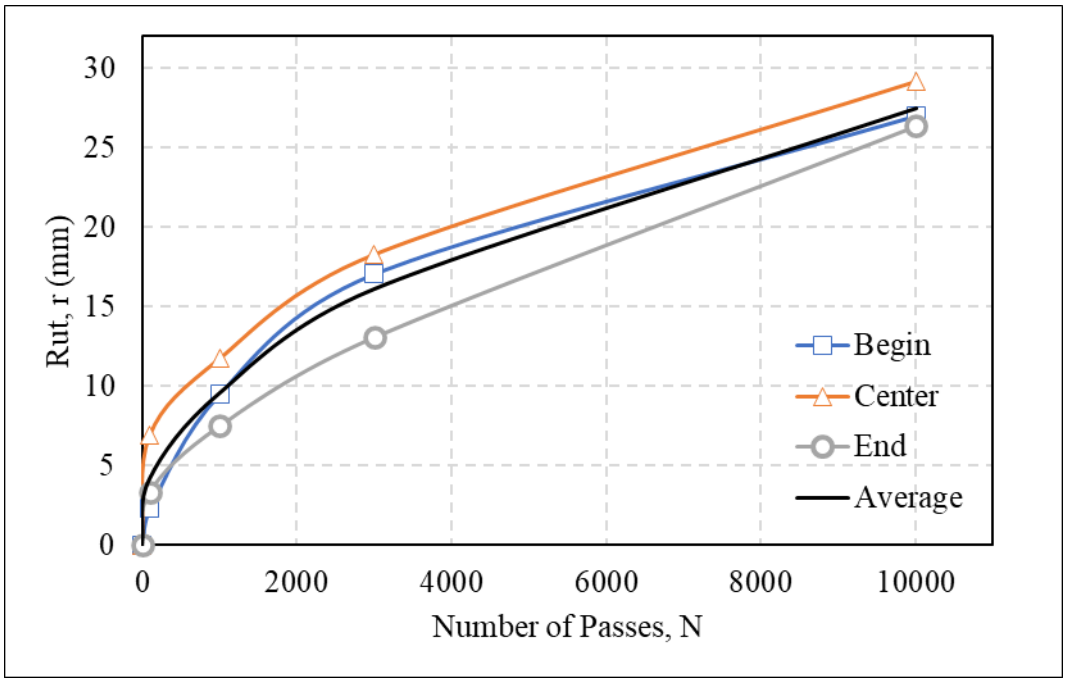

Figure 4.9. Rut development in the control section at begin, center and end profile locations.

The development of ruts in the stabilized (GG1) and control sections are compared in Figure 4.10. As discussed in paper 2, the presence of the geogrid for stabilization redirects and reduces particle movement during lateral flow. In addition to those effects, the geogrids used in this study reduced the initial portion of steep rut development by reducing the particle reorientation under shakedown as seen from the rut development curves in Figure 4.10(a). The benefits of stabilizing the base using a geogrid can be quantified by the traffic benefit ratio (TBR). AASHTO R50 (2009) defines the TBR as the ratio between the number of load cycles (wheel passes) in a stabilized pavement structure to reach a defined failure criterion and the number of load cycles in a control section needed to reach the same failure criterion. Thus, the TBR of a stabilized section is calculated as a function of defined failure criterion $r_{failure}$. Paper 2 provides details about the computation of the TBR vs. failure rut. The relationship between TBR and $r_{failure}$ for the GG1 stabilized section (see Figure 4.10(b)) can be described as showing three phases. The first phase (ranging from 0 mm to 3 mm rut depth) in which the TBR is continuously increasing, corresponding to an increase in pavement life when both the control and stabilized sections are in the initial shakedown domain (rapid rut accumulation). The second phase, ranging from 3 mm to 10 mm rut depth, is characterized by the control section being in the shakedown domain (rapid rut accumulation) and the stabilized section being in the lateral flow domain (slower rut accumulation). This results in a transitory increase in the TBR to a peak value until the control section reaches the lateral flow domain, followed by a reduction in TBR to an asymptotically constant value as lateral flow becomes the dominant mechanism in the control section. The third phase, ranging from 10 mm rut depth to the end of test, in which the TBR remains asymptotically at a constant value, corresponds to both the control and stabilized sections in the lateral flow domain (slow rut accumulation). The

TBR asymptotes to the constant value equal to the ratio of the slopes of rut development curve of the stabilized and control sections.

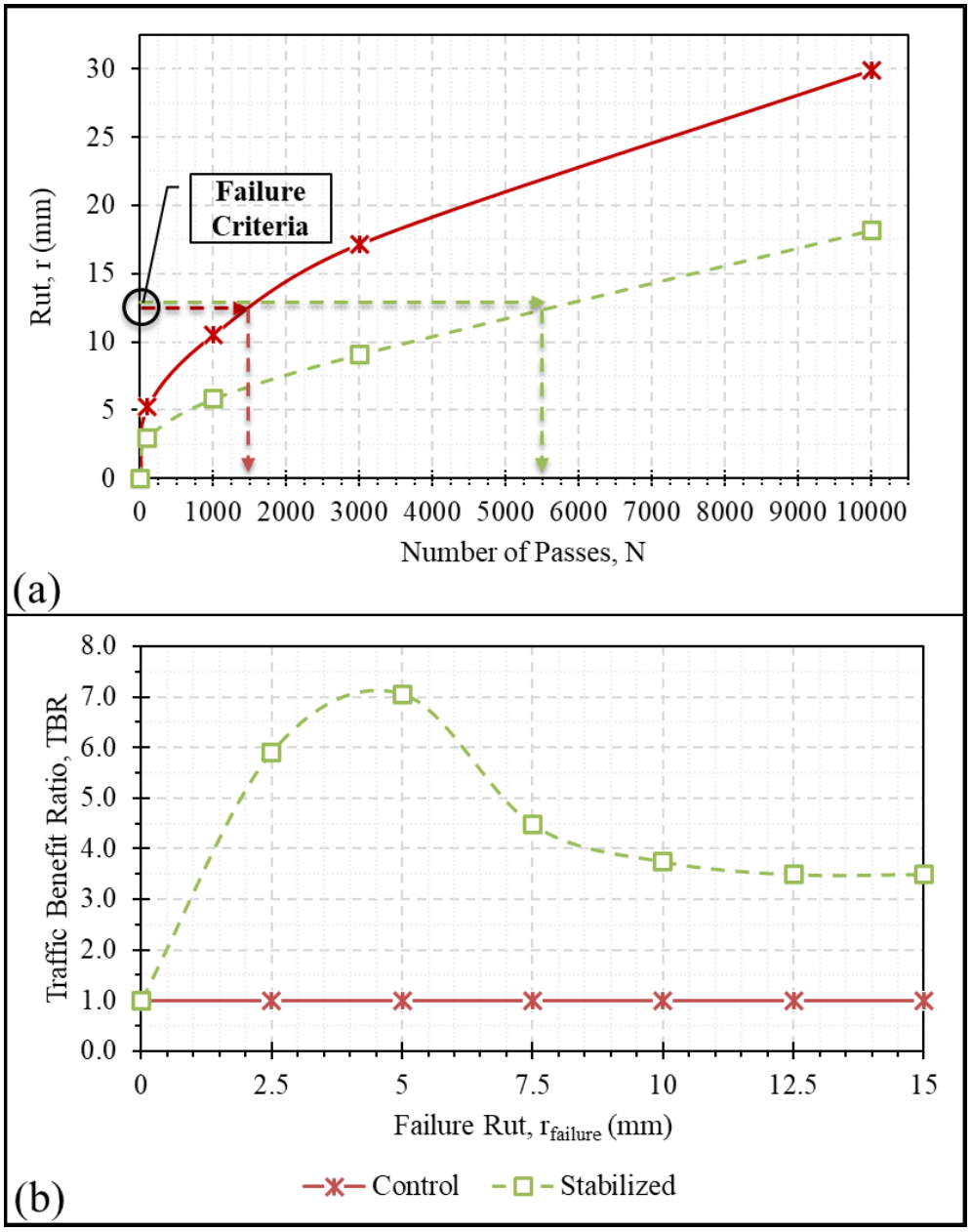

Figure 4.10. Quantification of benefits from geosynthetic stabilization: (a) rut development (stabilized vs. control); (b) traffic benefit ratio.

The development of rut with number of passes in the control section and in the seven sections stabilized with the various geogrids (GG1 to GG7) were determined following the previously described procedure and are shown in Figure 4.11(a). The corresponding TBR curves as a function of failure rut (r_f) obtained by comparing the rut development with number of passes in the stabilized sections with that in the control are shown in Figure 4.11(b). All the TBR curves show the characteristic three phase behavior of early shakedown, transition to lateral flow, and pure lateral flow. However, the range of rut over which the three phases dominate varies with the geogrid used for stabilization and its ability to limit the extent of settlement through shakedown. Geogrids such as GG2, GG3, and GG5 show an early transition from shakedown to lateral flow, while geogrids such as GG1, GG6, and GG7 show an intermediate transition, and finally GG4 shows a relatively late transition with equal parts of shakedown and lateral flow range in the GG4 section and the control section. Since the focus of this study is on understanding and ultimately mitigating the lateral flow mechanism, the TBR corresponding to the asymptotic value reached at a rut of 12.5 mm is used to evaluate the performance of the stabilized sections.

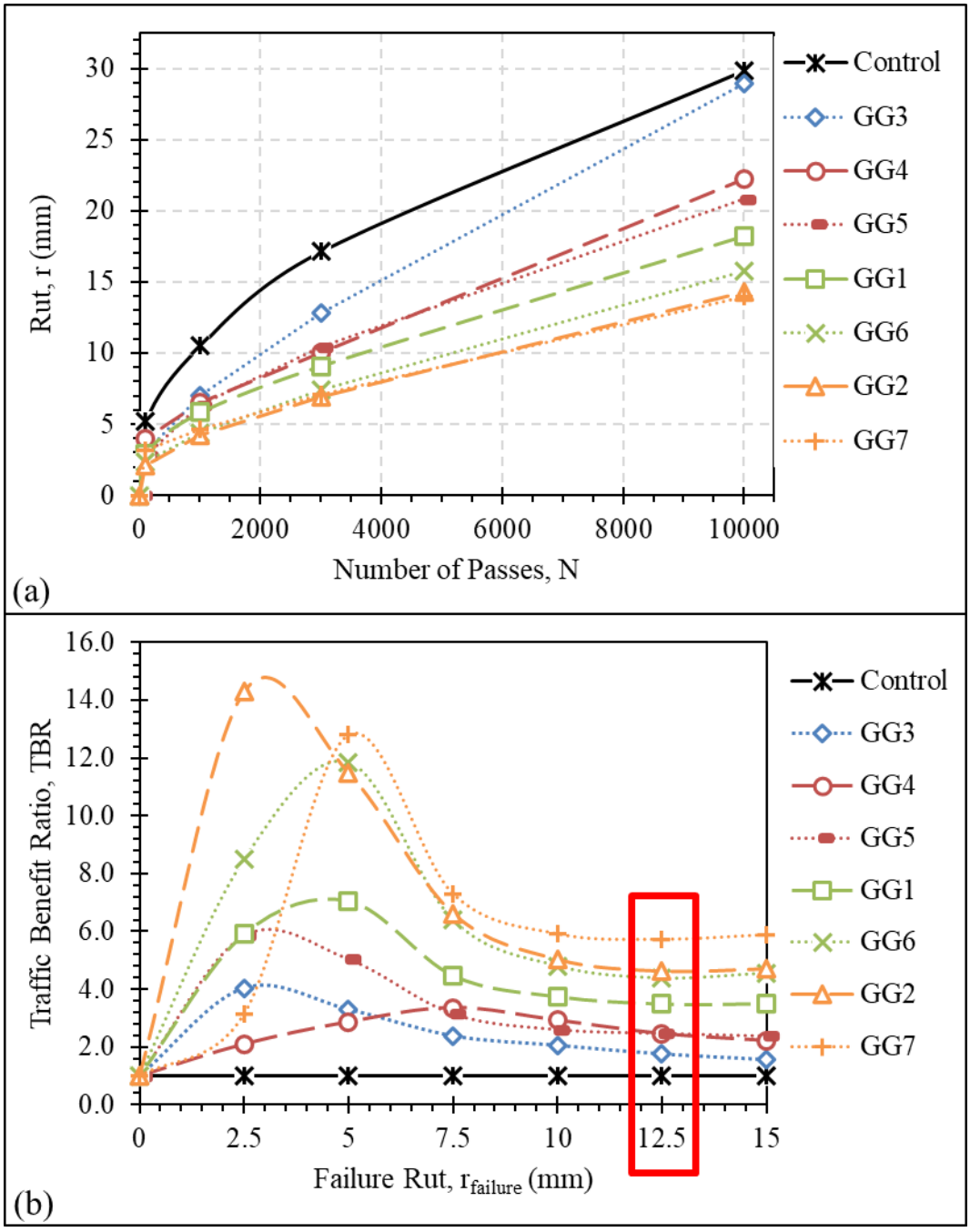

Figure 4.11. Comparison of the performance of control and stabilized sections: (a) rut development; (b) traffic benefit ratio.

Figure 4.12 shows the traffic benefit ratio obtained for a failure rut criterion of 12.5 mm in the 7 stabilized sections as a function of the shape of the surface rut profile, characterized by the location ($x_h - m$) and relative magnitude (h/d) of the heave. As the benefits from stabilization (TBR) increase, the location of heave becomes closer to the wheel path, indicating a narrowing of the wheel path rut. Also, an increasing TBR is observed to correlate positively with the normalized heave (h) observed for the same vertical deformation (d) under the wheel path. Paper 2 describes in detail the mechanisms associated with the narrowing of the wheel path and increased heave for the same deformation (d). The redirection of particle flow within the base by the stabilizing geogrid, and the reduction of shear transfer across the geogrid resulting in lower particle movements below the geogrid for the same level of rut results in increased lateral flow above the geogrid which increases the heave next to the wheel path and narrows the rut path.

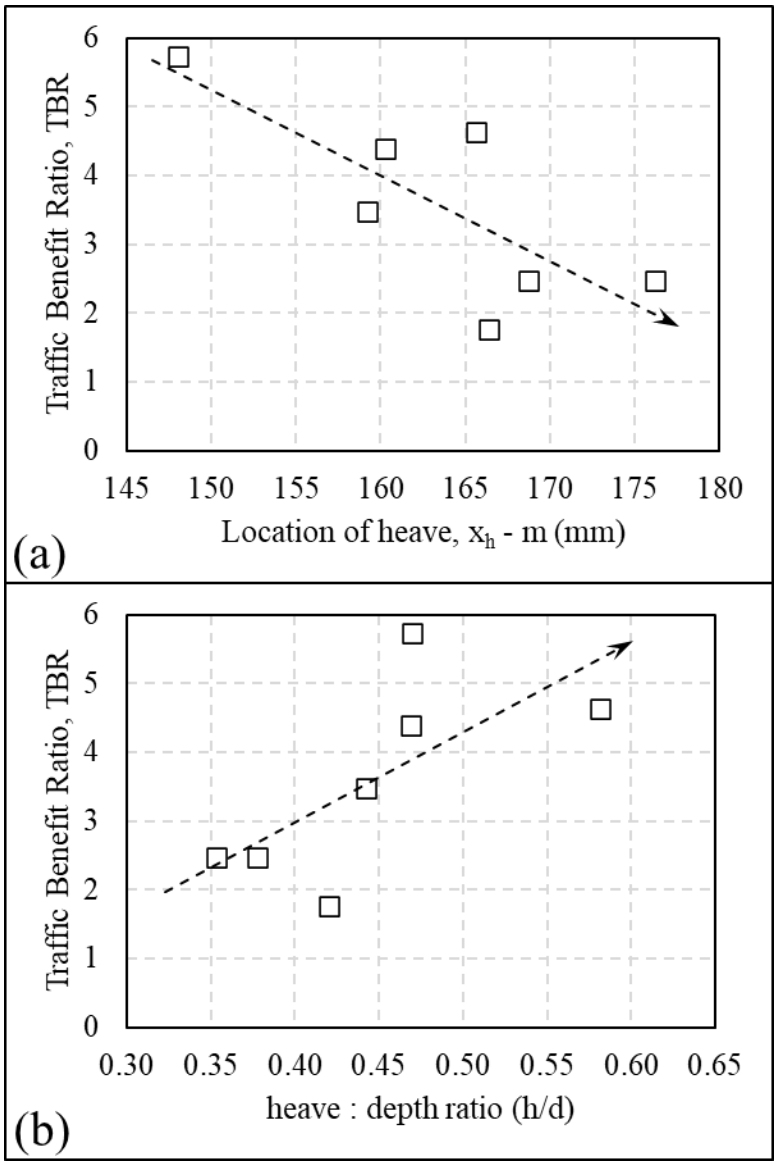

Figure 4.12. Correlation between parameters defining the shape of surface rut profiles and traffic benefit ratio (TBRs): (a) location of heave ($x_h - m$); (b) heave to depth ratio (h/d).

4.3 CORRELATIONS BETWEEN TBR AND GEOSYNTHETIC PROPERTIES

The benefits of stabilizing the base with geogrids in the reduced-scale pavement sections investigated in this study were quantified by the TBR values corresponding to a

rutting failure criterion of 12.5 mm . While the TBRs have been obtained for a limited number of geogrids, in order to predict the performance of the pavement section stabilized with a geogrid that was not a part of this study correlations may be developed between properties of the geogrids or soil-geogrid composites and the traffic benefit ratios. These correlations, based on geogrids studied for their stabilization benefits, may then be used to predict the benefits from the use of any other geogrid with properties within the range used in the study. Several researchers have attempted to develop correlations between the performance of geogrid-stabilized flexible pavements and the in-isolation geogrid properties (index properties) or performance properties such as interaction properties obtained under the confinement of soil. The index properties that had been most commonly used in specifications and previous correlation studies (Brown et al., 2007; Indraratna et al., 2012; Sakleshpur et al., 2019; Tang et al., 2008; TxDOT DMS6240, 2017) are: (1) geometric properties such as aperture size, rib thickness, rib width, percent open area, apparent opening size (in case of geotextiles) (2) material properties such as ultimate tensile strength, tensile stiffness (i.e., strength at 1%, 2%, and 5% strains), flexural rigidity, junction strength (and efficiency), aperture rigidity. Performance properties such as the ultimate pullout resistance (from a pull-out test), interface shear strength (from direct-shear tests) have also been used to predict the performance of the geosynthetics in stabilization of the unbound aggregate layers (Sakleshpur et al., 2019; Tang et al., 2008). Such correlations are standard practice in the pavement industry, so much so that several DOTs utilize these properties in their specifications for geosynthetic product selection to be used in stabilization projects. For instance, the Texas Department of Transportation's Departmental Materials Specification for Geogrid for Base Reinforcement (DMS6240, 2017) specifies a combination of aperture size, percent open area, rib thickness, junction efficiency, aperture shape, and

tensile modulus @ 2% elongation for identifying geogrids to be used for pavement projects. In this section, an evaluation is presented of correlations between the TBRs obtained from the APTs and some of the geogrid index properties and performance properties of the soil-geogrid composite.

4.3.1 Geometric Properties

The geogrids used in this study (Figure 4.2) involved different aperture shapes, including square, rectangular, and triangular shapes. In order to be able to compare the aperture sizes across the various geogrids with different geometric shapes, the area of the aperture was calculated using the formulas for square (a^2), rectangle (l x b), and the equilateral triangle ($\sqrt{3}\ s^2/4$). Then the area was characterized by the side length of an equivalent square with area a_{eq}^2. From this, the average opening size is determined as a_{eq}. Figure 4.13 shows the relationship between TBR and the average aperture size. The geogrids with similar opening sizes (between 25 mm and 30 mm) showed a wide range of TBR from 2.0 to 6.0 resulting in a poor correlation coefficient (with $R^2 = 0.463$).

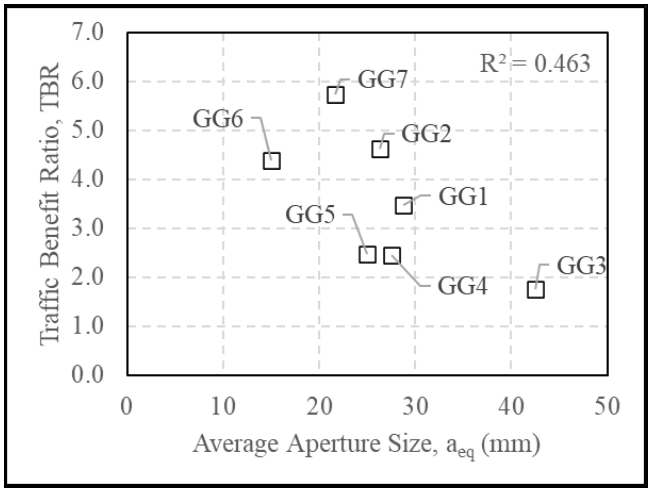

Figure 4.13. Correlation between traffic benefit ratio and average aperture size.

4.3.2 Tensile Properties

In order to determine the unconfined tensile properties of the geogrids in the transverse direction, wide width (multi-rib) tensile tests were conducted according to ASTM D6637 (2015) on six specimens of each of the seven geogrids used in this study. While the applied tensile load was measured using a load cell according to the ASTM standard, the strains in the geogrid specimens were measured by tracking the displacements of the marked nodes of the geogrid specimen through image analysis. A python program based on the OpenCV2 (open computer vision) module was developed for the purposes of this image analysis. The geogrid nodes were marked with distinct blue or white markers with a cross to enable object tracking of the markers with increase in load. Figure 4.14 shows the images obtained at the start and end of the test on one of the GG1 geogrid specimens. The markers (in white and blue) numbered from 3 to 42 were used to track the nodal displacements of the geogrid. The white markers 1 and 2 were fixed onto the upper moving roller grip and the lower stationary lower grip to determine their positions with increasing load. The displacement of Marker 1 (on the upper moving grip) measured from the object tracking program was verified with the LVDT mounted onto the load frame to measure grip displacement and was found to be within 5% of each other. The lower marker 2 (on the stationary grip) was used to ascertain that the camera did not displace during the duration of the test. The length of each individual vertical rib between the top row of markers (3, 8, 12, 18, 23, 28, 33, 38) and the bottom row of markers (7, 12, 17, 22, 27, 32, 37, 42) were determined from each image obtained during the test. The change in length of an individual rib over the course of the test was calculated by the measured lengths of the rib from the images taken over the course of the test. This change in length was normalized by the length of the rib as measured at the beginning of the test to determine the strain in the individual rib. The strains obtained

from the 8 active transverse ribs were averaged to determine the overall strain in the multi-rib geogrid specimen at any point in the test. The applied load is normalized with respect to the width of the geogrid specimen to obtain the unit tension. This unit tension was plotted against the average strain obtained from the image analysis as shown in Figure 4.15 and was used to obtain geogrid index properties such as (1) unit tension at 2%, (2) unit tension at 5%, and (3) ultimate tensile strength. The properties (1) and (2) are measures of tensile stiffness of the geogrid at various strain levels, whereas the property (3) is a measure of the geogrid strength in the transverse direction.

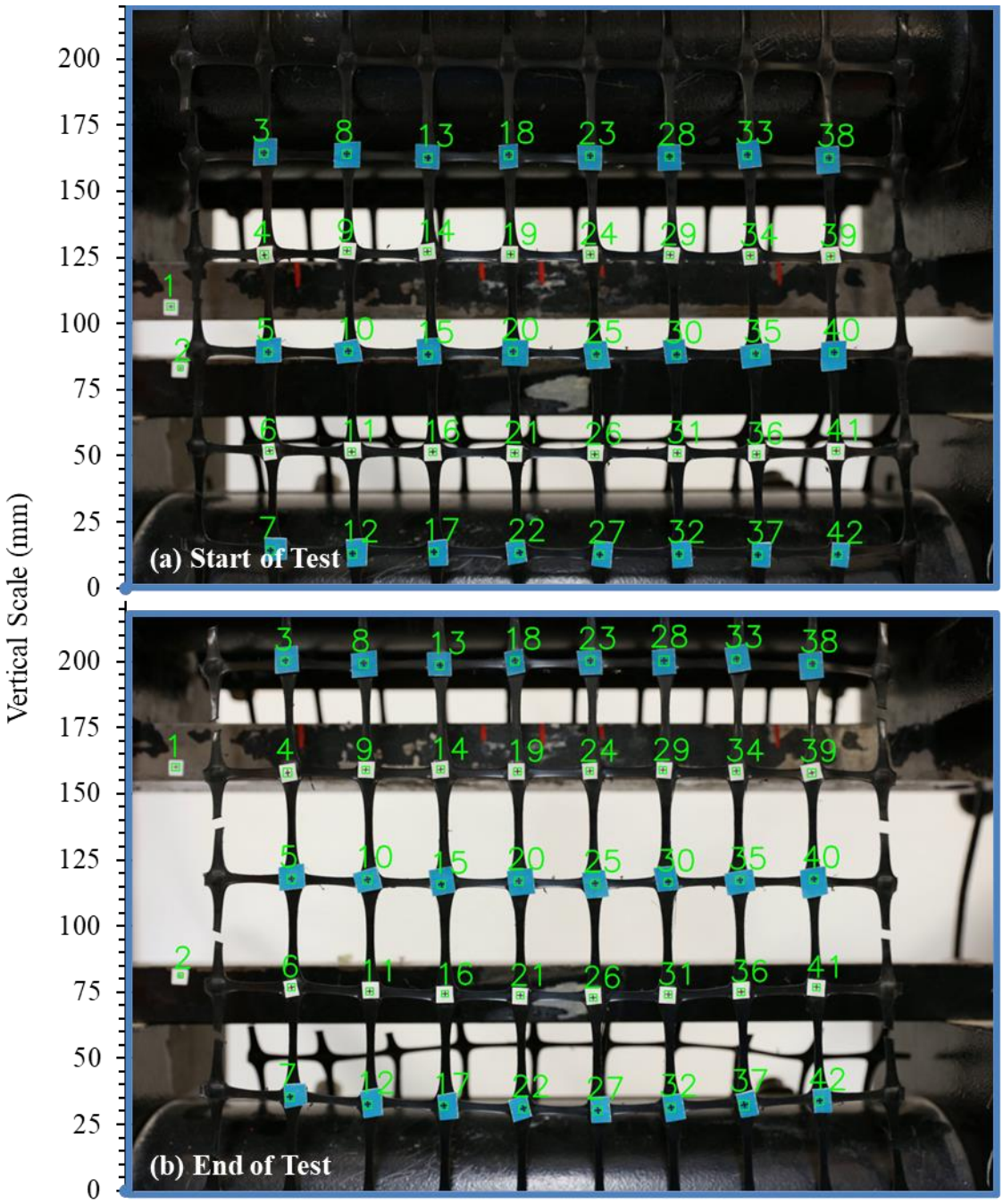

Figure 4.14. Tracking geogrid nodes with markers: (a) start of test; (b) end of test.

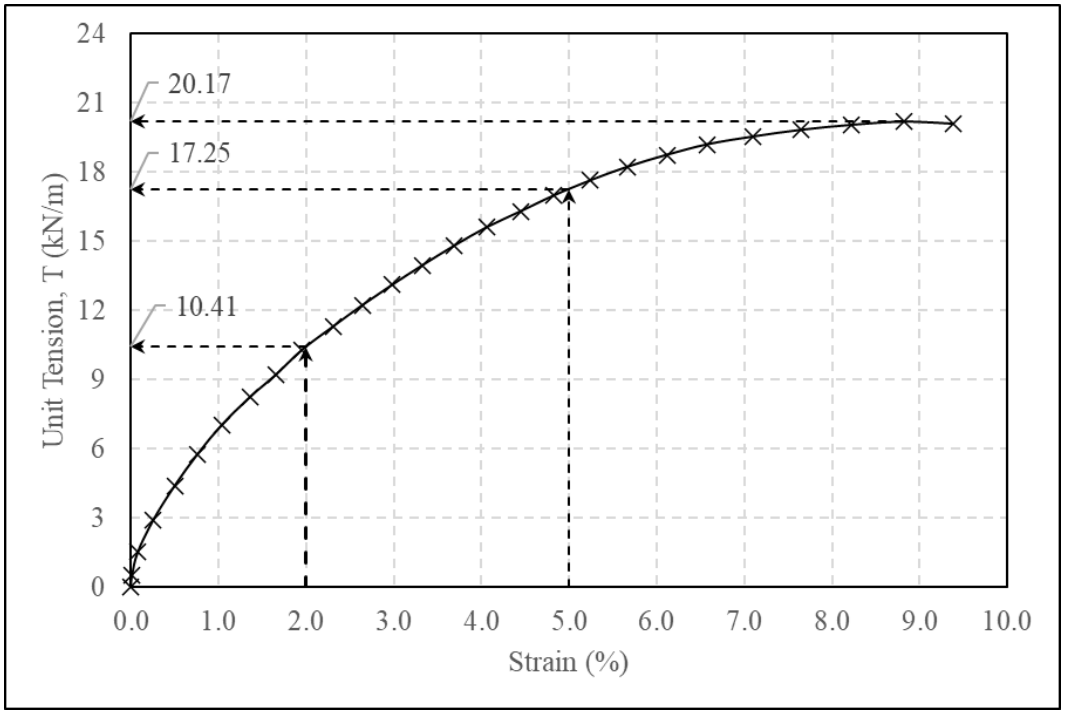

Figure 4.15. Unit tension obtained from normalized load plotted against averaged strains obtained from image analysis.

Figure 4.16 shows the correlation of the TBR with the measure of tensile stiffness of the geogrid. Both the plot of the unit tension at 2% and at 5% are very similar in their distribution and differ only in the actual magnitude of the unit tension, with that at 5% being higher than that at 2%, as expected. Overall, both measures of tensile stiffness show poor correlation with the TBR with R^2 values of 0.172 and 0.250 for the unit tension at 2% and 5% respectively. When a straight line was forced to fit to the cluster of data, it was observed that: (1) the correlation was negative, indicating that the TBR decreased with increasing tensile stiffness; (2) the correlation was poor with significant scatter. However, further inspection of the results in Figure 4.16 reveal that if the two geogrids with triangular apertures (GG2 and GG7) were excluded from the analysis, the tensile stiffness of the remaining 5 geogrids showed a positive correlation with the TBR,

with reduced scatter i.e., for the rectangular geogrids the TBR was found to increase with increasing tensile stiffness. Thus, for geogrids with rectangular apertures only, the transverse tensile stiffness of the geogrid in a wide-width tensile test was found to be a reasonable predictor of performance of geogrids used for stabilization. Whereas, in the case of triangular geogrids, due to the collapse of the grid structure under unconfined tensile loads, uniaxial tensile stiffness measurements were shown to be poor predictors of performance under confined applications such as stabilization.

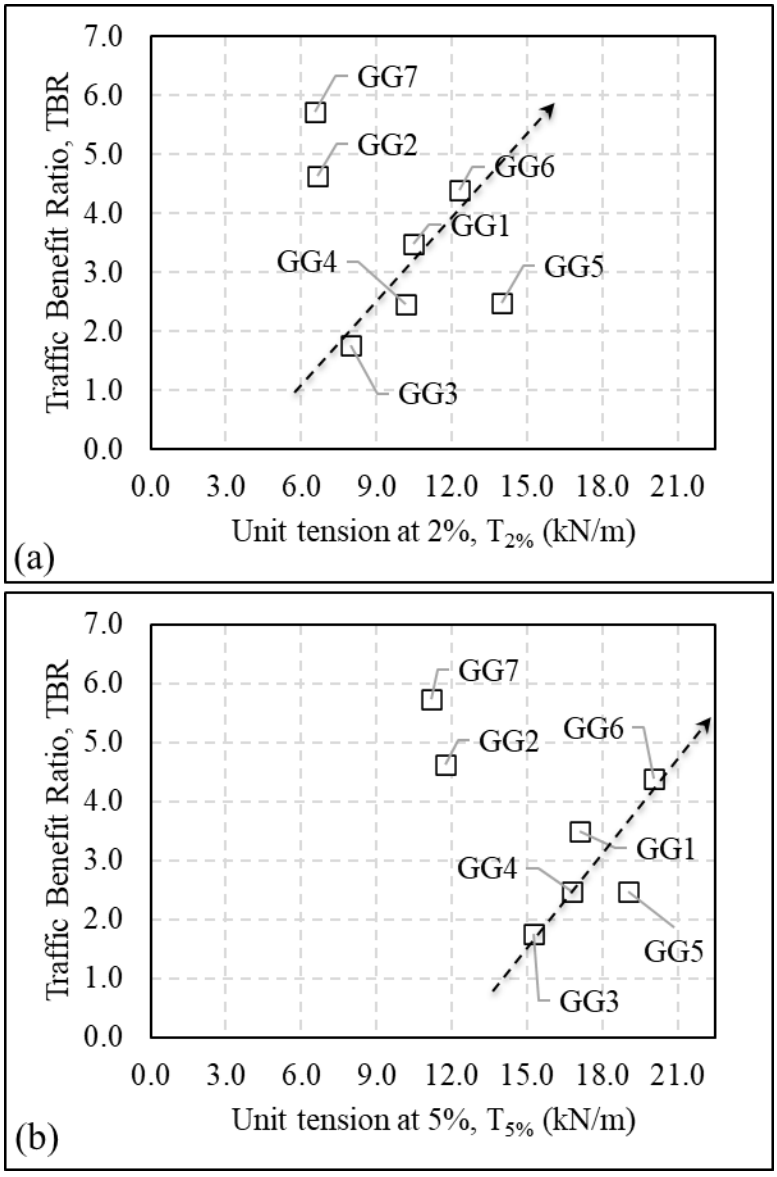

Figure 4.16. Correlation of traffic benefit ratio with tensile stiffness of the geogrids: (a) unit tension at 2%; (b) unit tension at 5%.

Figure 4.17 shows the correlation between TBR and the tensile strength of geogrids. It is observed that the performance of the stabilized pavements, as quantified by the TBR, correlates poorly with the ultimate tensile strength of the geogrids used for the stabilization. Most of the geogrids used in this study (except GG5) had an ultimate tensile

strength of roughly 20 kN/m, while the TBR obtained from sections stabilized with those geogrids was found to range from less than 2.0 to 6.0. It is noted that the geogrid with lowest ultimate tensile strength (GG7) performed the best amongst the various geogrids used in this study. The poor correlation between the ultimate tensile strength and the TBR is understood to be a consequence of their measurements being made at entirely different strain levels. The ultimate tensile strength of these polymeric geogrids is measured roughly around the 8% to 10% strain levels when the geogrids fail in tension. Whereas in a flexible pavement, especially in paved roads, in order to achieve a 10% strain in the geogrid, the adjoining soil must also undergo at least 10% strain which is excessive when it comes to meeting the serviceability criteria for the pavement structure. Thus, the geogrids used for base stabilization in paved roads are not subject to the strain levels that causes tensile failure in the geogrid. Therefore, the ultimate tensile strength of the geogrid was found to be a particularly poor indicator of the performance of a geogrid-stabilized base.

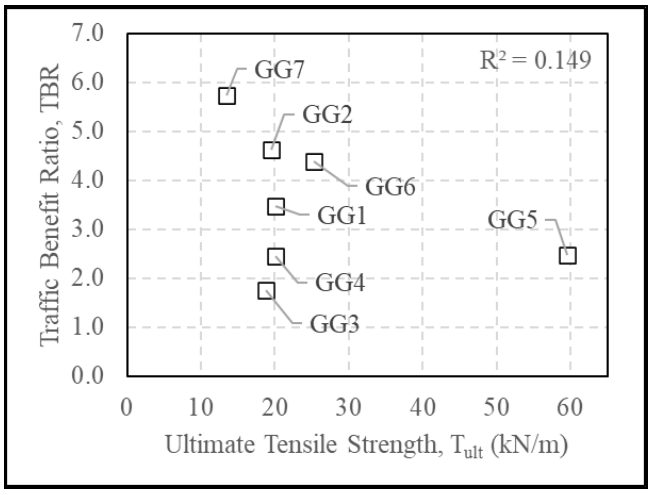

Figure 4.17. Correlation of traffic benefit ratio with the transverse ultimate tensile strength of the geogrids.

4.3.3 Interaction Properties

The interaction of a geogrid with the adjacent soil may be characterized by conducting Soil-Geosynthetic Interaction (SGI) tests, a novel variation on a conventional pull-out resistance test that involves the measurement of internal nodal displacements of the geosynthetic in addition to the external pull-out load and the corresponding frontal displacement of the geosynthetic (references). The procedure to conduct SGI tests resemble those of a conventional pull-out test, as described in ASTM D6706-01 (2021), but on a reduced-scale. Key differences the SGI test setup has over the conventional pull-out tests are: (1) the soil box of the SGI test has about 5% of the volume of a full-scale conventional pull-out test built to the minimum required dimensions (according to ASTM D6706-01), allowing for faster testing with multiple repeats; (2) The dimensions of the soil box and the geogrid specimen are such that it can be setup, vertically, in any standard load frames commonly used for multi-rib tensile tests of geogrids (ASTM D6637, 2015). Figure 4.18 shows the testing setup used to perform the SGI tests and Figure 4.19 shows a schematic cross-section of the test setup. The SGI tests are performed by sandwiching the geogrid within the soil, applying the desired confining pressure through the bladder on the lid of the box, and pulling out the geogrid from within the soil matrix. As in the conventional pull-out tests, the pull-out load applied and the frontal displacement of the geogrid are measured using a load cell and an LVDT, respectively. In addition to these measurements, the nodes of the geogrids are tied with tell-tale wires that run from the node of the geogrid, along the vertical ribs, to the bottom of the box where they exit the box to be tied to linear position transducers that measure the internal displacement of the geogrid nodes as the geogrid is being pulled-out from the top of the box. A typical layout of the geogrid node tie-ins is shown in Figure 4.20 (b).

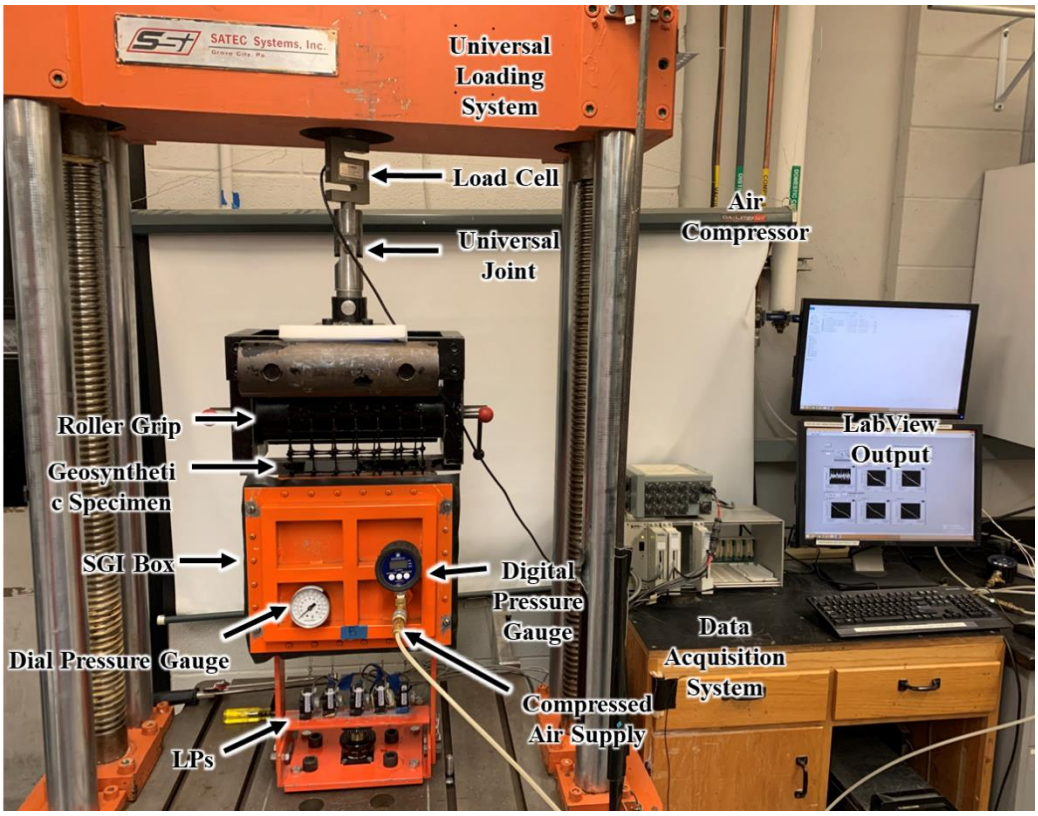

Figure 4.18. Soil-geosynthetic interaction test setup. (Peve, 2020)

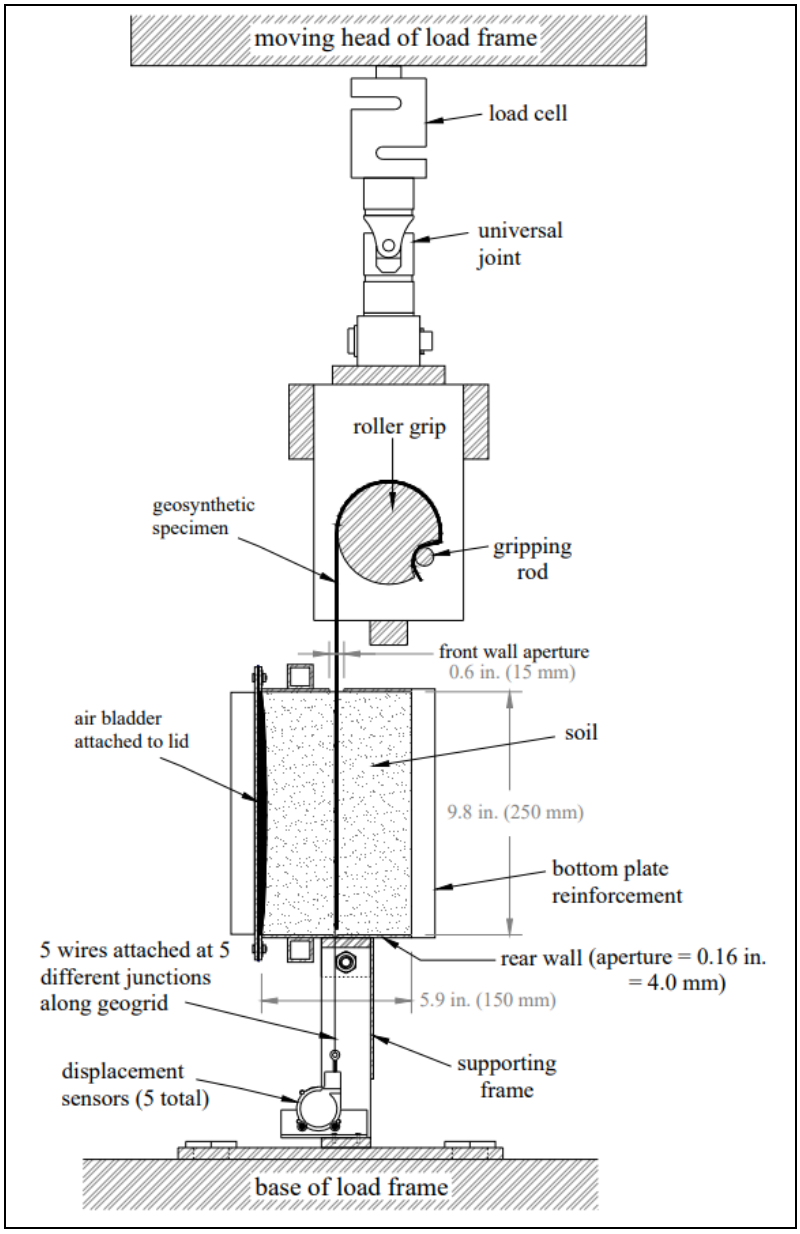

Figure 4.19. Schematic of the soil-geosynthetic interaction test. (Zornberg et al., 2013)

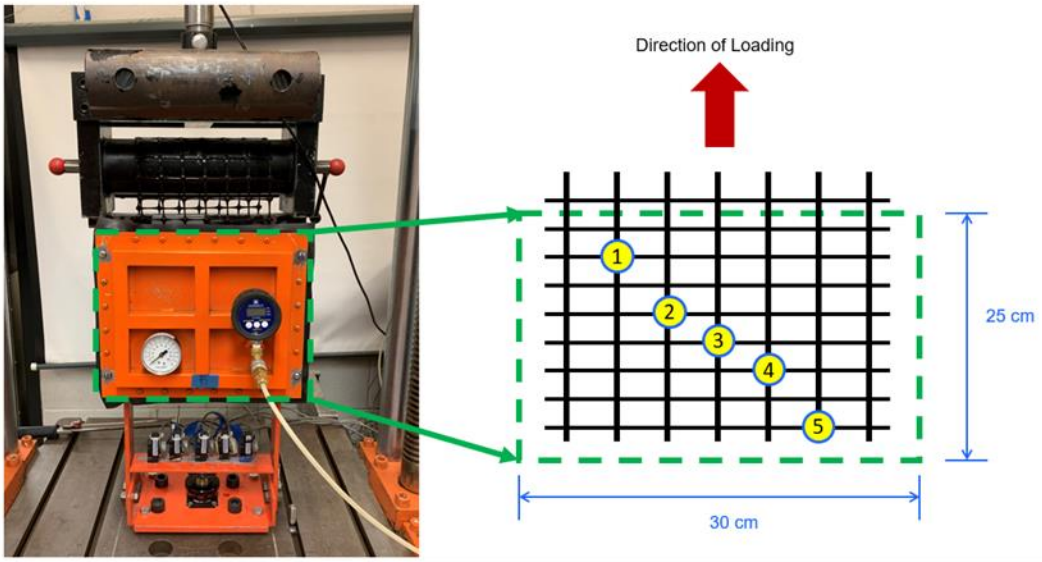

Figure 4.20. Geogrid nodal displacement measurement: (a) SGI test setup; (b) location of geogrid nodes tied to tell-tale wires. (Peve, 2020)

The SGI tests performed for this study involved sandwiching each geogrid (GG1 to GG7) within the clean gravel base material, conforming to the AASHTO #8 gradation at a confining pressure of 21 kPa. The geogrids were then pulled out from the soil-geogrid matrix while measuring their internal nodal displacements under the applied frontal unit tension. The frontal unit tension (T_0) and frontal frame displacement (u) are directly measured as shown in Figure 4.21, and the maximum pull-out resistance is obtained from the peak value of this plot. Note that the pull-out resistance obtained from the SGI test is different than that would be obtained in a conventional pull-out test owing to the shorter embedment length in the reduced-scale SGI box compared to the full-scale pull-out box. However, for the purposes of comparison of the pull-out resistances of the different geogrids (GG1 to GG7) against the AASHTO#8 gravel base, the modified pull-out resistance obtained from the SGI tests was deemed adequate.

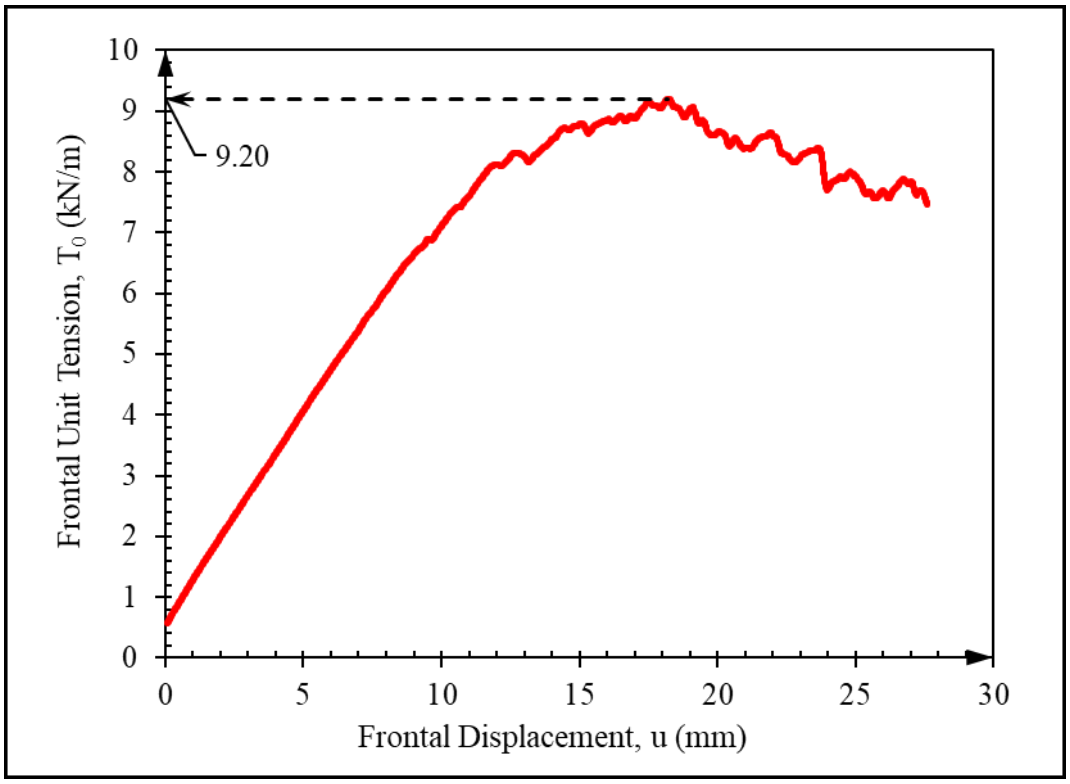

Figure 4.21. Frontal unit tension vs. frontal frame displacement.

Five specimens each for the different geogrids (GG1 to GG7) were used to perform the SGI tests and the pull-out resistances averaged from the five tests were averaged to obtain the average pull-out resistance of the geogrid against the grave base. This pull-out resistance was then compared to the TBR of the corresponding geogrid to assess the predictability of TBR from the pull-out resistance in Figure 4.22. The pull-out resistance is found to be poorly correlated to the performance of the geogrid in flexible pavements. Although the pull-out resistance is a measure of the confined properties of the geogrid in the gravel base, a condition very similar to the that which exists within the pavement structure, the magnitudes of sustained displacements across the geogrid at which the maximum pull-out force is mobilized is too high (around 20 mm). Whereas the

soil in the immediate vicinity of the geogrid undergoes displacements that are 3-4 times smaller in magnitude (Paper 2). This difference in displacement, and hence the strain levels, at which the TBR is mobilized in flexible pavements and at which the pull-out resistance is mobilized in SGI tests makes pull-out resistance a poor predictor of the performance of geogrid stabilized aggregate base. Further if the data set is corrected for geometric properties (GG2 and GG7 excluded for triangular apertures), the other five geogrids show a positive correlation (with slightly better R^2) indicating that the TBR increases with pull-out resistance.

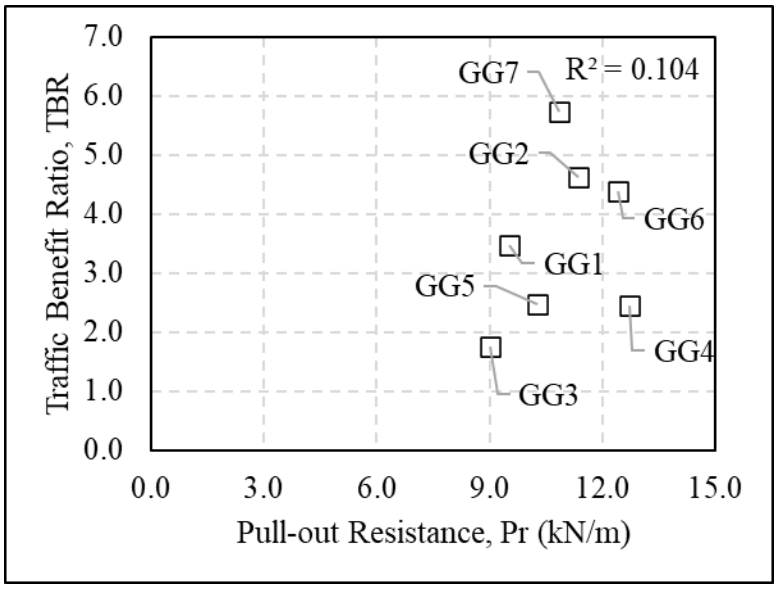

Figure 4.22. Correlation of traffic benefit ratio with pull-out resistance of the geogrid.

Thus, a measure of the geogrid's resistance to displacements under confined conditions (such as the pull-out resistance) but at smaller strains compatible with the displacement levels observed in flexible pavements (such as the tensile stiffness) is expected to be a better predictor of performance of stabilized aggregate base. The SGI test measures such a property called the coefficient of soil-geosynthetic composite, K_{SGC},

at small displacements and under confined conditions. In the SGI tests, the internal nodal displacements, u_i, of the geogrid are directly measured at the location of the tell-tale tie-ins, in addition to the measurement of the frontal unit tension, T_0 (Figure 4.23). The interface shear is progressively mobilized along the geogrid with the displacements initiating in LP1 (that is closest to the frontal pull-out load) and moving down the geogrid with subsequent LPs (2-5) being triggered in order.

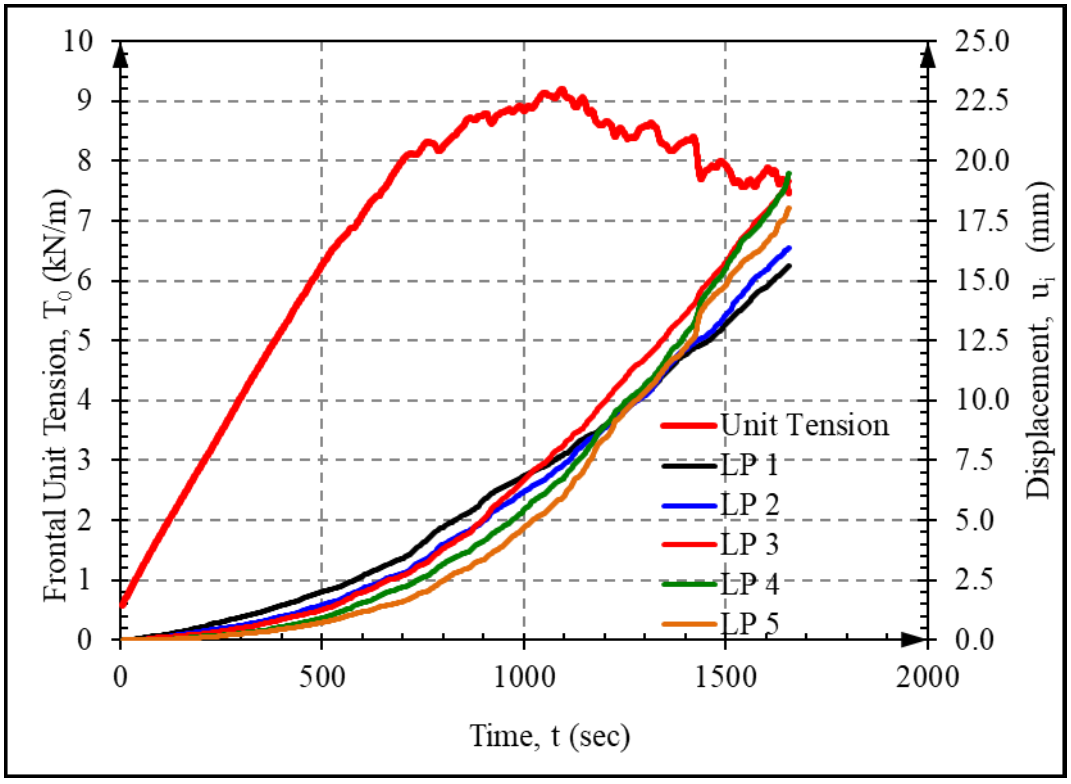

Figure 4.23. Frontal unit tension and internal nodal displacements with time.

Figure 4.24 shows the frontal unit tension plotted against the internal displacements of the LPs. The clear ordering of the triggering process of the LPs, with LP1 mobilizing at lower frontal unit tension, followed by LPs 2, 3, 4, and 5 which are subsequently triggered at higher unit tensions. The frontal unit tensions reach a state of

maximum constant tensile load corresponding to pull-out failure. All SGI tests conducted in this study were conducted up to pull-out failure.

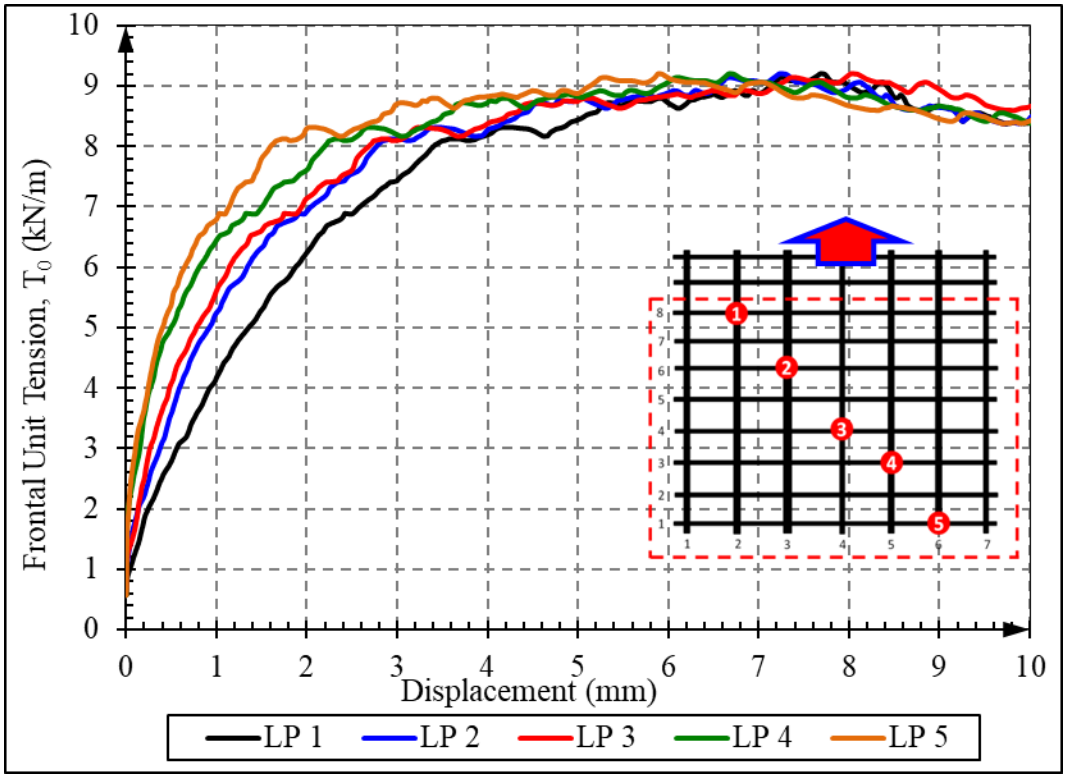

Figure 4.24. Frontal unit tension with internal nodal displacements.

The K_{SGC} model captures this behavior by assuming a rigid, perfectly plastic shear model for soil-geosynthetic interface and a linear-elastic model for the tensile load-geogrid strain behavior. As a consequence of this assumption, the domain of the geogrid length is divided into an active (region with triggered LPs) and a passive length (region with inactive LPs), where active length is that part of the soil-geosynthetic interface that is subject to the interface shear stress equal to yield shear strength (τ_y) resisting the pull-out force and the passive length contributes zero resistance to the pull-out force. Thus, any increase in frontal unit tension is balanced by an increase in active length equal to the

increase in pull-out unit tension divided by twice the yield shear strength (τ_y). The displacements in the passive length are assumed to be zero, while the displacement in the active length is determined from the strains along the active length. The tension at any point in the geogrid, from the point of application of the frontal unit tension to the end of active length, is estimated by determining the equilibrium of forces at that point (balancing the unit tension with the force due to the interface shear from that point to the end of the active length). The strains in the active region are then obtained from the estimated unit tension at any point and the linear tension-strain relationship. The closed form solution for the unit tension, T_i, at any point within the active length of the geogrid is given by (Zornberg et al., 2017):

$$T_i^2 = \left[4 \cdot J_c \cdot \tau_y\right] u_i \tag{4.9}$$

where u_i = displacement of the point, i.

J_C = confined stiffness i.e., slope of the linear unit-tension vs. strain relationship.

τ_y = yield shear strength at the rigid, perfectly plastic soil-geogrid interface.

The term $\left[4 \cdot J_c \cdot \tau_y\right]$ is defined as the coefficient of stiffness of the soil-geosynthetic composite, K_{SGC}, and is defined as the slope of the T_i^2 vs. u_i data immediately after the onset of displacements at location 'i' (i.e., at small displacements). Thus, in order to obtain the K_{SGC}, the unit tension at the tell-tale location when the displacements are triggered at the particular location must be estimated. The unit tension T_i at the location of tell-tale 'i' can be estimated by measuring frontal unit tension $T_{0,i}$ at the moment the LP at location 'i' is triggered (Zornberg et al., 2017). The unit tension at any location 'i' is estimated as the difference between the frontal unit tension T_0 at any

time, t, and the frontal unit tension $T_{0,i}$ at time t_i when the LP at location 'i' is first triggered. Thus, for each tell-tale location, the unit tension values are shifted by the unit tension value measured at the time the tell-tale location exceeds the triggering point ($T_i = T_0 - T_{0,i}$). The tell-tales are assumed to have been triggered when a displacement of 0.1 mm is reached at the tell-tale location. Figure 4.25 shows the unit tension at the tell-tale location, obtained through shifting the frontal unit tensions by the corresponding frontal unit tension at displacement initiation, plotted against the displacement of the nodes at the tell-tale locations. Excepting LPs 1 and 5, due to their proximity to the edges of the box and possible boundary effects, the other three LPs (2-4) show very similar response post-shifting, especially in the initial portion between 0.1 mm and 1 mm displacements. Thus, the behavior of the geogrid-soil interaction at small strains is in accordance with the K_{SGC} theory.

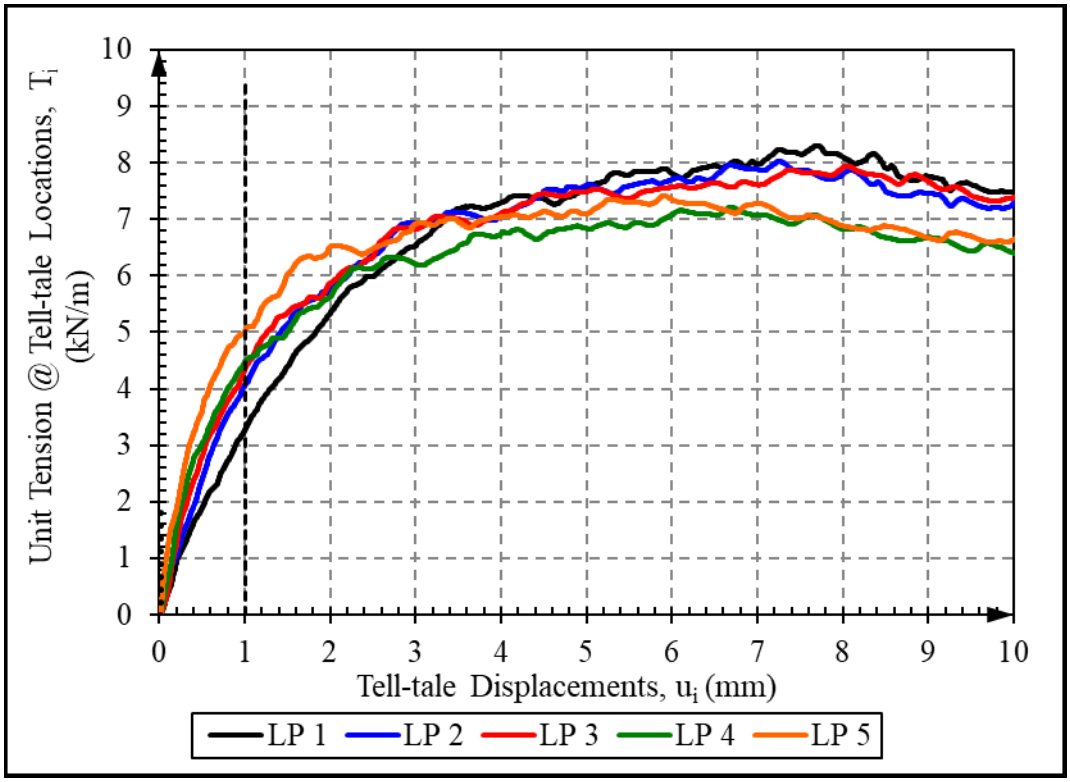

Figure 4.25. Unit tension at nodes with displacement of the nodes.

Figure 4.26 show shows the relationship between the unit tension squared and displacements at the location of tell-tales 2, 3, and 4. Since the K_{SGC} is a small-strain stiffness, only geosynthetic displacements ranging from 0.1 mm (trigger threshold) to 1.0 mm are used for the K_{SGC} calculation. The K_{SGC} is obtained using linear regression on the T^2 versus u data for each telltale location. The K_{SGC} provides a constitutive relationship between the displacement of the geogrid (u_i) and the resistive forces developed in it (T_i) by combining the shear strength (τ_y) of the interface with the stiffness of the geogrid under confined conditions (J_c). Therefore, K_{SGC} of the geogrid is a measure that combines the in-isolation stiffness of the geogrid under confined conditions with the interaction of the geogrid with the surrounding soil as shown in Equation (4.9). A high K_{SGC} indicates that the geosynthetic under consideration is not only stiff but is also capable of significant

stress transfer between the soil and the geosynthetic. This implies that K_{SGC} is particularly well suited in determining how well geosynthetics would perform under stabilization of bases where transfer of stresses from the soil to the geosynthetic is expected along with resistance to those transferred stresses (high stiffness).

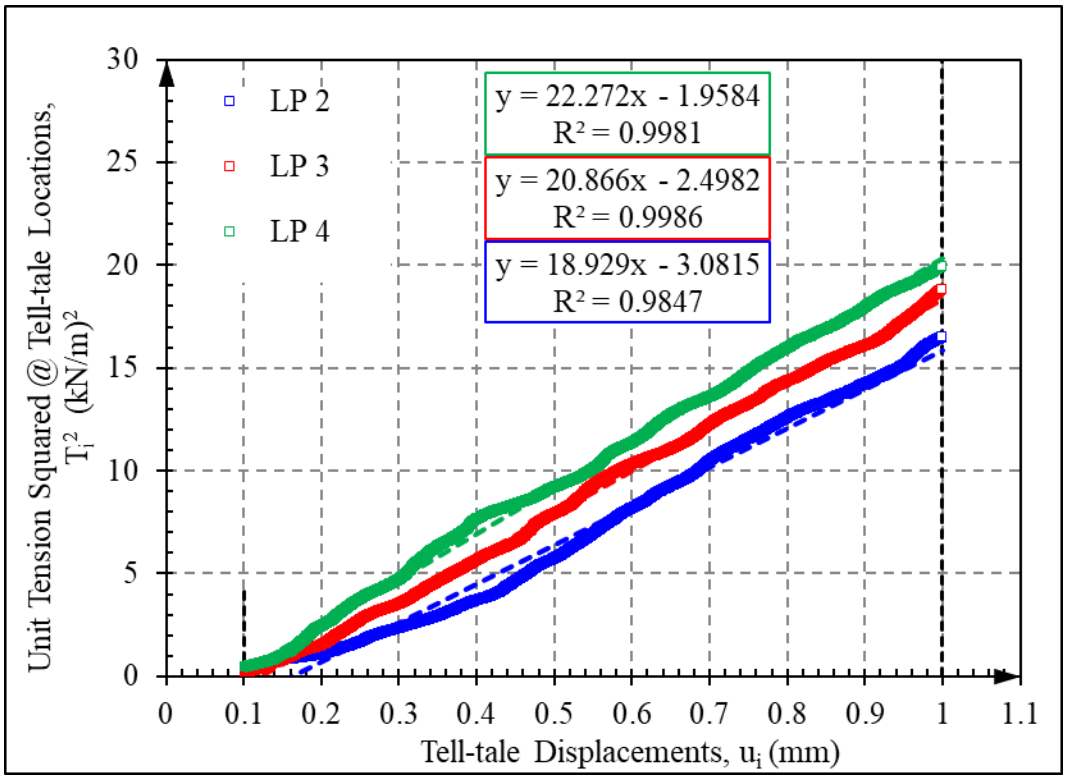

Figure 4.26. Determination of K_{SGC} as the slope of the T_i^2 vs. u_i curve in an SGI test.

A total of five SGI repeat tests were conducted in this study for each geogrid and three out of the five nodal displacements measured per test were used to compute the K_{SGC}. Thus, the K_{SGC} was calculated as the slope of the square of the unit tension (in (kN)/m) at each node versus the nodal displacement (in mm) of the corresponding node. The K_{SGC} of each geosynthetic was taken as the average of the 15 K_{SGC} values obtained from the five repeat tests. This K_{SGC} is compared with the TBR obtained from the

accelerated pavement tests conducted with same set of geogrids and aggregate base material in Figure 4.27. Each marker represents the (TBR, K_{SGC}) pair of the particular geogrid. The dashed line is the linear regression line through the datapoint. The results show that the TBR of stabilized sections are linearly correlated with the K_{SGC} of the aggregate base-geogrid composite used in the stabilized section. The high degree of linear correlation (R^2 = 0.998) between TBR and K_{SGC} values shows that K_{SGC} is a direct measure of the improvement to pavement rutting performance due to the inclusion of the geogrid and is thus a strong justification for the use of K_{SGC} as a critical parameter in the selection of geogrids to be used as for base stabilization.

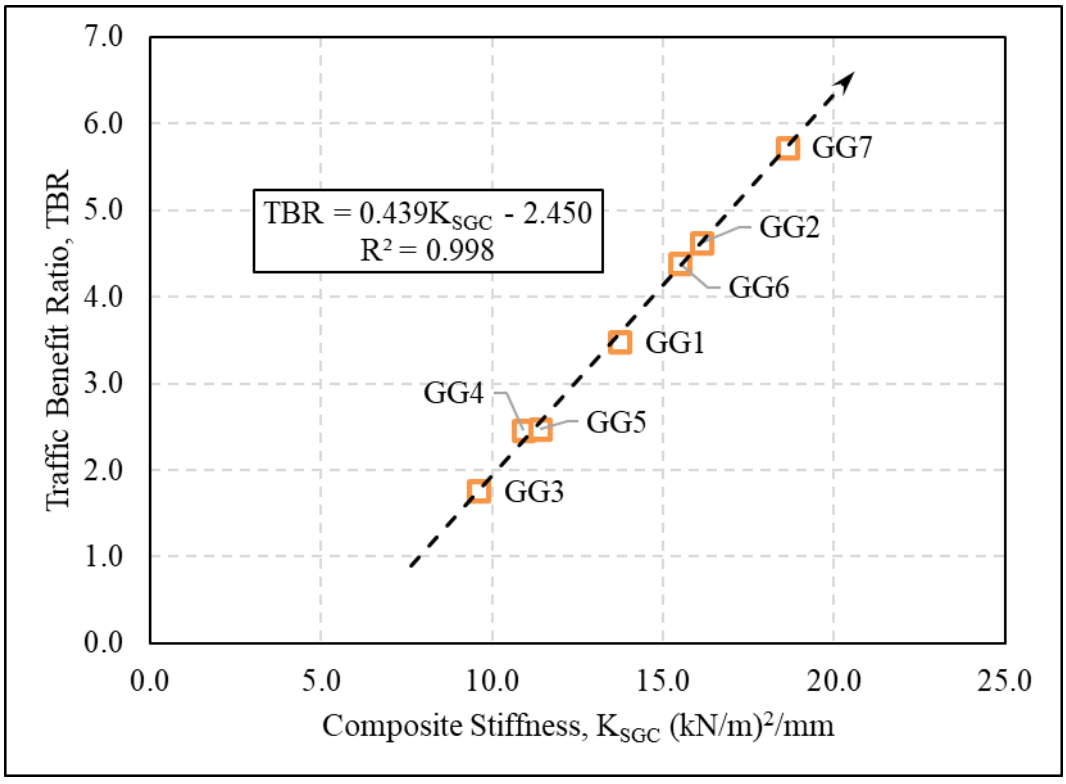

Figure 4.27. Correlation between TBR and K_{SGC} for the geosynthetic-stabilized pavement sections investigated in this study.

4.4 CONCLUSIONS

The benefits from the geogrid stabilization of the aggregate base in flexible pavement is assessed through an accelerated pavement testing program comprising of seven reduced-scale pavement sections with different type of geogrid and one section with no geogrid serving as the control. A model Mobile Load Simulator (MLS11) is used to apply repeated, uni-directional, rolling-wheel loads on to the reduced-scale pavement sections. The performance of the pavement sections is monitored through the measurement of the surface rut with increasing number of passes. The pavement surface rut is assessed from the surface rut profile obtained by measuring the pavement surface profile before and after trafficking using a laser profilometer developed in-house. In order to remove the uncertainties in the measurement of rut due to noise in the surface profile data from surface roughness and electrical noise, and to average out the asymmetry in heaves on either side of the wheel path, the surface rut profile is fit with a modified double gaussian function. The benefits from the stabilization of the aggregate base by geogrids are quantified as the improvement in pavement life against rutting, commonly referred to as the traffic benefit ratio (TBR). The TBR obtained from the accelerated pavement tests with the aggregate base stabilized by the various geogrids are studied for their correlation with the geometric and tensile properties of the geogrids in-isolation, and with their interaction properties with the aggregate base. Multi-rib tensile tests were conducted on the geogrids in order to determine their tensile stiffness and strength properties. The soil-geosynthetic interaction tests are conducted on the different geogrids with the aggregate base gravel used in this study to determine the pull-out resistance of the soil-geogrid interface and the coefficient of stiffness of the soil-geogrid composite.

- With increasing pavement rut, the shape of the surface profile remained a constant for a given pavement test section, and that only the magnitude of the rut (vertical

deformation under the wheel path and the heave on the sides) increases with increasing traffic volume.

- The shape of the surface rut profiles changes with the type of geogrid and the absence of the geogrid in the control section.
- The TBR computed for different failure rut criteria showed three distinct phases of the TBR curves. The first phase is associated with rut development through shakedown in both the stabilized and control sections and shows an increasing TBR as the geogrid reduced the level of shakedown in the stabilized sections. The second phase is associated with rut through shakedown in the control section, but transition to rut through lateral flow in the stabilized section, resulting in a sharp rise in TBR since rutting significantly slows down once shakedown stops. The final phase is characterized by a constant TBR, associated with lateral flow in both control and stabilized section, and the associated reduction in lateral flow in the geogrid stabilized section due to lateral restraint.
- For the seven different types of geogrid used in the study, the TBR associated with the stable third phase ranged from 1.8 to 5.8.
- Pavement sections with higher TBR are characterized by a narrower rut profile with a larger normalized heave adjacent to the wheel path.
- TBR showed poor correlation with the average aperture size of the geogrids, with significant scatter in TBR over a small aperture size range of 25-mm to 30-mm.
- The correlation between the TBR and tensile stiffness properties (unit tension at 2% and 5%) showed very poor R^2 values, when all seven geogrids are considered. However, when only geogrids with rectangular apertures are considered, the correlations improved, and TBR increased with increasing tensile stiffness. Thus,

small strain tensile stiffness was found to be a good measure of performance for geogrids with rectangular apertures.

- The correlation between TBR and ultimate tensile strength showed very poor correlation, with almost all geogrids having similar ultimate strengths with vastly different performances (TBRs). The poor correlation was attributed to the lack of overlap in the operational strain range in the base layer of a flexible pavement and that at which the ultimate tensile strength is measured.
- The pull-out resistance showed poor correlation with TBR when all the geogrids are considered but showed slightly better correlation when considering only rectangular geogrids. The pull-out resistance being measured at displacement levels that are significantly higher than those observed in the reduced-scale pavement sections result in poor correlation between the pull-out resistance and the performance in flexible pavements.
- The soil-geosynthetic composite stiffness (K_{SGC}), being a measure of the stiffness of the geogrid (slope of T^2 vs u) and being a combination of the yield shear strength and the confined small-strain tensile stiffness, showed an excellent correlation with the TBR observed in the stabilized flexible pavements.
- Thus, KSGC can be used to predict the performance of geogrid stabilized base layers in flexible pavements and therefore be used in the selection of geogrids for the application of stabilization.

REFERENCES

AASHTO M43-05, 2022. Standard Specification for Sizes of Aggregate for Road and Bridge Construction.

AASHTO R50, 2009. Standard Practice for Geosynthetic Reinforcement of the Aggregate Base Course of Flexible Pavement Structures.

Archer, S., Wayne, M., 2012. Relevancy of Material Properties in Predicting the Performance of Geogrid-Stabilized Roadways. GeoCongress 2012: State of the Art and Practice in Geotechnical Engineering 1320–1329.

ASTM D6637, 2015. Test Method for Determining Tensile Properties of Geogrids by the Single or Multi-Rib Tensile Method. https://doi.org/10.1520/D6637_D6637M-15

ASTM D6706-01, 2021. Test Method for Measuring Geosynthetic Pullout Resistance in Soil. https://doi.org/10.1520/D6706-01R21

Brown, S.F., Kwan, J., Thom, N.H., 2007. Identifying the key parameters that influence geogrid reinforcement of railway ballast. Geotextiles and Geomembranes 25, 326–335. https://doi.org/10.1016/j.geotexmem.2007.06.003

Christopher, B., Cuelho, E., Perkins, S., 2008. Development of geogrid junction strength requirements for reinforced roadway base design, in: Proceedings of GeoAmericas 2008 Conference, Cancun, Mexico. pp. 1003–1012.

Epps, A.L., Ahmed, T., Little, D.C., Hugo, F., 2001. Performance prediction with the MMLS3 at Westrack (Research Report No. FHWA/TX-01/2134-1). Texas Transportation Institute, College Station, TX.

Indraratna, B., Hussaini, S.K.K., Vinod, J.S., 2012. On the shear behavior of ballast-geosynthetic interfaces. Geotechnical Testing Journal 35.

Kim, H., Sokolov, K., Poulikakos, L.D., Partl, M.N., 2009. Fatigue Evaluation of Carbon FRP-Reinforced Porous Asphalt Composite System Using a Model Mobile Load Simulator.

Kim, S.-M., Hugo, F., Roesset, J.M., 1998. Small-Scale Accelerated Pavement Testing. J. Transp. Eng. 124, 6.

Kumar, T., Chehab, G.R., 2014. Methodology for Relating Accelerated Trafficking to Field Trafficking for Pavement Evaluation. KSCE Journal of Civil Engineering 18, 9.

Lee, Jusang, Kim, Y.R., Lee, Jaejun, 2015. Rutting performance evaluation of asphalt mix with different types of geosynthetics using MMLS3. International Journal of Pavement Engineering 16, 894–905. https://doi.org/10.1080/10298436.2014.972916

Martin, A.E., Walubita, L.F., Hugo, F., Bangera, N.U., 2003. Pavement Response and Rutting for Full-Scale and Scaled APT. J. Transp. Eng. 129, 11.

Peve, L., 2020. Sources of Variability in Small-scale Soil-geosynthetic Interaction Testing. The University of Texas at Austin.

Roodi, G.H., Zornberg, J.G., 2017. Stiffness of Soil-Geosynthetic Composite under Small Displacements. II: Experimental Evaluation. J. Geotech. Geoenviron. Eng. 143, 04017076. https://doi.org/10.1061/(ASCE)GT.1943-5606.0001769

Sakleshpur, V.A., Prezzi, M., Salgado, R., Siddiki, N.Z., Choi, Y.S., 2019. Large-scale direct shear testing of geogrid-reinforced aggregate base over weak subgrade. International Journal of Pavement Engineering 20, 649–658. https://doi.org/10.1080/10298436.2017.1321419

Smit, A. de F., Hugo, F., Epps, A., 1999. Report on the first Jacksboro MMLS tests (Research Report No. FHWA/TX-00/0-1814-2). Center for Transportation Research, Austin, TX.

Tang, X., Chehab, G.R., Palomino, A., 2008. Evaluation of geogrids for stabilising weak pavement subgrade. International Journal of Pavement Engineering 9, 413–429. https://doi.org/10.1080/10298430802279827

TxDOT DMS6240, 2017. Geogrid for Base/Embankment Reinforcement.

van de Ven, M., Smit, A. de F., 2000. The Role of the MMLS Devices in APT, in: South African Transport Conference. Presented at the Action in Transport for the New Millennium, p. 16.

Zornberg, J.G., 2017. Functions and Applications of Geosynthetics In Roadways. Procedia Engineering 189, 298–306. https://doi.org/10.1016/j.proeng.2017.05.048

Zornberg, J.G., Ferreira, J.A.Z., Roodi, G.H., 2013. Geosynthetic-Reinforced Unbound Base Courses: Quantification of the Reinforcement Benefits (Research Report No. FHWA/TX-13/5-4829-01-2), 5-4829-01. TxDOT, Austin, TX.

Zornberg, J.G., Roodi, G.H., Gupta, R., 2017. Stiffness of Soil–Geosynthetic Composite under Small Displacements: I. Model Development. J. Geotech. Geoenviron. Eng. 13.

Chapter 5: Summary of Conclusions

5.1 SUMMARY

The dissertation discusses an accelerated pavement testing (APT) program developed to evaluate the mechanisms associated with the stabilization of aggregate base in flexible pavements. The APT loading device used is the model mobile load simulator (MLS11) capable of applying repeated, unidirectional, rolling wheel loads, and the pavements tested are reduced-scale sections built in the laboratory under controlled environmental conditions (in terms of temperature and moisture). Three independent studies are conducted focusing on the development of the comprehensive instrumentation that monitored the performance of the reduced-scale pavement sections, the measurement of lateral restraint provided by the stabilization geogrid, and the identification of a mechanistically relevant parameter that serves as a good indicator of the performance of stabilized sections, respectively.

Chapter 2 outlined the development of the accelerated pavement testing facility for the purposes of this study. The design, development, construction, and operation of the 2D profilometer and the protocols associated with the data processing techniques to obtain the final surface profiles and pavement rut were crucial to the monitoring of the pavement performance. The novel particle tracking sensors were capable of tracking the horizontal particle displacements with the base. The earth pressure cells installed were found to be capable of measuring the dynamic stresses due to rolling wheel loads from the MLS11.

In Chapter 3, the instrumentation developed, in chapter 2, was used to monitor the pavement section performance for performing a repeatability study and a comparative study. The repeatability study assessed two control sections, identical in construction, for

variability in performance of the two sections assumed to be identical to each other, while the comparative study assessed the evolution of lateral restraint and consequent stabilization provided by the geogrid installed within the aggregate base.

In chapter 4, the primary focus was on understanding the surface rut profiles developed in pavement section with different types of geogrid, and their correlations to the geometric, material and interaction properties. Multiple testing programs such as the wide-width tensile tests for tensile properties and soil-geosynthetic interaction tests for interaction properties were performed to obtain the relevant properties for the correlation study performed.

Some of the key findings from the three studies conducted as a part of this dissertation are as follows.

1. The 2D Laser Profilometer developed to measure the surface profiles was found to be adequate to measure the surface deformation to an accuracy of ±0.25 mm. The vertical deformation under the wheel path, the location and magnitude of the heave, and thus the overall rut could be measured to an accuracy of ±0.5 mm.
2. The vertical deformation under the wheel path and the accompanying heaves on either side of the wheel path at every stage in the life of the pavement indicated that the lateral flow of base aggregates is the dominant mechanism of rutting, and that the one-dimensional compression of the aggregates was negligible.
3. The flexible particle tracking sensors developed were found to be capable of measuring the horizontal particle displacements within the base. The sensors demonstrated an upper limit for error due to vertical particle displacements at 10% of vertical deformation under the wheel path.
4. The particle displacement data was found to be consistent with expected behaviors and could be used to develop horizontal displacement field contour

plots. The particle displacement data demonstrated the lateral flow of aggregates in the base, with larger displacements near the surface and reduction in displacements with depth. The shear transfer efficiency plots also showed the increased lateral flow and slip close to the surface and greater shear transfer efficiency at the bottom of the aggregate layer.

5. The horizontal normal strain field, obtained as a partial derivative of the horizontal displacement field with respect to distance from the wheel path, showed the development distinct region of horizontal tension under the wheel and horizontal compression away from the wheel path. The regions of tension and compression from the strain field remained a constant with increasing traffic volume and were found to be compatible with the regions of vertical deformation under the wheel path and the that of the heaves adjacent to the wheel path remaining constant.
6. The earth pressure cells installed at various depths and at various distances from the wheel path captured the distribution of the load applied on the surface of the pavement. The regions of tensile strains were found to be compatible with the regions of maximum vertical stress under the wheel path. The stresses also decreased with depth under the wheel path due to the distribution of stresses over a wide area with increase in depth.
7. The comparison of performances between the two identical repeats of the control section showed that the pavement sections performed within 10% of each other in terms of rutting and particle displacements.
8. The comparison of the control and stabilized section showed a marked improvement in rutting pavement life (by 330%) in the stabilized section due to the inclusion of the geogrid. The rut profile in the stabilized section showed a

narrower rut path i.e., the location of the heaves was closer to the wheel path, and a taller heave adjacent to the wheel path compared to the control section for the same vertical deformation under the wheel path indicative of the redirection of the particle flow due to the inclusion of the geogrid.

9. The comparison of the displacement profiles between the stabilized and control section showed reduced in lateral movement of particles in the stabilized section compared to the control for the same traffic volumes. For the same level of vertical deformation under the wheel path, the lateral displacements in the stabilized section were higher above the geogrid, and lower in the vicinity of and below the geogrid compared to the control. This indicated the redirection of the lateral flow of the base aggregates due to the presence of the geogrid in the path of the aggregate flow. This caused more particle movement parallel to the geogrid orientation than perpendicular to it. The geogrid further resisting this lateral flow parallel to the geogrid resulted in the reduction of the particle movement in the vicinity of the geogrid. Finally, the shear transfer efficiency plot showed poor shear transfer across the location of the geogrid resulting in reduced particle movements below the geogrid location.
10. The rut profiles obtained from APTs on pavement sections with different geogrids showed that the shape of the rut profile is unique to the pavement configuration and does not change over the life of the pavement, whereas the magnitude of the deformations increase with traffic volume. Further, the higher the benefit (TBR) due to a geogrid, the narrower the rut path and with a more pronounced heave.
11. TBR showed poor correlations with aperture size, and ultimate tensile strength of the geogrid. TBR showed acceptable correlations with tensile stiffness and pull-

out resistance when accounted for geogrid aperture geometry and geogrid material properties, respectively.

12. TBR showed the best, highly-linear correlation with the small-strain confined stiffness measure of the soil-geogrid composite, K_{SGC}. This is due to the fact that both TBR in the APT and the K_{SGC} in the SGI tests are obtained under fairly similar conditions of confinement, and strain levels. Thus, K_{SGC} is the mechanistically relevant parameter for the selection of geogrids to be used in base stabilization.

5.2 FUTURE WORK

Having developed the techniques to assess the mechanical performance of the pavement and having established the repeatability of these protocols, the tools needed to evaluate the impact of a geogrid inclusion into the unbound aggregate layers of a flexible pavement has been used to answer two questions: (1) what happens to the particle movement within the base subject to lateral flow when a geogrid is present? (2) what property of the base aggregate or geogrid or the base aggregate-geogrid composite governs the extent of the impact of the geogrid on improving pavement performance? For a holistic understanding of the impact of the geogrid, future work should entail studying,

1. The effect of changing the base aggregate. The base aggregates used in this testing program was clean, rounded, uniformly graded material resulting in lateral flow dominant rutting mechanism. Alternate base materials could be (a) angular, uniformly graded material (b) well-graded clean gravel (c) well-graded soil with around 10% fine content and maximum aggregate size of 12 mm to simulate real base material.

2. The effect of changing the stiffness of the subgrade. The subgrade used in this study is a relatively stiff clean sand material. As observed in the post-trafficking trenching, the subgrade remained relatively unaffected across the tests. Since the subgrade was stiff and did not undergo any major deformation and the base material was placed at a relatively high density, lateral flow was the only feasible mechanism of rutting. Thus, repeating these tests with a less stiff subgrade such as a clayey silt whose stiffness can be easily altered by changing the moisture content would be useful.
3. The effect altering the depth of installation of the geogrid. All 8 stabilized sections tested had the geogrid installed at close to mid-depth within the base. This configuration resulted in increased lateral flow between the HMA layer and the geogrid location. Positioning the geogrid closer to the surface (at a shallower depth) could result in further squeezing of the path for lateral flow between the HMA and geogrid. This is likely to increase the TBR by restricting the width of the path through which lateral flow can occur. It will be interesting to determined what is the optimum location of the geogrid to maximum the benefits observed from stabilization.
4. Conducting large scale-SGI tests with artificial particles at increasing distances above and below the geogrid to evaluate the degree of interlock and the zone of influence for varying levels of confinement and angle of internal friction of the base aggregate (angular vs rounded aggregates).

Appendix 1: Literature Review

A comprehensive literature survey of geosynthetic-stabilized pavement systems and accelerated pavement testing was completed as a part of the research work discussed. The work outlined in the dissertation required the understanding of accelerated pavement testing methods, scaling down of pavements sections for controlled laboratory testing, index and interface properties of the geosynthetics (in-isolation and within the soil matrix) relevant to the stabilization of unbound bases, the mechanisms associated with the stabilization of soil with geogrids and the different types of sensors needed to assess the performance of a scaled-down stabilized pavement section trafficked using an accelerated vehicle simulator (such as MMLS3). The multi-disciplinary nature of the study needed a thorough literature review of the various fields involved to get an overall picture of where the current research stands, in the various fields. This allowed the for a comprehensive approach to ratifying the existing ideas, identifying the areas that need further research and developing a more integral solution to the problem. The literature review summarized in this appendix aided in learning and building up from the previous work in the various areas. The following objectives are met as part of the technical literature review for this project.

1. Collection, review, and assessment of relevant domestic and foreign literature on geosynthetic-stabilized pavement systems, with emphasis on the experimental, field validation and design components.
2. Analyses of the field performance data from geosynthetic-stabilized pavements and verification of any relevant proposed stabilization mechanisms.

3. Compilation of APT data from relevant non-stabilized and geosynthetic-stabilized pavement studies and identification of any relevant strategies to use APT programs to evaluate the performance of GRPs.
4. Identification of relevant results from the soil-geosynthetic interaction testing program.

A 1.1 GEOSYNTHETICS IN PAVEMENT SYSTEMS

There are different types of geosynthetics (geo-membranes, geo-cells, geo-nets, etc.) specializing in different functions (separation, filtration, drainage, etc.). One of the chief functions of geosynthetics is providing reinforcement. The geosynthetics that specialize in reinforcement are of three types namely, geogrids, geocells and geotextiles. Of these, the geosynthetics that are chiefly used for reinforcing unbound base course in pavement structures are geogrids. Geogrids constitute a category of geosynthetic materials made up of tension bearing elements that are meshed together to have an open grid-like appearance. The openings are sized to facilitate interlocking with the surrounding soil matrix, in addition to any frictional resistance between the geogrid and soil matrix (Figure A.1).

Figure A.1 Various types of Geogrids: (a) Homogenous; (b) Coated Yarn; (c) Welded;

Type of Geosynthetics for Stabilization

The wide spectrum of geosynthetic material available alongside the significant difference in their index properties and functions opens numerous combinations of geosynthetics embedded in the various unbound layers of the pavement structure. Watn et al. (2005) summarized the functions served by the various geosynthetic materials in the different unbound pavement layers as shown in Figure A.2.

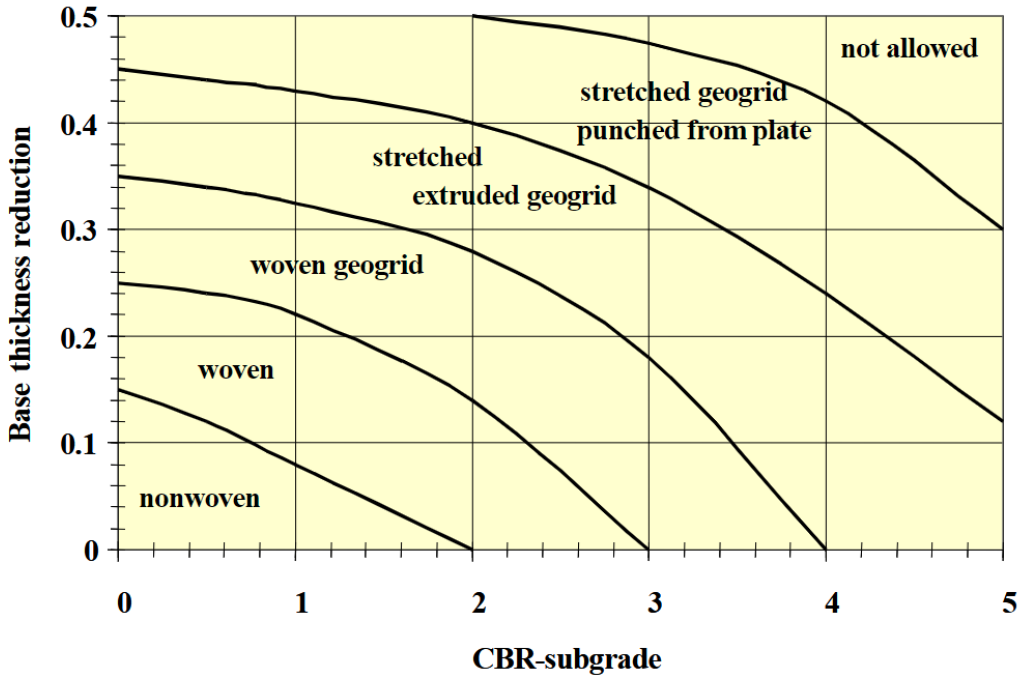

Figure A.2. Benefits of geosynthetics in unbound layers in terms of reduced base thickness (Watn et al., 2005)

The predominant candidate for the reinforcement of an unbound base layer in a pavement structure is polymer grid or geogrid. This notion is further reinforced by the fact that geogrids offer the maximum reduction in base thickness without compromise in performance for a pavement section. This is illustrated in Figure A.2 which shows the range of base thickness reduction for various geosynthetics as a function of the California Bearing Ratio of the Subgrade. It is seen that, for a given subgrade CBR, geogrids

provide better base thickness reduction than the geotextiles. Watn et al. (2005) also describe two case studies namely Test Road in Hitra, Norway and Test Trial in Germany. Their critical observation was that the mechanism of reinforcement and the aggregate-reinforcement interaction is not fully understood and that very few national standards recognize the benefits of designing with geosynthetic reinforcement showing a lack of understanding in the field.

Quantification of benefits from stabilization

One of the early design methods for geotextile-stabilized unpaved roads was developed by the US Army Corps of Engineers. This design procedure was validated and modified by Tingle and Webster (2003) to facilitate the use of the procedure with biaxial geogrids which were much stiffer than the geotextiles for which the method was originally developed. The bearing capacity factors developed for geotextile-stabilized base were validated using previously unpublished results from historical test sections. Further, for the geogrid-stabilized base, additional bearing-capacity factors were reported through the evaluation of the test sections. The test sections comprised of a subgrade of the high-plasticity (CH) Vicksburg Buckshot clay (CH), which was relatively immune to the influence of moisture content on the shear strength. Crushed limestone was used for the base-layer. The geosynthetic products (2 Geotextiles and 1 Geogrid) were placed directly on the subgrade to act as reinforcements in the subgrade-base layer interface. An M923 military truck, with a gross vehicle weight of 43500 lbs., was used to traffic the test sections. The calculated bearing capacity factors for the various sections studied are shown in Table A.1.

Test Section Item	Base Thickness in. (Design)	Effective Subgrade Bearing Capacity[1] CN_c, psi (Figure 3)	Average Subgrade Strength[2] CBR, % (Table 3)	Equivalent Shear Strength C, psi (Figure 4)	Calculated Bearing Capacity Factor[3] N_c
1	20	9.3	0.7	3.6	2.6
2	15	13	0.7	3.6	3.6
3	15	13	0.7	3.6	3.6
4	10	21	0.7	3.6	5.8

Table A.1. Calculation of subgrade bearing-capacity factor (Tingle and Webster, 2003)

Tingle and Jersey (2009) studied the performance of geosynthetic reinforced aggregate road sections. They constructed and trafficked eight instrumented full-scale aggregate road sections with marginal base materials over a typical subgrade. To quantify the benefits of reinforcement, the mechanistic response and permanent surface deformation of each test section was monitored periodically during trafficking and the traffic benefit ratios were calculated and tabulated in Table A.2. It was found that the mobilization of the geosynthetic reinforcement takes place only after the initial densification phase of the trafficking. Thus, the benefits of reinforcement were identified to be predominant after this phase and any difference in performance before this initial densification is mainly due to the aggregate gradation, packing, etc. The post densification results showed improved load response for the reinforced sections, compared to their unreinforced counterparts. It is noted that initial pavement stiffness should not be used to evaluate reinforcement effectiveness.

Performance Factor	Test Item	12-mm Deformation	25-mm Deformation	38-mm Deformation	50-mm Deformation	75-mm Deformation
Traffic benefit ratio	Item 1—crushed aggregate control	1	1	1	1	1
	Item 2—clay gravel control	1	1	1	1	1
	Item 3—crushed limestone control	1	1	1	1	1
	Item 4—crushed limestone w/GT	3	9	17	32	15+
	Item 5—crushed limestone w/GT-GG	3	217	169+	71+	15+
	Item 6—crushed limestone w/GG	2	98	161	71+	15+
	Item 7—clay gravel w/GG	0	1	1	1	1
	Item 8—crushed aggregate w/GG	2	8	18	29	27

Table A.2. Traffic benefit ratio comparisons (Tingle & Jersey 2009)

Relevance of Material Properties to Stabilization

The Texas Farm-to-Market Road No.2 or FM2 project (Zornberg et al., 2008) is one of the most relevant GRP fields studies in the US. The project located in Grimes County included the evaluation of the performance of 32 field test sections comprising control portions, three different types of geosynthetic reinforcements, sections with lime-treatment and multiple repeats of each section type. The data was collected over a period of nine years (January 2006 to January 2015). The results of the project were mainly used to assess the long-term performance of the various sections under the effects of environmental loads (e.g., longitudinal cracks). The geosynthetics used were geogrids GG PET, GG PP, and a geotextile GT. More details on the materials used are available in Report No. FHWA/TX-08/0-4829-1.

The authors found two main gaps in the current specification for geogrids in Texas. First, there was a lack of testing methods to directly evaluate the stabilization of unbound aggregates by the geogrids. Second, the lack of a property that is mechanistically relevant to the stabilization process. Further, they have also noted that while all the testing of geogrids is done under unconfined conditions, the application of those geogrids is under confined conditions. This makes the whole testing procedure more of a geosynthetic property, whereas the parameter of interest is the soil-

geosynthetic interaction property. The authors recommend the development of an index property based on confined monotonic tests for quantifying the confinement effect of the geosynthetic which is the principal effect of stabilizing geosynthetics in flexible pavements. The authors have hypothesized that the confined stiffness of the soil-geosynthetic system under low strains would be a relevant parameter to quantify the benefits of geosynthetics in pavement. To determine the confined stiffness of the soil-geosynthetic system, the authors had developed a new test setup called the soil-geosynthetic interaction (SGI) test.

The field test sections with the geogrids and geotextiles showed that the geosynthetics provided adequate stabilization over the high plasticity clays seen at FM2. Based on the laboratory and field studies, it was observed that the geosynthetics provided increased lateral confinement against aggregate movement in the unbound base of the pavement. The evaluation of benefits from reinforcement was done based on the confined stiffness of the reinforcement in the SGI test. It was found that the junction strength of the geogrids played a major role in determining the confined stiffness of the geogrids and eventually in the enhancement of performance of the pavement structure. Other factors that contributed to the differential performance of the geosynthetics were identified to be sensitivity to installation damage, high manufacturing variability and low friction coefficient.

Another major full-scale field section stabilized with geogrids is the Texas Farm-to-Market Road No. 1644 (Zornberg et al., 2013). The project included six experimental geogrid-reinforced and control sections treated with cement constructed in Robertson County. Geogrid was used to reinforce the two reinforced sections. The sections were constructed in 2010 and monitored data is available for 2 years. The results of the project were ratified by testing the same geogrid products in the soil-geosynthetic interaction

test. It was found that the performances of the stabilized field sections were consistent with the results of the bench-scale SGI tests conducted on the geosynthetics in the lab.

One of the significant findings of this study was the repeatability of soil-geosynthetic interaction test results along with the various sources of errors in the testing setup namely uneven torque on the clamping assembly, inconsistency in the tie wires for the extensometers, local changes in the density of the soil, variations in material properties of the geosynthetic and non-uniformity in the distribution of the confining pressure over the sample. Given considerable control over these factors, the authors were able to obtain repeatable results from the testing apparatus. 11 different types of geosynthetics (10 Geogrids and 1 Woven Geotextile) were tested against a standard soil and the results obtained were with an estimated error ranging from 10 to 20 % with a 95% confidence level.

Further comparison of the results across the various geosynthetic products reinforced the suggestion by Brown et al. (2007) that the product with the aperture width (W) to mean diameter of soil particles (D_{50}) ratio closest to the optimal value of 1.4 exhibited maximum confined stiffness values. At lower confining pressures, for geogrids with similar aperture size, the performance of the geogrids did not change with changes in the stiffness of the geogrids. However, the effect of increased stiffness improved the performance under higher confining pressures. The authors also noted that the performance of the geosynthetics in the conventional multi-rib tensile tests (unconfined) were poorly correlated to the stiffness measured from the soil-geosynthetic interaction tests. Thus, the performance in unconfined tensile tests do not provide a good measure of the performance under confined applications such as in pavement projects involving geosynthetic stabilization.

Concluding Remarks

Some of the key lessons learnt from the comprehensive literature survey relevant to geosynthetic reinforcements in full-scale field pavements systems are

- The use of geosynthetics to reinforce an unbound base layer in a pavement structure enhances the performance of pavements.
- The predominant candidate for the reinforcement of an unbound base layer in a pavement structure is polymer grid or geogrid.
- The benefits of reinforcing the unbound base layer of a pavement system are evident only after the initial densification phase, by which stage, the reinforcements are mobilized to influence the performance of the pavement. Thus, benefits from reinforcing a base layer must be quantified after this initial densification phase.
- The principal effect of reinforcing an unbound base layer using geogrids is an increase in lateral confinement of the base layer resulting in enhancement in mechanical properties such as modulus of the base layer, etc.
- Many DOTs and national standards do not feature a test for measuring the reinforcement function of the geogrids, instead the properties of the geogrid in-isolation are utilized.
- The in-isolation unconfined properties of the geosynthetics are poorly correlated to the benefits effected by using them as reinforcement in pavement structures.
- The confined stiffness of the geogrid which is a soil-geosynthetic interaction property was found to be a more appropriate parameter and it depended on the junction strength of the geogrids, sensitivity to installation damage, manufacturing variability and friction coefficient.

- The results of the field performance were found to be reasonably consistent with the experimental testing program using the soil-geosynthetic interaction test.
- The K_{SGC} coefficient, a parameter obtained from the soil-geosynthetic interaction tests, shows potential as an index in the selection of geosynthetics for use in base stabilization against environmental loads.
- Historically the placement of geosynthetics has been at the base-subgrade interface of pavement structure. However recent research challenges this idea by introducing a position dependent performance analysis.

A 1.2 ACCELERATED PAVEMENT TESTING

Accelerated Pavement Testing (APT) is defined as the controlled application of wheel loading in pavement structure for simulating the effects of long-term in-service loading conditions in a compressed time (Hugo and Martin, 2004). APT is one of the several different disciplines used in pavement engineering to understand the response of pavement structures and materials to traffic loading and the environment. One of the chief advantages of using APT programs is that they are cost effective, and they take a significantly less time when compared to the full-scale field sections. Long term pavement performance (LTPP) studies provide performance of real pavements under real traffic and climate conditions but are cost prohibitive, requiring many years of data collection and are often difficult to interpret given the very large number of factors influencing performance over time. APT done under controlled loading and environmental conditions provide a better understanding of the mechanisms influencing the performance of pavement.

Model Mobile Load Simulator (MMLS3)

Model Mobile Load Simulator (Figure A.3) is an APT device that is one-fourth scale of a full-scale APT device. A scaled-down version of the load simulator cuts down costs in terms of equipment, construction of pavement section and operation. It also facilitates testing on a laboratory scale under controlled environment and testing conditions. The use of scaled APT is becoming increasingly popular with as many as 21 MMLS devises in operation by DOTs and research organizations worldwide. Two aspects are critical in the evaluation of MMLS tests: (1) the use of reduced-scale testing of pavement sections are particularly useful when the goal is to obtain a preliminary indicator or ranking of performance; (2) to carry out scaled tests effectively, dimensional analysis considerations need to be met, i.e., laws of similitude must be observed. This essentially ensures that the full-scale and scaled-down pavement sections are subjected to the similar stresses and strains under scaled-down loading and similar environmental conditions, with the material properties being equivalent to full-scale materials. Figure A.4 shows the schematic of the MMLS3 one-fourth scale APT device. Table A.3 summarizes the specifications of the MMLS3

Figure A.3. UT's MMLS in the field

Relevant Literature on APT

A large volume of knowledge exists globally in the field of full-scale APT that has been systematically and concisely synthesized in three syntheses by Hugo and Martin (2004), Metcalf (1996), Steyn (2012) spanning the work done in this field over the last 40 years. Metcalf (1996) noted that there were 35 full-scale APT devices in the world, of which 19 of them were active. Since then, there has been a significant increase in the number of full-scale APT devices in the US and around the world. Steyn (2012) reported that full-scale APT has been predominantly used in studies to determine equivalence between a conventional solution (with materials whose properties are known) and a novel solution (with new and innovative materials whose behavior is unknown). The established equivalence of the novel solution is extrapolated for immediate use in the field, where the newer materials continue to be monitored for the understanding of material behavior and pavement performance.

When scaled models are used, caution must be addressed to the level of load on the pavement. The stresses must be determined by the laws of similitude and corresponding wheel load and tire inflation pressure must be determined so that the stresses applied are representative. Alabaster et al., (2004a, 2004b) demonstrated that vertical surface deformation or rutting follow a power law as function of the applied stress with exponents varying from 2 to 9, depending on the pavement type and end of pavement life definition.

Similarly, tire inflation pressure determines the shape of the contact area between the tire and the surface layer. Since the contact area does not have a uniform stress distribution, this in-turn determines the maximum vertical and shear stresses applied onto the surface under the determined loading. Several researchers (De Beer et al., 2004; Machemehl et al., 2005; Machemehl and Wang, 2006; Prozzi and Luo, 2005; Wang and

Machemehl, 2006) have found that this is directly related to the tensile stresses at the bottom of the surface layer and thereby having a direct effect on the performance of the pavement structure.

No. of bogies	4	
No. of axles per bogie	1	
Wheels per axle	1	
Wheel diameter	300	mm
Tire width	80	mm
Lateral spread of tracks from centerline	0 to 80	mm
Maximum tracking width	240	mm
Tire footprint area	34	cm^2
Tire contact pressure	560-800	kPa
Nominal load per wheel	1900-2700	N
Load setting	Load cell calibration	
Load control	Automatic	
Nominal speed	2.5	m/s
Nominal wheel load application per hour	7200	
Nominal motor supply voltage	220 V AC single phase	
Power consumption	1500	Watt (max)
Dimensions:		
Length	2400	mm
Width	600	mm
Height	1150	mm
Weight	800	kg

Table A.3. Technical specification of the MMLS3 as provided by the manufacturer.

Wheel wander was observed to produce reduced levels of rutting in the pavement in case of unidirectional loading such as in case of MMLS3. Significant stresses are developed both on the pavement surface and on the wheel. Hence consistency in the use of wheel wandering across the different test sections is advised to facilitate unbiased comparison of section performances.

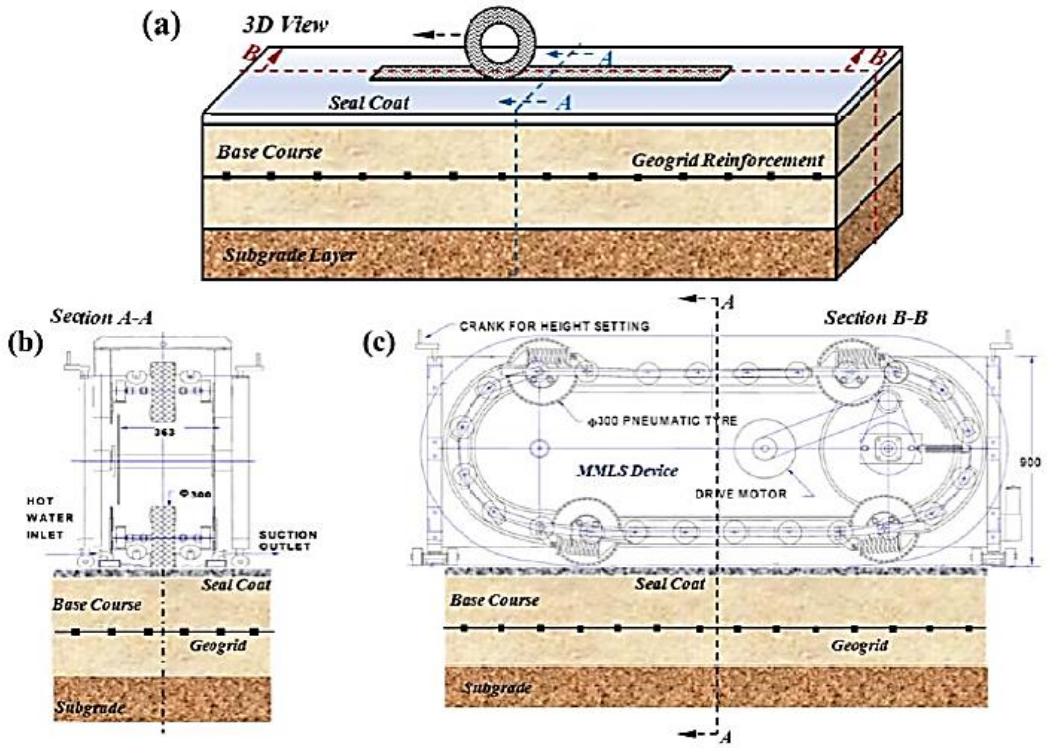

Figure A.4. Pavement in APT program: (a) schematic view; (b) cross-section; (c) longitudinal section.

Smit et al., (1999) outlined three accelerated pavement tests completed on US 281 in Jacksboro, Texas using the one-third scale Model Mobile Load Simulator (MMLS3). The MMLS3 testing was used to investigate and compare the relative rutting of the one-third scale MMLS3 against that of the full-scale TxMLS. Figure A.5 shows the

comparison between the rutting performance under MMLS3 and TxMLS loading. Figure A.6 shows the relationship between the rut depths. The ratio of the rate of rut development in the TxMLS relative to that in the MMLS3 was low (2.9) under lower traffic volume and with increase in traffic volume this ratio increased to a value of 12.6. The authors attribute this delayed increase in rutting rate to the larger influence depth of the TxMLS due to its increased contact area and higher loads resulting in the 1D densification and lateral flow of the asphalt concrete at higher depths. Note that MMLS3 is a one-third scale APT device and the laws of similitude as discussed earlier are not followed in this study. This results in extraneous rutting as reinforced by the observations of Alabaster et al., (2004a, 2004b) discussed earlier.

The authors also give an alternative explanation for stark difference in performance under the two mechanisms. They attribute the cause of the difference to the configuration of the wheel. While MMLS3 uses a single wheel load, TxMLS uses a dual wheel configuration. This distinctly affects the stress distribution beyond the point superposition of the stresses from the two wheels as illustrated in Figure A.7.

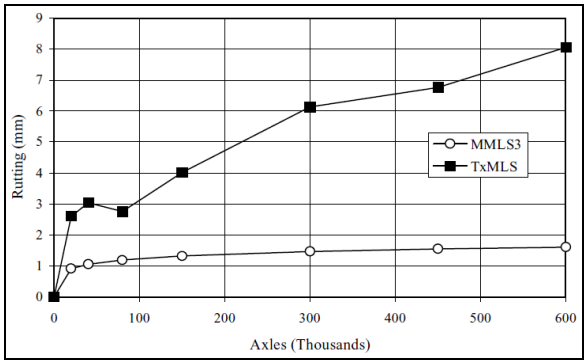

Figure A.5 . TxMLS vs. MMLS3 rutting (Smit et al., 1999).

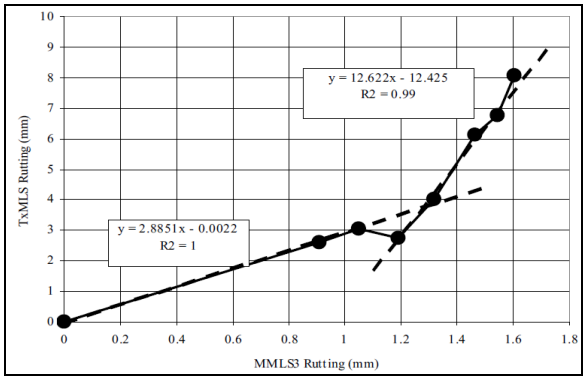

Figure A.6 . Relationship between TxMLS and MMLS3 rutting (Smit et al., 1999).

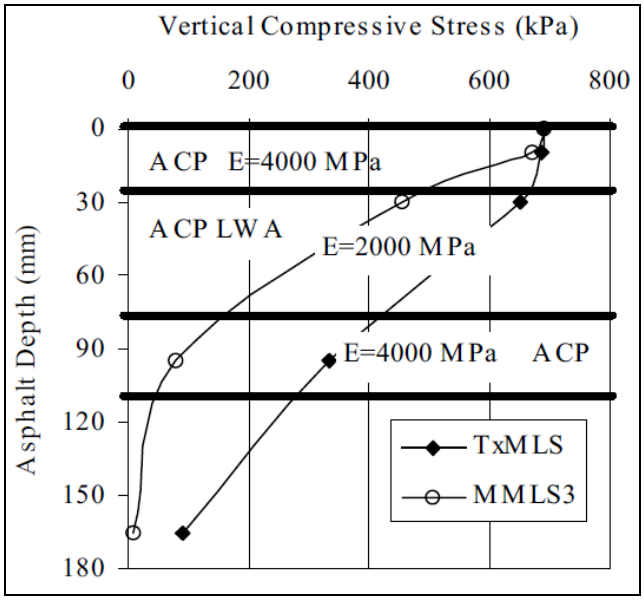

Figure A.7 . Model tests in the field for composite layered structure (Smit et al., 1999).

The authors observed that the development of rut under the TxMLS followed three different mechanisms namely, 1D densification, viscous flow, and lateral flow (plastic flow). The road, under the MMLS3, also exhibited the viscous flow mechanism of rut development, although magnitude of stresses caused a differential rutting

performance. Thus, the scale of loads applied to pavements determines the mechanisms of rutting activated in the pavement system.

Epps et al., (2001) conducted five MMLS3 tests on four pavement sections at WesTrack to establish a relationship between the existing field performance, material properties and MMLS3 test results. The authors compared the performances observed in the laboratory tests with the MMLS to the measured field performance under full-scale loading. The researchers found a very good correlation between the rutting results of the MMLS3 tests and those observed in the field for the four independently trafficked sections. The authors recommend the standardization of the rutting depth analysis method to ensure uniformity. The method favored by the author was the Reference Method, where the pavement surface was profiled relative to a fixed reference. A performance prediction methodology to predict rutting in the field under full-scale trafficking by performing MMLS3 tests in laboratory was reported. An analytical stress analysis using layered elastic analysis was presented to account for additional factors such as lateral wander effects, tire contact stresses, future traffic, prevailing environmental conditions, and material properties that could affect the performance of the asphalt.

Smit et al., (2003) performed one-third scale, dry & wet-heated model mobile load simulator testing on five sections at the National Center for Asphalt Technology Test Track. They compared the rutting performance of the sections under the MMLS3 with that under full-scale truck loading. Cores were extracted from the sections, both under and outside the wheel path and laboratory tests such as wet and dry Hamburg wheel testing, Superpave shear tester frequency sweep and semi-circular bending strength testing were performed.

Table A.4 shows the NCAT track sections tested using the MMLS3. No lateral wandering of the wheel was applied during testing. In addition to the tests listed in the

testing matrix, several cores were obtained and tested using the wet Hamburg and semi-circular bend tests.

Test No.	Date	NCAT Section	Dry/ Wet	Axles, k	Total Rut, mm	Down Rut, mm
1	03/04/2002	S9	Dry	44	2.2	1.4
2	03/11/2002	S10	Dry	109	3.4	2.2
3	03/18/2002	E2	Dry	112	4.1	3.1
4	03/25/2002	S9	Dry	94	2.7	2.0
5	04/02/2002	E6	Wet	85	3.0	1.9
6	04/15/2002	E2	Dry	107	3.4	2.7
7	04/15/2002	E2	Wet	103	3.8	2.9
8	04/22/2002	E8	Dry	106	4.6	3.5
9	04/22/2002	E8	Wet	106	4.0	2.9

Table A.4 . MMLS3 test matrix and rutting Results (Smit et al., 2003).

Table A.5 the results and ranking of the various test sections subject to laboratory and field tests. The results indicated that the ranking of the sections remained consistent independent of the testing method between the full-scale rutting performance of the truck sections and compared to the MMLS3 sections. As far as the results from the laboratory tests are concerned, they do not agree with full or one-third scale wheel loading methods. The procedure to predict the performance of a section under full-scale loading from the performance under MMLS3 loading was developed by Epps et al., (2001). This procedure was used in the current study and the results of the comparative analysis were presented. The authors found that the rutting prediction ratio, PR was approximately equal to 1 for most sections (except E2 and E8). The authors indicated that estimation of full-scale loading rut depth from MMLS3 loading rut depth may lead to overestimation. However, they recommended this area must be further examined before any conclusions can be drawn from the same. The authors developed a method to predict the rut under the

full-scale loading from the rut under MMLS3 loading, the associated differences in the vertical compression stress potentials, and the influence factors. It was observed that factors such as the volume of traffic, lateral wander, frequency of traffic loading and temperature of the HMA layers were the primary factors influencing the comparison.

Rank	Trucks[1]	APA (NCAT)[2]	Hamburg (NCAT)[2]	Hamburg (TxDOT)[3]	MMLS3[4]
1	S9 (2.7 mm)	S9 (2.2 mm)	E6 (2.7 mm)	E2 (3.2 mm)	S9 (2.7 mm)
2	E6 (4.0 mm)	E6 (2.3 mm)	E2 (2.8 mm)	S9 (3.8 mm)	E6 (3.0 mm)
3	E8 (4.0 mm)	E2 (2.3 mm)	E8 (3.0 mm)	E6 (4.0 mm)	S10 (3.2 mm)
4	S10 (4.1 mm)	S10 (2.6 mm)	S10 (3.5 mm)	S10 (4.2 mm)	E2 (3.8 mm)
5	E2 (5.1 mm)	E8 (4.6 mm)	S9 (3.7 mm)	E8 (4.6 mm)	E8 (4.0 mm)

[1] Dipstick rutting after 8.5 million ESALs
[2] Dry at 64°C after application of 8,000 cycles
[3] Wet at 50°C after application of 20,000 cycles
[4] Total rutting at 100,000 axles (interpolated/extrapolated)

Table A.5. Ranking of mix rutting performance based on laboratory and field tests (Epps et al., 2001).

Concluding Remarks

Some of the key lessons learnt from the comprehensive literature survey of those literatures relevant to Accelerated Pavement Testing of pavements systems are as follows.

- The use of scaled-APT programs warrants attention to considerations of dimensional analysis i.e., laws of similitude. However, scaling of materials is not required if the dimensions of the materials do not influence the structural response in terms of compaction, densification under traffic, etc.
- APT programs are more commonly used in case of studies that involve comparison between two or more sections with different materials or configurations with all other parameters remaining constant. APT has the

advantage of allowing the operator to control all the parameters with respect to the testing. Thus, APT programs are predominantly used to demonstrate equivalency of sections.

- Scaling of the loads between full-scale and reduced-scale sections becomes mandatory when rutting performance of the pavement sections are considered, as the rutting depths correlate exponentially with the applied stress levels. This is in-turn increases the estimated error in the analysis, even in the case of comparison studies.
- Improper scaling of loads results in variable relative rates of rutting across the various test sections thus introducing an error in the comparison of the relevant data.
- Improper scaling of loads results in activation of different or unexpected mechanisms of rutting. Hence caution must be exercised to ensure that the loads are scaled in accordance with the laws of similitude.
- Variation in the tire inflation pressure affects the contact area and maximum vertical and shear stresses that come on the contact surface. This is found to be directly related to the tensile stresses at the bottom of the surface layer. Hence caution must be exercised to ensure that the tire inflation pressure is set to the manufacturer recommended value to obtain the desired contact area.
- Wheel wander affects the level of rutting significantly. Hence care must be taken to ensure that the wheel wander is accounted for uniformly across the various test sections.
- Rutting depth measured with respect to an initial non-trafficked profile is more reliable.

- Prediction of rutting performance under full-scale loading from that under reduced scale may lead to overestimation.
- Laboratory torture tests such as the Hamburg wheel tests have poor predictability both qualitatively (ranking) and quantitatively.

A 1.3 INSTRUMENTATION

Understanding the mechanisms involved in reinforcements of unbound bases requires extensive data collected from highly instrumented sections subject to trafficking. Some of the common parameters that are to be measured to develop a mechanistic-empirical pavement design model, include strains, stresses, deflections, moisture, and temperature (Weinmann et al., 2004). In situ measurements during full-scale APT allow for the development of accurate performance models and the calibration of mechanistic pavement design approaches (Steyn, 2012).

Instrumentation of full-scale field section

Sargand et al., (1997) identified the most important parameters or material properties required to develop and validate a numerical model such as FEM, FDM, BEM of the pavement design which is essential for developing an empirical mechanistic design method. They identified two sets of input parameters for these models. The first set consisted of material properties of the various layers in the pavement system, namely the stiffness, Poisson's ratio, strength, and nature of the failure limits (brittle or ductile). The second set consisted of parameters that would be needed to calibrate such a model such as pressure between the layers, deflection of the layers, strain in the pavement, joint discontinuities, temperature distribution, etc. Since then, any attempt at developing an

empirical mechanistic model has involved instrumentation of test sections to determine these parameters.

Brandon et al., (1996) discussed the construction and instrumentation of geosynthetic reinforced secondary road test sections in Southeast Virginia. The test road consisted of nine instrumented, control and geosynthetic reinforced test sections of varying base and surface HMA layer thicknesses. The geosynthetics used were a geogrid and a geotextile which had been characterized by Smith et al., (1995).

Two types of Earth Pressure Cells (EPCs) were used in the study, namely the hydraulic pressure type Carlson TP 101 and the diaphragm type Kullite Type 0234. They were used to measure dynamic traffic loading. It was found that maximum registration ratio was observed when the EPCs were flush with the surface of the respective soil layer. This ensured minimum disturbance between the subsequent layers. The EPCs were placed at mid-depth of the base layer and at the base-subgrade interface. Carlson JO-1 Soil Horizontal Strain Gauge was used to measure strain in the soil layers and near the base-subgrade interface just below the EPCs. Kyowa KM HMA Horizontal Strain Gauge was used to measure the strains at the bottom of the HMA wearing surface layer. Measurements Group N2A 06 40 CBY 120 Foil type strain gauge was used to measure the strains at the bottom of the geotextile. The strains at the bottom of the geogrid were measured using foil-type strain gauges from Texas Measurements. Further, T Type thermocouple for temperature sensing, Gypsum Block Moisture sensor and piezometric polymer traffic sensor were used in the study. Table A.6 summarizes the survivability of the various instrumentation after 8 months of installation.

Gage Type	Number Installed	Number Survived	Percent Survived
Kulite earth pressure cells	6	3	50%
Carlson earth pressure cells	21	16	76%
HMA strain gages	35	26	74%
Geotextile strain gages	18	1	6%
Geogrid strain gages	18	5	28%
Soil strain gages	6	5	83%
Thermocouples	17	15	88%
Gypsum blocks	18	18	100%

Table A.6. Instrument Survivability after 8 Months (Brandon et al., 1996).

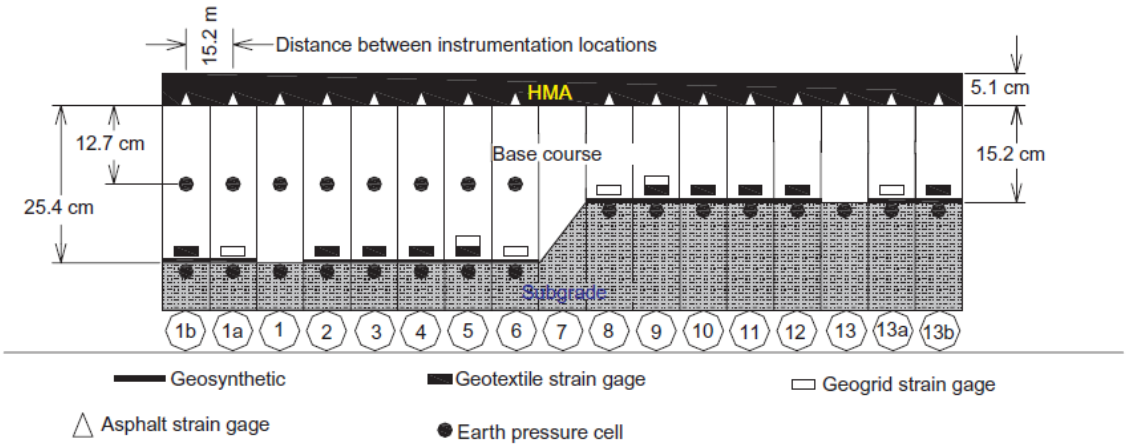

Figure A.8. Profile View of the test sections (Warren and Howard, 2007).

The authors also conducted a gauge survivability analysis by determining the percentage of sensors still active in the sections, 8 months after construction and traffic. They also observed that the critical period for gauge survivability is during construction and the failure rate of sensors beyond the very first month of trafficking is very low. Thus, to ensure maximum functionality of the gauges, care must be exercised primarily during the construction phase of the project.

One of the pioneering works done, in terms of instrumentation of a full-scale field pavement section is the project that was part of a research initiative conducted by the Arkansas State Highway and Transportation Department (Warren and Howard, 2007). The project involved the construction of 17 highly instrumented sections (Figure A.8) of full-scale geosynthetic reinforced flexible pavement at Marked Tree, Northeast Arkansas. In this study, the base-subgrade interface was stabilized with 2 different geogrids, 3 different woven geotextiles, and 1 nonwoven geotextile. The project was aimed at determining the benefits of geosynthetic-stabilization of unbound layers by measuring the dynamic pavement response under traffic loads. The responses measured was used to aid the development of a mechanistic-empirical design procedure for geosynthetic-stabilized flexible pavements. Details and recommendations for the use of sensors in full-scale projects were also reported and are as follows.

Geokon 3500 hydraulic earth pressure cells were used to measure the vertical stresses in the soil. The earth pressure cells were installed in the subgrade, approximately 2 cm form the subgrade surface and mid-depth (sections 1-6) in the 25.4 cm thick base coarse layer. The idea behind the position of the earth pressure cells was that those cells positioned at the surface of the subgrade would measure any relief in stress at the subgrade level because of the geosynthetic and those cells positioned at mid-depth in the base course would measure the stress distribution within the aggregate mix thus evaluating the confining effect from the geosynthetic. The instrumentation was in the outside wheel path in the center of each test section (longitudinally). Vishay Micro-Measurement foil strain gauges were utilized to measure strain on the geosynthetics. EP-08-19CDZ-350 was utilized for the geotextiles (48.3 mm in length), EP-08-500GC-350 (12.7 mm long) for the polyester geogrid and EP-08-230DS-120 (5.8 mm long) for the biaxial polypropylene geogrid. CTL Group ASG-152, H-type Asphalt Strain Gauge is

embedded at the bottom of the asphalt surface layer. Omega TMQSS-125G-6 T-type thermocouples (rated 220^{o} C) were placed in the base course and subgrade layers to create a temperature profile. Three T-type thermocouples were placed at the bottom of the asphalt-concrete layer, since the surface layer was only 5.1 cm thick. For this purpose, the Omega CPSS-14G-12-NHX T-type thermocouples (rated 650^{o} C) were used. Decagon EC-20 capacitance type moisture content probe was used to measure moisture content variation in this study. Geokon 3400 piezometers were installed outside the wheel paths in section 7 to monitor the existence of static pore pressures at the surface of the subgrade and mid-depth in the base course.

All 17 active earth pressure cells installed in the subgrade and all eight earth pressure cells in the base course showed signal presence and stability upon pre-traffic evaluation. All 17 active asphalt strain gauges installed were found to be working satisfactorily. Out of the 16 active geosynthetic gauges, 3 gauges malfunctioned thus showing an 81 % survivability rate, post-construction, for geosynthetic foil type strain gauges. In summary, out of the 56 active structural gauges, 94 % provided functional signal post-construction. Of the 11 thermocouples installed, five were not satisfactory. All five moisture content probes and both piezometers were satisfactory. Approximately 77 % of the active environmental sensors provided functional signal post-construction. The authors finally produced some installation recommendations for the sensor. They recommended that the gauges must be oriented in a direction that will maximize gauge survivability. This means, for pavement structures, the gauges aligned horizontal (perpendicular to applied load) survived better than those aligned vertical. Wherever possible, backup gauges must be installed to reinforce the instrumentation configuration. The functionality of the gauges and the quality of the signal were to be checked before the burying of cable lines in the conduit system. This facilitated repairs and ensured near

100% functionality before trafficking. The authors recommended the calibration of all sensors (or at least validation of the calibration factors) in a controlled environment using the full-scale data acquisition system prior to the field installation. This is especially necessary of foil type strain gauges, where the modulus of the material used to attach the gauges to the materials will probably be higher than the stiffness of the material. Signal noise from the test configuration must be evaluated prior to the implementation of the network of sensors, rather than doing it as a part of the implementation program. Prior knowledge of on-site noise and any other problems in the signal helps in saving a lot of time during the implementation. The authors recommend the use of wire extensometers and conductance coils to measure the global displacement in the geosynthetics as against the use of strain gauges. The research team at UT Austin also has very good experience with the use of extensometers to measure the strains in the geosynthetics from the small pull-out box test program. They also recommend developing a repeatable gauge evaluation procedure to be performed regularly during testing to evaluate gauge performance over time.

Instrumentation of laboratory sections under APTs

Perkins and Cortez (2005) conducted full-scale APTs on four test sections reinforced with geosynthetics including a control section at the US Army Corp of Engineers Engineering Research and Development Center, Cold Region Research and Engineering Laboratory. They constructed four full scale test sections in the laboratory and used DynaTest Mark IV heavy vehicle simulator to traffic the same. The geosynthetics used were Amoco Propex 2006 woven geotextile, Tensar BX 1100 geogrid and Tensar BX 1200 geogrid.

To measure the vertical dynamic stress within the pavement layers due to the wheel load, DynaTest Stress cells were used. The calibration procedure for the same can be obtained from Selig et al., (1997). These stress cells are placed at a depth of 0.46 m below the pavement surface at the base-subgrade interface below the geosynthetic directly below the center wheel path and at 0.15 m and 0.35 m offsets from the wheel path. The idea behind this placement of the stress cells was that they would shed light into the aspect of the load distribution beneath the wheel load under cases of with and without reinforcement as illustrated in Figure A.9.

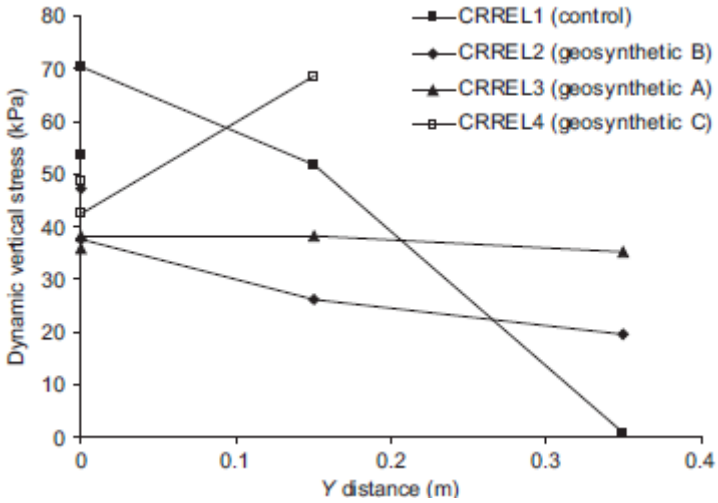

Figure A.9. Distribution of Stresses in the transverse direction (Perkins and Cortez, 2005).

35 EMU Strain coils under various configurations were embedded into the pavement system. These were electromagnetic coils, 100 mm diameter that worked in transmitter-receiver pairs. They measured strains (dynamic and permanent) in the soil in terms of change in voltage across the coils.

Concluding Remarks

A comprehensive list of all instrumentation used in pavement sections in previous studies is listed as follows.

- Profilometer
- LVDT to measure surface deflection
- HMA Strain Gauge
- Soil Strain Gauge
- Settlement plates at different depths
- Extensometers
- Earth Pressure cells
- Pore Pressures sensors
- GeoGrid Strain Gauge (Foil type)
- Light Weight Deflectometer
- Portable Seismic Pavement Analyzer (P-SPA)
- Forensic Trenching

Some of the key lessons learnt from the comprehensive literature survey of those literatures relevant to instrumentation of pavements systems are as follows.

- For the development of accurate performance models and calibration of mechanistic pavement design approaches, it is advised to make use of in-situ measurements of relevant parameters.
- The input parameters for the development of an empirical mechanistic model are the material properties of the various layers in the pavement system such as stiffness, Poisson's ratio, strength, and nature of failure.
- The input parameters for the calibration and validation of an empirical mechanistic model include parameters such as pressure between the layers,

deflection of the layers, strain in the pavement, joint openings, temperature distribution, frost depth characteristics, etc.

- When measuring properties that are to be correlated to each other, such as stress and strain, it is advisable to align the appropriate sensors vertically so that the response measured is not phase delayed.
- The alignment of the gauges inside the pavement section is an important property that determines the survivability of the gauge. As far as possible, gauges must be aligned horizontal, perpendicular to the traffic loads as far as to maximize survivability.
- Use of back-up gauges is highly recommended in the case of field sections, as replacement of faulty gauges is difficult without disturbing the in-situ state of the system.
- One of the critical measurements to develop a mechanistic-empirical model of GSR pavements is the stress at the surface of the subgrade, so EPC measurements are mandatory in this case and backup gauges are highly recommended.
- Ideal locations of the EPCs were found to be at the mid-depth of the base layer and at the base-subgrade interface.
- The calibration of all sensors is recommended to be done using the same data acquisition system as that to be used during the monitoring of the pavement section.
- The use of extensometers with LVDTs is preferred over the use of foil-type strain gauges in measuring the strains in a geosynthetic. This is a more popular observation made by several researchers (Brandon et al., 1996; Warren and Howard, 2007; Zornberg et al., 2008).

- Most of the instrument failures occur either during construction or the first few weeks of operation. Hence caution must be primarily observed during this phase of the project for both field and laboratory scale sections.

A 1.4 ACCELERATED PAVEMENT TESTING OF GRPS

Numerous studies have been carried out in the use of full-scale and reduced-scale APT on Geo-Synthetic Reinforced Pavements. This is primarily due to the unique advantage APT programs have to offer in terms of demonstrating equivalency of two or more test configurations. APT tests have been predominantly used to demonstrate equivalency in terms of increase in traffic benefit ratio, effect on the modulus of the base material, effect on the reduced equivalent thickness of the base material, etc. Since they are cost effective at reduced scales and require a very short amount of time to obtain the results, they make comparisons between several experimental configurations much easier and thus readily favored by the researchers.

Relevant Literature

The Brazilian experience in the field of APTs encompasses 12 years of APT programs. While several parallel studies were run, it is of more relevance to this review to focus on the one involving geosynthetics (Núñez et al., 2008). They evaluated asphalt overlays on top of cracked pavements with and without a reinforcing fabric under the traffic simulator UFRGS-DAER/RS. Two geotextiles (G150 and G150-TF) were used in the study as the inter-layers. Both the reinforced AC overlays performed significantly better than their unreinforced counterpart by delaying the development of cracks and improving pavement life by a factor of two. However, these improvements to fatigue performance did not translate to the field when a similar pavement configuration was

implemented in an in-service road. The performance of the reinforced and control asphalt overlays were found to be similar due to issues in the installation of the geotextiles. Thus, the procedures used for the installation of the geotextiles were found to be crucial to their performance in the field.

Tang et al., (2008) studied the mechanical and physical properties of geogrids that are critical to their effectiveness in the stabilization of pavement subgrade. The MMLS3 was used to traffic the reduced-scale pavement sections stabilized with the various geogrids. Geogrid properties were correlated with bench-scale interface test results such as direct shear, pull-out and the accelerated pavement testing results. The performance was evaluated in terms of surface rutting with trafficking levels. The index properties of the geogrids such as the aperture size, tensile strength, etc. were determined by a series of tests conducted as per the ASTM standards and standards set forth by the Geosynthetic Research Institute (GRI). A summary of the test results is provided in Table A.7.

		Geogrid							
		Grid A		Grid B		Grid C		Grid D	
Index property	Test method	MD*	TD**	MD	TD	MD	TD	MD	TD
Aperture size (mm)	Calipers	27.18	28.96	35.05	41.15	25.65	36.58	25.65	26.42
Rib thickness (mm)	Calipers	0.76	1.12	1.98	1.09	0.76	1.07	1.42	2.03
Junction thickness (mm)	ASTM D5199	1.17		2.29		3.94		1.55	
Mass per unit area (g/m^2)	ASTM D5261	298.37		252.26		319.06		350.93	
Tensile strength at 2% strain (kN/m)		7.5	10.1	14.8	15.0	9.8	15.6	10.3	11.2
Tensile strength at 5% strain (kN/m)	ASTM D6637	13.1	14.1	30.1	30.0	16.8	29.2	18.1	17.4
Ultimate tensile strength (kN/m)		33.3	57.8	36.5	35.7	23.9	32.9	39.5	52.8
Elongation at break (%)		10.5	14.0	7.1	6.7	20.6	10.9	10.5	12.0
Junction strength (kN/m)	GRI GG2	6.1	7.6	10.2	4.3	17.7	28.1	7.4	7.1
Flexural rigidity (mg cm)	ASTM D1388, modified	146,119		271,509		1,429,355		452,671	
Torsional stiffness (cm kg/deg)	COE/GRI GG9	3.47		3.97		7.50		3.43	

*MD, machine direction; **TD, transverse/cross-machine direction.

Table A.7. Tested index properties of the geogrids (Tang et al., 2008).

The bench-scale tests, namely, direct shear test and pull-out box test, were done to characterize the interaction properties of the several types of geogrids installed between

the subgrade and the aggregates used in the aggregate base layer. The results of these tests are shown in Table A.8.

Property	Grid A	Grid B	Grid C	Grid D	Control
Friction angle, δ_{peak} (deg)	28.6	44.0	48.0	32.7	44.2
Efficiency factor, E_ϕ	0.56	0.99	1.14	0.66	N/A
Adhesion, c (kN/m^2)	1.72	0.00	0.00	3.69	0
Interaction coefficient, C_i	0.86	1.00	0.82	0.62	N/A

Table A.8. Results of the direct shear and pull-out tests (Tang et al., 2008)

As for the accelerated pavement testing, the tests were conducted by applying wheel loads from MMLS3 onto the laboratory-fabricated slabs for the four types of geogrid products. Two phases of testing were conducted. APT I with subgrade CBR = 3 and APT II with subgrade = 1.5. The unidirectional trafficking to the pavement was applied by MMLS3 in the controlled laboratory experiment. The APTs were conducted with no lateral wander of the MMLS3, at controlled laboratory temperatures.

From the direct shear test results, the authors found that the interface efficiency factor (the ratio of geogrid-soil interface strength to soil-soil direct shear strength) increased with increasing aperture size to a maximum value and then decreased with further increase in aperture size. They found that the interface efficiency factor did not change with change in the rib thickness of the geogrid. However, the interface efficiency factor showed a strong linear correlation to the sum of the junction strength and the unit tension at 2% strain, indicating that the small-strain tensile stiffness is a good indicator of the performance of a geogrid used for stabilization. Finally, the interface efficiency factor was found to increase with junction thickness (an indicator of the junction strength).

They identified that for pavement applications, the stiffness at small strains under pull-out conditions (confined) was more useful to predict performance compared to the large displacement measures such as the coefficient of interaction or interface strength obtained from pull-out or direct shear tests.

The authors exemplified the fact that the coefficient of interaction being a large strain property had no evident correlation with the index properties of the geogrids. However, one key aspect was observed about the importance of aperture size to aggregate size ratio. It was found that maximum interaction efforts can be achieved when the grain size was similar to that of the geogrid aperture size, as this facilitates an optimum between interlocking and contact area of the geogrid with the granular aggregate.

A summary of the results and the associated trends are tabulated into Table A.9. The trends are indicated as a function of the increasing index properties.

	Correlation and observed trend				
Property	Efficiency factor	Pull-out @ 5 mm	Coefficient of interaction	Rutting @ 1.5 CBR	Rutting @ 3.0 CBR
Aperture area	I	I	I	D	I
Junction strength	I	I	N	D	I
Tensile strength at 2% strain	I	I	N	N	N
Ultimate strength	N	I	N	N	N
Flexural rigidity	N	I	N	D	I
Efficiency factor		I	N	N	I
Pull-out force @ 5 mm				N	N
Coefficient of interaction				N	N

I, increasing trend; D, decreasing trend; N, no observed trend.

Table A.9 Relationship between selected index and bench-scale properties with subgrade rutting from accelerated testing (Tang et al., 2008).

Concluding Remarks

Some of the key lessons learnt from the comprehensive literature survey of those literatures relevant to Accelerated Pavement Testing of GSR pavements sections are as follows.

- Although APT program results show considerable difference in performance of pavement sections with different configurations, one must be wary of the fact a number of factors including but not exclusive to environmental factors, installation conditions, etc. affect the in-field performance of these test sections.
- In the case of geogrid reinforced pavement sections, the aperture size is one of the crucial factors determining the degree of mobilization of the reinforcement.
- For pavement application, evaluation of load-displacement relationship at small displacements correlated well with the pavement performance.
- The choice of aperture size of the geogrid depended on the grain size of the particle such that when the aperture size and grain size are similar, maximum interlocking is expected, which in turn produces better performance.

A 1.5 SUMMARY AND CONCLUSION

Summary

- A brief background of study was provided with emphasis on the expertise needed in the various areas that would contribute to the study. The objectives of this technical memorandum were listed out, followed by brief description of the layout of the technical memorandum.
- The material, geosynthetics, was introduced with brief discussion on the different types and functions of the various geosynthetics. Particular emphasis was placed on geogrids and a historical account of the usage of geogrids in the pavement industry was provided.
- The various geosynthetics used in the previous studies were discussed along with their intended functions and geogrids were identified to be ideal in providing

reinforcement to pavement systems. Relevant literature along with lessons learnt from these literatures were neatly outlined.

- A pavement testing technique, namely Accelerated Pavement Testing was introduced. The advantages and disadvantages of using APT for testing pavement sections were outlined. The cost benefits and scaling limitations with respect to the use of a reduced scale APT program were discussed. One such reduced scale APT device, namely MMLS3 available with UT Austin was described.
- Relevant literature with respect to APT systems, and their use in full-scale field and reduced-scale laboratory pavement sections was reviewed along with the lessons learnt about the advantages, shortcomings, and sources of errors from these systems.
- The need for instrumentation in order to determine the various material properties and input parameters that are identified to be required for developing the empirical mechanistic multi-layer pavement model was outlined.
- The instrumentation used in previous studies for pavement systems in full-scale field sections and in pavement sections subjected to APT in the laboratory was discussed and the relevant lessons learnt were outlined.
- Finally, a few literatures on the use of accelerated pavement testing systems on pavement sections reinforced with geosynthetics were reviewed in order to breed familiarity with the workings of these programs and identify any particular issues with the testing procedures.

Conclusion

Relevant domestic and foreign literature on geosynthetic-reinforced pavement systems, with particular emphasis on the experimental, field validation and design

components of the study were collected, reviewed, assessed, and summarized into Appendix 1. The field performance data from geosynthetic-reinforced pavements constructed in Texas were analyzed and the relevant proposed reinforcement mechanisms were noted. The APT data from relevant unreinforced and geosynthetic-reinforced pavements studies were presented and the relevant strategies to use APT programs to evaluate the performance of GRPs were identified. The relevance of the results from the soil-geosynthetic interaction testing program was determined and the parameters of interest from the testing program were identified.

REFERENCES

Alabaster, D., Arnold, G., Steven, B., 2004a. The equivalent standard axle approach and flexible thin surfaced pavements, in: International Conference on Accelerated Pavement Testing, 2nd, 2004, Minneapolis, Minnesota, USA.

Alabaster, D., Greg Arnold, B.S., Sleath, L., 2004b. Do we really know how thin surfaced granular pavements behave under higher axle loads?, in: International Symposium on Heavy Vehicle Weights and Dimensions, 8th, 2004, Muldersdrift, South Africa.

Brandon, T.L., Al-Qadi, I.L., Lacina, B.A., Bhutta, S.A., 1996. Construction and Instrumentation of Geosynthetically Stabilized Secondary Road Test Sections. TRANSPORTATION RESEARCH RECORD 8.

Brown, S.F., Kwan, J., Thom, N.H., 2007. Identifying the key parameters that influence geogrid reinforcement of railway ballast. Geotextiles and Geomembranes 25, 326–335. https://doi.org/10.1016/j.geotexmem.2007.06.003

Chehab, G.R., Palomino, A., Tang, X., 2007. Laboratory Evaluation & Specification Development for Geogrids for Highway Engineering Applications.

De Beer, M., Fisher, C., Kannemeyer, L., 2004. Towards the application of Stress-In-Motion (SIM) results in pavement design and infrastructure protection.

Epps, A.L., Ahmed, T., Little, D.C., Hugo, F., 2001. Performance prediction with the MMLS3 at Westrack (Research Report No. FHWA/TX-01/2134-1). Texas Transportation Insitute, College Station, TX.

Hugo, F., Martin, A.E., 2004. Significant findings from full-scale accelerated pavement testing: a synthesis of highway practice, NCHRP synthesis. Transportation Research Board, Washington, D.C.

Machemehl, R., Wang, F., Prozzi, J., 2005. Analytical study of effects of truck tire pressure on pavements using measured tire-pavement contact stress data, in: CD-ROM Proceedings for the 84th TRB Annual Meeting. Washington, DC: Transportation Research Board.

Machemehl, R.B., Wang, F., 2006. Development of Quick Solutions for Prediction of Critical Asphalt Pavement Responses due to Measured Tire-Pavement Contact Stresses.

Metcalf, J.B., 1996. Application of full-scale accelerated pavement testing. Transportation Research Board.

Núñez, W., Ceratti, J., Gehling, W. and Oliveira, J., 2008. Twelve years of Accelerated Pavement Testing in Southern Brazil; Challenges, Achievements and Lessons Learned. Plenary Session.'. In Proceedings of 3rd International Conference on Accelerated Pavement Testing-APT'08.

Perkins, S.W., Cortez, E.R., 2005. Evaluation of base-reinforced pavements using a heavy vehicle simulator. Geosynthetics International 13.

Prozzi, J.A., Luo, R., 2005. Quantification of the joint effect of wheel load and tire inflation pressure on pavement response. Transportation Research Record 1919, 134–141.

Sargand, S.M., Green, R., Khoury, I., 1997. Instrumenting Ohio test pavement. Transportation research record 1596, 23–30.

Selig, E.T., Zhang, J., Ebersöhn, W., 1997. Evaluation of dynamic earth pressure cells for subgrade. Transportation research record 1596, 1–6.

Smit, A. de F., Hugo, F., Epps, A., 1999. Report on the first Jacksboro MMLS tests (Research Report No. FHWA/TX-00/0-1814-2). Center for Transportation Research, Austin, TX.

Smit, A. de F., Hugo, F., Rand, D., Powell, B., 2003. Model Mobile Load Simulator Testing at National Center for Asphalt Technology Test Track. Transportation Research Record 9.

Smith, T., Brandon, T., Al-Qadi, I., Lacina, B., Bhutta, S., Hoffman, S., 1995. Laboratory Behavior of Geogrid and Geotextile Reinforced Flexible Pavements. Final Report Submitted to Atlantic Construction Fabrics, Inc. Amoco Fibers and Fabrics Company and the Virginia Center for Innovative Technology, February, Virginia Polytechnic Institute and State University, Department of Civil Engineering, Blacksburg, VA, USA.

Steyn, W.J., 2012. Significant findings from full-scale accelerated pavement testing, NCHRP synthesis. Transportation Research Board, Washington, D.C.

Tang, X., Chehab, G.R., Palomino, A., 2008. Evaluation of geogrids for stabilising weak pavement subgrade. International Journal of Pavement Engineering 17.

Tingle, J.S., Jersey, S.R., 2009. Full-Scale Evaluation of Geosynthetic-Reinforced Aggregate Roads. Transportation Research Record 12.

Tingle, J.S., Webster, S.L., 2003. Corps of Engineers Design of Geosynthetic-Reinforced Unpaved Roads. Transportation Research Record 9.

Wang, F., Machemehl, R.B., 2006. Mechanistic–Empirical study of effects of truck tire pressure on pavement: Measured tire–pavement contact stress data. Transportation Research Record 1947, 136–145.

Warren, K.A., Howard, I.L., 2007. Sensor selection, installation, and survivability in a geosynthetic-reinforced flexible pavement. Geosynthetics International 18.

Watn, A., Eiksund, G., Jenner, C., Rathmayer, H., 2005. Geosynthetic Reinforcement Pavement Systems: European Perspectives, in: International Perspectives on Soil Reinforcement Applications. Presented at the Geo-Frontiers Congress 2005, American Society of Civil Engineers, Austin, Texas, United States, pp. 1–11. https://doi.org/10.1061/40788(167)1

Weinmann, T.L., Lewis, A.E., Tayabji, S., 2004. Pavement sensors used at accelerated pavement test facilities, in: Proceedings of the Second International Conference on Accelerated Pavement Testing.

Zornberg, J.G., Ferreira, J.A.Z., Roodi, G.H., 2013. Geosynthetic-Reinforced Unbound Base Courses: Quantification of the Reinforcement Benefits (Research Report No. FHWA/TX-13/5-4829-01-2), 5-4829-01. TxDOT, Austin, TX.

Zornberg, J.G., Prozzi, J., Gupta, R., Luo, R., McCartney, J.S., Ferreira, J.A.Z., Nogueira, C., 2008. Validating Mechanisms in Geosynthetic Reinforced Pavements (Research Report No. FHWA/TX-08/0-4829-1). University of Texas at Austin, Austin, TX.

Vita

Subu (Subramanian Sankaranarayanan) was born and raised in Tirunelveli, a district in the state of Tamilnadu, closer to the southern tip of India. Growing up in a household that actively encouraged inquisitiveness, Subu grew up enamored with the pursuit of knowledge and wanting to know how everything worked. At the end of his high school, Subu joined the Bachelor's program majoring in Civil Engineering at the National Institute of Technology at Tiruchirappalli, one of the premiere engineering institutions in the country, where he graduated top of his class, with a President's Medal for the highest GPA in the university. Subu went on to pursue his Master's in Geotechnical Engineering at the Indian Institute of Science, Bengaluru, the most prestigious research institution in India. Subu finished his Master's top of his class, with a thesis on the Discrete Element Modeling of Dynamic Soil Testing. Becoming highly interested in research, and academia, Subu joined the University of Texas at Austin to pursue a PhD in Geotechnical Engineering and worked on understanding the performance of flexible pavements with geogrid-stabilized unbound aggregate layers, developing expertise in pavement design, analysis, instrumentation, monitoring, and testing. Post-graduation, Subu is excited to join the industry and grow as a professional pavement engineer.

Email address: ssubu.ind@utexas.edu

This dissertation was typed by Subramanian Sankaranarayanan.